

Feasibility of High Repetition Rate Laser Generated Ultrasound with Composite Comprising  
Candle Soot Nanoparticles and PDMS on Glass

Mahta Nazemi

A Thesis

In the Department

of

Mechanical, Industrial and Aerospace Engineering

Presented in Partial Fulfillment of the Requirements

For the Degree of Master of Applied Science at

Concordia University

Montreal, Quebec, Canada

September 2021

© Mahta Nazemi, 2021

CONCORDIA UNIVERSITY  
SCHOOL OF GRADUATE STUDIES

This is to certify that this thesis is prepared

By: Mahta Nazemi

Entitled: Feasibility of High Repetition Rate Laser Generated Ultrasound with Composite  
Comprising Candle Soot Nanoparticles and PDMS on Glass

and submitted in partial fulfillment of the requirements for the degree of

**Master of Applied Science (Mechanical Engineering)**

complies with the regulations of the University and meets the accepted standards with respect to originality and quality.

Signed by the final examining committee:

\_\_\_\_\_ Chair  
Dr. Muthukumaran Packirisamy

\_\_\_\_\_ Examiner  
Dr. Ashutosh Bagchi

\_\_\_\_\_ Examiner  
Dr. Muthukumaran Packirisamy

\_\_\_\_\_ Thesis Supervisor  
Dr. Sivakumar Narayanswamy

Approved by \_\_\_\_\_  
Chair of Department or Graduate Program Director

\_\_\_\_\_ 2021 \_\_\_\_\_

Dean of Faculty

## Abstract

Feasibility of High Repetition Rate Laser Generated Ultrasound with Composite Comprising  
Candle Soot Nanoparticles and PDMS on Glass

Mahta Nazemi

Ultrasound is widely used in biomedical imaging and non-destructive testing. Recently, Laser Generated Ultrasound (LGU) with high frequencies, large bandwidths have been introduced. LGU transducer typically consists of a light absorber layer and a thermal expansion layer. In this thesis, we concentrate on Candle Soot Nanoparticles (CSNPs) as the light absorption layer and Polydimethylsiloxane (PDMS) as an acoustic transfer medium. There is a lot of work done on LGU composites, however, most of these are experimental. Not much has been done to understand the theory behind LGU composites. On the other hand, almost all the works in the literature utilize high power lasers for the experiments. We aspire to work on high repetition rate LGUs, as they are extensively used in industry and the costs are competitive. Should the feasibility study for high repetition rate LGU needs to be performed, fundamental physics behind LGU need be understood. To this effect, 2D simulation was performed on CSNP/PDMS composite LGU with COMSOL Multiphysics. The material properties of the composite were taken from the literature. The input parameters were selected from literature and the pressure output was extracted from the model. The results from the model for generated acoustic pressure was measured as 5MPa, which compared well with the experiments in literature that measured 4.8MPa under similar conditions. The robustness of the model was further validated using experimental studies for different composites with different thicknesses under different laser fluence. Excellent agreement/trend was found between the results of the model vs results from experiments. Further, high repetition rate laser was examined to study the feasibility of pressure generation. To this effect, composites were fabricated. Damage threshold and absorption coefficient were measured and input into the model for accurate simulation. It was concluded that LGU was feasible under repetition rates of up to 10kHz without damaging the CSNP/PDMS composite. The developed model provides valuable data on how to improve the performance of laser generated ultrasound by tailoring the effective parameters. In this thesis, the study has been successfully carried out to understand the feasibility of using a high repetition rate laser for ultrasound generation using composite (CSNP/PDMS) transducer.

## **Acknowledgments**

The path toward this dissertation has been circuitous. Its completion is thanks in large part to the special people who challenged, supported and stuck with me along the way.

I would first like to express my gratitude to my supervisor, Dr. Sivakumar Narayanswamy for his valuable comments and assistance to guide my work to a satisfactory conclusion.

I am thankful and appreciate my fellow graduate students Hamid Ebrahimi Orimi, Sevin Samadi and Hossein Ghayour for their encouragement and willingness to help me in the technical issues related to my thesis.

I would like to present my sincere thankfulness to my dear mother, Mrs. Zohreh Reyhani and my deceased father, Dr. Shamsedin Nazemi for their continuous effort for my education and intellectual development. I am sorry that my dad did not get to see my completed dissertation. It was my parents' unconditional love, care and tolerance, which made the hardship of writing the thesis worthwhile. Without their support, I do not think that I could overcome the difficulties during these years.

## **Dedication**

To the memory of my father

My best teacher,

who taught me so much in life, and is now my inspiration for continuing on

I miss you endlessly. Forever and always...

To my mother

who has been a source of motivation and

strength during moments of despair and discouragement

## Table of contents

<b>List of Figures</b>	<b>ix</b>
<b>List of Tables</b>	<b>xii</b>
<b>Nomenclature</b>	<b>xiii</b>
<b>List of abbreviations</b>	<b>xv</b>
<b>CHAPTER 1. Introduction</b>	<b>1</b>
1.1 Introduction	1
1.2 The principle of photoacoustic	1
1.3 Laser generated ultrasound (LGU) composite	3
1.4 Photoacoustic generation for thick and thin absorber	4
1.5 Efficiency of photoacoustic generation	5
1.6 Light absorbers	6
1.6.1 CNT/PDMS	7
1.6.2 Carbon black	7
1.6.3 Candle soot nanoparticle	8
1.7 Fabrication of CSNP/PDMS nanocomposite	9
1.7.1 Effect of absorber thickness on photoacoustic generation	11
1.7.2 Elastomer Material	12
1.7.3 Fabrication of PDMS composite transmitter for ultrasound generation	13
1.8 Pulsed laser source	14
1.9 Theory of photoacoustic generation	16
1.9.1 Evaluation of optical absorption coefficient	17
1.9.2 Maxwell-Garnett Theory	18
1.9.3 Beer-Lambert's Law	18
1.9.4 Temperature distribution for metal absorbers	19
1.9.5 Temperature distribution for non-metal absorbers	20

1.10	Focusing ultrasound	20
1.10.1	Focusing in piezoelectric based transducers	21
1.10.2	Focusing technique in laser generated ultrasound	21
1.11	Thesis motivation	23
1.12	Objective and scope of the thesis	23
1.13	Thesis organization	24
<b>CHAPTER 2. Numerical study of LGU</b>		<b>25</b>
2.1	Introduction	25
2.2	2D simulation of laser induced ultrasound	25
2.3	Simulation methodology	26
2.3.1	Geometry	26
2.3.2	Material properties	26
2.3.3	Physics	26
2.3.4	Boundary conditions	30
2.3.5	Parameters of the numerical model and assumptions	32
2.3.6	Mesh and study configuration	32
2.3.7	Output acoustic pressure of 2D model	34
2.4	2D axisymmetric model simulation	36
2.4.1	Geometry	36
2.4.2	Mesh	37
2.4.3	2D-axisymmetric result	37
2.5	Summary	39
<b>CHAPTER 3. Model refinement and validation</b>		<b>40</b>
3.1	Introduction	40
3.2	Model refinement	40

3.2.1	Structural transient behavior	40
3.2.2	Absorption coefficient of CB and CNF	41
3.2.3	Two-layer approach in numerical model of CNF/PDMS	42
3.2.4	Displacement profile of PDMS for different absorbers	42
3.2.5	Generated acoustic pressure in CSNP, CNF and CB embedded PDMS and its comparison with experimental result	43
3.2.6	Comparison of the numerical result with experimental study	46
3.3	Evaluation of output acoustic pressure of CSNP on a curved surface	47
3.4	Mesh refinement	49
3.5	Effect of composite thickness on acoustic pressure	52
3.6	Impact of laser fluence on the acoustic pressure	53
3.7	Relationship between laser pulse width and acoustic pressure	54
3.8	Summary	55
<b>CHAPTER 4.</b>	<b>Feasibility study of LGU using high repetition rate lasers</b>	<b>57</b>
4.1	Introduction	57
4.2	Laser	57
4.3	Fabrication of CSNP/PDMS transducer	58
4.4	Evaluation of the properties of fabricated CSNP/PDMS transducer	60
4.5	Damaged threshold of CSNP/PDMS transducer at various repetition rates	62
4.6	Using MATRIX 532 for photoacoustic generation	64
4.7	Numerical simulation with excitation source as Matrix 532-14-40	66
4.8	Comparison of two numerical model with different aperture sizes	68
4.9	Summary	72
<b>CHAPTER 5.</b>	<b>General conclusion and future outlook</b>	<b>73</b>
5.1	Future research direction	74
<b>References</b>		<b>76</b>

## List of Figures

Figure 1.1 Photoacoustic generation using material ablation and thermal expansion method [6] .	2
Figure 1.2: Laser is used to excite an acoustic wave at the surface of the tissue sample .....	2
Figure 1.3 Schematic of the LGU transducer .....	3
Figure 1.4 Generation of acoustic pressure in thick and thin absorber [6] .....	5
Figure 1.5 Effect of CNT as a light absorber on frequency attenuation [24] .....	7
Figure 1.6 Schematic of the laser-generated-focused ultrasound using CB/PDMS transducer .....	8
Figure 1.7 Schematic of CSNP/elastomer transducer [6] .....	8
Figure 1.8 a) Fabrication of CSNPs on a glass substrate using flame synthesis b) Scanning Electron Microscopy(SEM) of coated CSNPs [29].....	9
Figure 1.9 Relationship between CSNP thickness and its deposition time [29].....	10
Figure 1.10 Light absorption of different thickness of CSNP for different wavelength [29].....	10
Figure 1.11 The relationship between the photoacoustic transduction efficiency and the thickness of CS/PDMS nanocomposites.....	12
Figure 1.12 Impact of curing time on Young's modulus of PDMS [39].....	13
Figure 1.13 Energy per pulse presented as the area under average optical power profile[52] .....	15
Figure 1.14 Characterization of pulsed laser[52].....	15
Figure 1.15 Schematic of CSNP/PDMS photoacoustic transducer [28].....	16
Figure 1.16 Absorption coefficients calculated by Maxwell-Garnett theory as a function of carbon solid volume fraction and wavelength [29] .....	18
Figure 1.17 Focused piezoelectric transducer.....	21
Figure 1.18 Deposition of CSNP on a plano-concave lens [60].....	22
Figure 1.19 Time and frequency response of CSNP/PDMS transducer fabricated on Plano-concave lens [60] .....	22
Figure 2.1 Schematic of laser induced ultrasound using carbon/PDMS transducer and its propagation in water .....	25
Figure 2.2 Acoustic pressure generation process.....	27
Figure 2.3 Spatial (left) and temporal (right) distribution of incident laser intensity.....	28
Figure 2.4 Exponential distribution of laser intensity as it is absorbed by composite.....	29

Figure 2.5 Physics applied to the domains.....	30
Figure 2.6 Boundary conditions in 2D model.....	31
Figure 2.7 Mesh distribution in 2D model.....	33
Figure 2.8 Acoustic pressure propagation in water domain at t=1 to t= 6 microsecond .....	35
Figure 2.9 Average acoustic pressure at 4.2 mm away from the substrate.....	35
Figure 2.10 2D- axisymmetric FE model .....	36
Figure 2.11 Mesh distribution in 2D-axisymmetric model.....	38
Figure 2.12 Average acoustic pressure of 2D-axisymmetric model at 4.2 mm away from the transducer.....	38
Figure 3.1 Time- dependent displacement of CSNP/PDMS composite when selecting "Quasi-static"(left) and "include inertial term" (right).....	41
Figure 3.2 : Schematic of the 2-D model and the point at which displacement is evaluated .....	42
Figure 3.3: Figure 3.3 Displacement profile of the monitoring point in different composite material .....	43
Figure 3.4 2-D axisymmetric model in COMSOL. ....	44
Figure 3.5 Output acoustic pressure generated by CSNP/PDMS composite at 4.2mm .....	45
Figure 3.6 Output pressure of a) CNF/PDMS and b) CB/PDMS transducer at 4.2mm .....	45
Figure 3.7 LGU of CSNP/PDMS transducer measured experimentally by Huang W. et.al[28]..	46
Figure 3.8 Pressure from the model compared with the experiments of Huang et. al.....	46
Figure 3.9: Figure 3.9 HGL-0200, ONDA Crop. ....	48
Figure 3.10: Figure 3.10 a) modified geometry including a semi-sphere monitoring surface b) a new mesh distribution adapted to resolve the acoustic wave in critical section.....	48
Figure 3.11: Figure 3.11 positive and negative pressure wave generated in a) 2-D axisymmetric environment b) 2D environment along the laser beam in the water domain at t=3191 ns .....	48
Figure 3.12: Figure 3.12 Output acoustic pressure of CSNP/PDMS composite evaluated on a semi sphere .....	49
Figure 3.13 Mesh distribution of 2-D axisymmetric model of CSNP with variation of “N” .....	50
Figure 3.14: Figure 3.14 a) Generated acoustic pressure in 2-D axisymmetric model for variation of “N” at t=3191ns. b) Maximum acoustic pressure with respect to “N” .....	51
Figure 3.15 Pressure from the model compared with the experiments of Huang et. al.....	52

Figure 3.16 The amplitude of acoustic pressure with various composite thickness and identical absorption coefficient.....	53
Figure 3.17 Maximum acoustic pressure versus different laser fluence.....	54
Figure 3.18 The peak pressure amplitude for CSNP/PDMS versus laser pulse width.....	55
Figure 4.1 Relationship of Ultrasound bandwidth to laser repetition rate[73] .....	58
Figure 4.2 Fabrication process of CSNP/PDMS nanocomposite .....	59
Figure 4.3 Fabricated planar photoacoustic transmitter coated by CSNP/PDMS layer .....	59
Figure 4.4 Scanning electron microscopy (SEM) of fabricated CSNP/PDMS composite.....	61
Figure 4.5 Scanning electron micrographs of the candle soot/PDMS nanocomposites .....	61
Figure 4.6 Schematic of the experiment done to measure damage threshold of CSNP/PDMS composite. (a) with a plano-convex lens (b) without a lens .....	62
Figure 4.7 Typical beam propagation for MATRIX 532 Models[74].....	63
Figure 4.8 Required beam diameter to produce 11mJ/cm <sup>2</sup> fluence for different repetition rate ..	65
Figure 4.9 Experimental setup .....	66
Figure 4.10 Mesh distribution and pressure propagation of CSNP/PDMS transducer under excitation of Matrix 532-14-40.....	67
Figure 4.11 Output acoustic pressure of CSNP/PDMS transducer under excitation of Matrix 532-14-40 .....	67
Figure 4.12 Output acoustic pressure of CSNP/PDMS transducer fabricated by Wenbin Huang et.al [28] under excitation of Matrix 532-14-40 .....	68
Figure 4.13 Pressure wave propagation in water for beam diameter of 0.53mm (left) and 10mm (right) .....	69
Figure 4.14 Pressure from CSNP/PDMS composite with beam diameter of 0.53 mm and 10 mm .....	69
Figure 4.15 Attenuation of pressure along the propagation axis for 0.53 & 10mm beam diameter .....	70
Figure 4.16 Pressure at various laser fluence measured 4.2 mm away from the composite .....	71
Figure 4.17 Maximum acoustic pressure of reduced-size CSNP/PDMS transducer with respect to various laser energy density.....	71
Figure 4.18 Characteristic curve of Matrix 532-14-40[74].....	72

## List of Tables

Table 1.1 Published papers on laser generated ultrasound using carbon/PDMS transducer .....	11
Table 1.2 Published papers on laser generated ultrasound using carbon/PDMS transducer .....	23
Table 2.1 Dimensions of domains in finite element model in 2D environment .....	26
Table 2.2 Material properties used in computer simulation with Young's Modulus of 750 KPa, and a Poisson's ratio of 0.49 for the composite.....	27
Table 2.3 Simulation parameters for 2D model.....	32
Table 3.1 optical properties of CNF and CB .....	41
Table 3.2 Different values of "N" and its corresponding mesh size.....	49
Table 4.1 optical properties of CSNP/PDMS transmitter measured by power meter .....	60
Table 4.2 Damage threshold of CSNP/PDMS composite in deferent repetition rates .....	64
Table 4.3 Beam diameter required to produce laser fluence of 11 mJ/cm <sup>2</sup> .....	64
Table 4.4 Simulation parameters for excitation source as Matrix 532-14-40.....	66
Table 4.5 Simulation parameter of CSNP/PDMS transducer fabricated by Wenbin Huang et.al [28] under excitation of Matrix 532-14-40.....	68
Table 4.6 Input parameters of CSNP/PDMS transducer in the numerical model .....	69
Table 4.7 Material properties and laser parameter in 2D axisymmetric model.....	70

## Nomenclature

$\alpha$	Thermal diffusivity	$\text{m}^2.\text{s}^{-1}$
$E_0$	Laser fluence	$\text{mJ}.\text{cm}^{-2}$
$\tau$	Pulse duration	ns
$\beta$	Absorption coefficient	$\mu\text{m}^{-1}$
$\beta_T$	Thermal expansion coefficient	$\text{K}^{-1}$
$\kappa$	Thermal conductivity	$\text{W}.\text{K}^{-1}.\text{m}^{-1}$
$S$	Arbitrary thermal source	$\text{W}.\text{m}^{-3}$
$q$	Heat flux	$\text{W}.\text{m}^{-2}$
$P_0$	Initial acoustic pressure	MPa
$P$	Acoustic pressure	MPa
$\eta$	Photoacoustic efficiency	-
$E_a$	Acoustic energy	J
$E_{optical}$	Laser pulse energy	J
$I_0$	Incident light intensity of laser	$\text{W}.\text{m}^{-2}$
$l$	light intensity of laser	$\text{W}.\text{m}^{-2}$
$\lambda$	Wavelength of light	m
$d_t$	Thermal diffusion path	$\mu\text{m}$
$d$	Light penetration depth	$\mu\text{m}$
$d_p$	Diameter of a nanoparticle	$\mu\text{m}$
$a$	Shape constant of nanoparticle	-
$l$	Thickness of composite	$\mu\text{m}$
$D$	Laser beam diameter	mm
$h$	Mesh size	$\mu\text{m}$
$u$	Acceleration	$\text{m}.\text{s}^{-2}$
$c$	Speed of sound	$\text{m}.\text{s}^{-1}$
$C_p$	Specific heat capacity of composite	$\text{J}.\text{kg}^{-1}.\text{K}^{-1}$
$T_{amb}$	Ambient temperature	K
$\rho$	Density	$\text{Kg}.\text{m}^{-3}$
$S_T$	Total stress	$\text{N}.\text{m}^{-2}$
$F$	Volume force	N

$\sigma_s$	Stefan-Boltzmann constant	-
$\varepsilon$	Surface emissivity	-
$\Gamma$	Grüneisen parameter	-
A	Absorption	-
T	Transmittance	-
R	Reflectance	-
$f$	Frequency	Hz
$\omega$	Angular frequency	rad.s <sup>-1</sup>
$\varepsilon_{eff}$	Effective dielectric constant of carbon/PDMS	-
$\varepsilon_{PDMS}$	Dielectric constant of PDMS	-
$\varepsilon_c$	Dielectric constant of Carbon	-
V	Carbon volume fraction	-
N	Constant of mesh size in 2D simulation	-
$t_{th}$	Thermal relaxation time	s
$t_{ac}$	Acoustic propagation time	s
$t_0$	Laser peak time	s
$t_p$	Pressure peak time	s
$\sigma$	Standard deviation of spatial profile of laser intensity	s

## List of abbreviations

LGU	Laser Generated Ultrasound
PA	Photoacoustic
PDMS	Polydimethylsiloxane
CSNP	Candle Soot Nanoparticle
CB	Carbon Black
CNT	Carbon Nanotube
CNF	Carbon Nanofiber
PML	Perfectly Matched Layer
NP	Nano Particle
LUT	Laser Ultrasound Transmitter
RT	Room Temperature
AuNP	Gold Nanoparticle
RGO	Reduced Graphene Oxide
HIFU	High Intensity Focused Ultrasound
FEA	Finite Element Analysis
CS	Candle Soot
RBAM	Radiative Beam in Absorbing Media
PDE	Partial Differential Equation
OD	Optical Density
HRRL	High Repetition Rate Laser

## **CHAPTER 1. Introduction**

### **1.1 Introduction**

The past fifty years have seen important advances in the understanding, development and application of ultrasound methods for medical and industrial uses. Ultrasound is widely used in health monitoring, biomedical imaging, drug delivery and non-destructive testing [1]–[4]. Ultrasound transmitters are the main element of ultrasound technology. As a result of more advanced applications, transmitters are required to have good conversion efficiency, high frequency, broad bandwidth and compact size.

Traditionally, ultrasound is generated by piezoelectric based transducer. The output performance of the transduction structure dramatically relies on the properties of chosen active materials such as quartz, lead Zirconate titanate (PZT) and, lead magnesium niobate-lead titanate (PMN-PT) However, technological limitations such as power per radiating surface area and the electrical voltage applied to the transducer need to be overcome[5]. As an alternative method, all-optical ultrasound with high frequencies, large bandwidths and a strong miniaturization potential has been introduced. In this method, ultrasound is generated via the photo-acoustic effect: excitation light is delivered to an optically absorbing coating where it is absorbed, leading to increase in temperature. The resulting pressure increase propagates as an ultrasound wave.

There are two possible methods to yield laser ultrasound which will be explained in detail in the next part.

### **1.2 The principle of photoacoustic**

The photoacoustic (PA) effect is the generation of high-frequency sound waves upon the absorption of a light pulse and it can happen in two ways: light assisted material ablation (plasma approach) or thermal expansion (thermoelastic approach). Figure 1.1 shows the difference between these two approaches. In case of high intensity light pulses, the temperature of the absorbing layer might go beyond its melting point. As a result, material will experience a phase change which leads to acoustic wave generation. However, ablation process will cause damage to material. In contrast, thermoelastic induced acoustic pressure can be generated by relatively low laser power

density. Therefore, it is favorable for biomedical imaging applications. Here, we shall limit our discussion to thermoelastic assisted laser generated ultrasound (LGU).

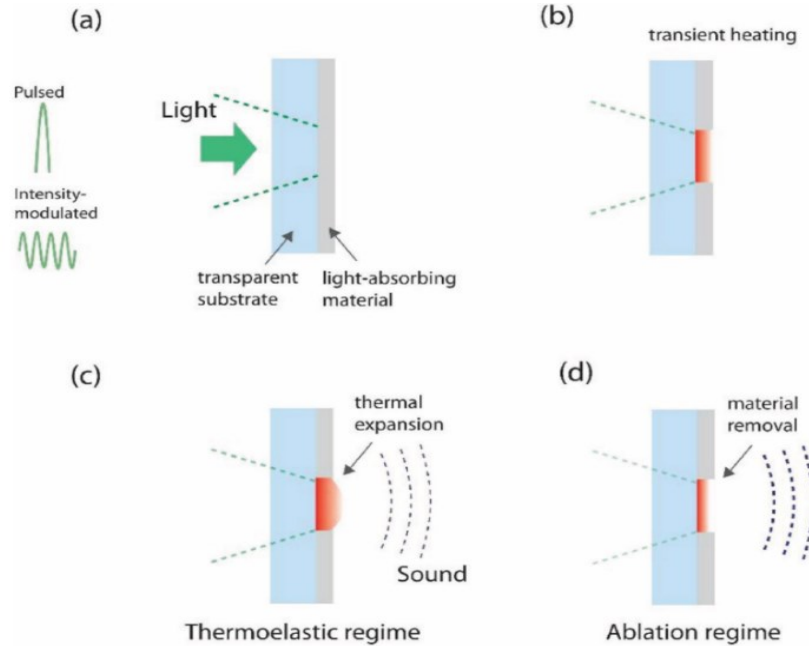


Figure 1.1 Photoacoustic generation using material ablation and thermal expansion method [6]

Initially laser was used to generate ultrasound using absorption of body organs as in figure 1.2. However, desirable amplitude and frequency control of ultrasound was a challenge in this approach. To overcome this, LGU using composite materials became the research focus in this area.

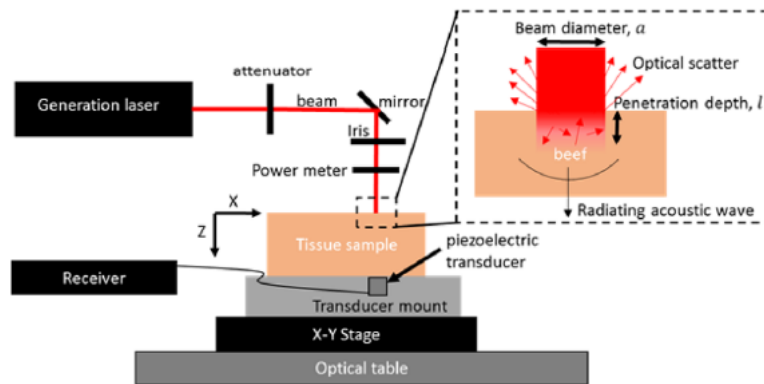
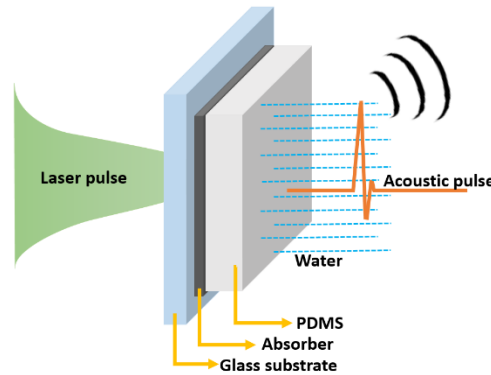


Figure 1.2: Laser is used to excite an acoustic wave at the surface of the tissue sample

### 1.3 Laser generated ultrasound (LGU) composite

LGU transducer typically consists of two layers: a light absorber layer for effective conversion of light to heat and a layer with high coefficient of thermal expansion. Polydimethylsiloxane (PDMS) is being used as an acoustic transfer medium thanks to its high coefficient of thermal expansion. Since PDMS is not considered as an absorber, it is usually mixed with an absorptive material to enhance the transmission efficiency of LGU. As an example, metallic absorbers such as Al thin film, gold nanoparticles (AuNPs), reduced graphene oxide (RGO), nanostructured germanium and carbon-based material such as carbon black (CB), carbon nanotube (CNT) nanocomposites, carbon nanofibers (CNF) and more recently candle soot carbon NPs have gained attention as absorber material [6]–[12]. Figure 1.2 shows the generation of acoustic pulse and how the above-mentioned layers are coated on a glass substrate.



*Figure 1.3 Schematic of the LGU transducer*

In order to generate acoustic wave efficiently, two conditions referred to thermal and stress confinement must be met [13]. If the heat generated by absorption of light stays confined in the irradiated volume during the laser pulse and cannot escape through heat conduction, a condition termed “thermal confinement” is obtained. In other words; laser duration has to be shorter than the thermal relaxation time given by:

$$t_{th} = \frac{d_t^2}{4\alpha} \quad (1-1)$$

Where  $d_t$  is the thermal diffusion path known as characteristic length and  $\alpha$  is heat diffusivity [14]. This condition requires the heating time to be much shorter than the time for heat to conduct away from the heating zone in the material and allows for the assumption of instantaneous heating. The

instantaneous heating gives rise to the local expansion of the material and the need for the localized stress or acoustic (source) condition[15].

Acoustic waves also require what is called stress confinement. It is achieved when heating pulse is much shorter than the acoustic propagation time across the optical absorption depth given by:

$$t_{ac} = \frac{d}{c} \quad (1-2)$$

$d$  is the penetration depth which is equal to inverse of absorption coefficient and  $c$  is the speed of sound[16].

#### 1.4 Photoacoustic generation for thick and thin absorber

The light absorption amplitude of thin absorber is larger than for thick one. As illustrated in figure 1.4, for the thin absorber, the heat source emits fewer numbers of sound waves of higher amplitudes, whereas the heat source for the thick absorber generates more numbers of sound waves of lower amplitudes. As a result, thin absorber will have high amplitude photoacoustic waves with narrow pulse width. Whereas for thick absorber photo acoustic waves will have low amplitude and wide pulse width.

The photoacoustic pressure amplitude is given by:

$$P_0 = \Gamma \cdot A \cdot \frac{E_0}{c\tau + \frac{1}{\beta}} \quad (1-3)$$

The condition  $c\tau_l \gg 1/\beta$ , commonly observed in thin absorbers, is referred to as long pulse regime. In contrast, the condition  $c\tau_l \ll 1/\beta$  for thick absorbers is referred to as short pulse regime. In these cases, the photoacoustic pressure amplitude can be expressed by:

$$P_0 = \Gamma \cdot A \cdot \frac{E_0}{\max(c\tau, \frac{1}{\beta})} = \begin{cases} \Gamma \cdot A \cdot \frac{E_0}{c\tau} & (\text{long pulse regime; } c\tau \gg \frac{1}{\beta}) \\ \Gamma \cdot A \cdot \frac{E_0}{1/\beta} = \Gamma \cdot A \cdot \alpha E_0 & (\text{short pulse regime; } c\tau \ll \frac{1}{\beta}) \end{cases} \quad (1-4)$$

In this equation,  $\Gamma$  is a dimensionless thermodynamic coefficient known as the Grüneisen parameter and it equals  $\Gamma = \frac{\beta_T c^2}{C_p}$ . Where  $\beta_T, c, C_p, A, E_0, \beta$  and  $\tau_l$  represent thermal expansion

coefficient, sound speed, specific heat capacity, light absorption ( $0 < A < 1$ ; dimensionless), laser fluence, absorption coefficient and pulse duration respectively [6].

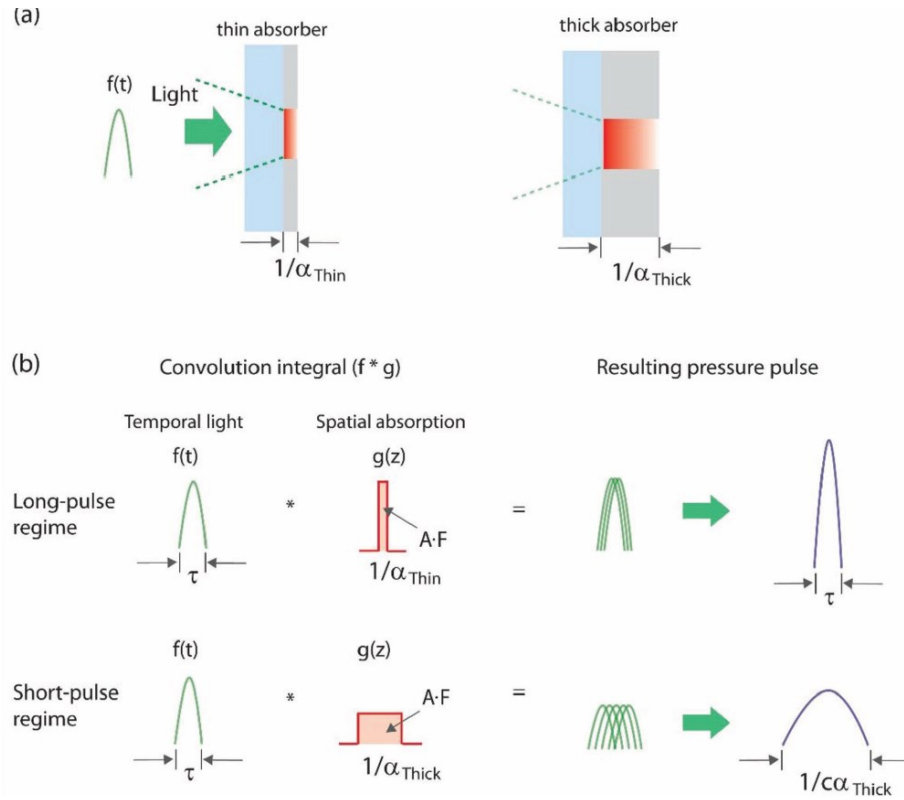


Figure 1.4 Generation of acoustic pressure in thick and thin absorber [6]

It is demonstrated experimentally and theoretically that the transducer's operational frequency is reverse proportion to the thickness of CNTs array-PDMS composite [7].

$$f = \frac{c}{4l} \quad (1-5)$$

where  $l$  is the thickness of CNTs array-PDMS composite and  $c$  is the speed of sound in composite.

## 1.5 Efficiency of photoacoustic generation

The efficiency of photoacoustic generation is calculated by following relationship:

$$\eta = \frac{E_a}{E_{optical}} \quad (1-6)$$

Where  $E_{optical}$  denotes laser pulse energy and  $E_a$  is acoustic energy. Acoustic energy can be expressed by following equation:

$$E_a = \frac{1}{\rho c} A \int_0^{\infty} P^2(t) dt \quad (1-7)$$

In this equation,  $\rho$  and  $c$  are the density and speed of sound in water respectively and  $A$  is the acoustic spot area which is approximately equal to laser beam size near transducer surface.  $P$  is the acoustic pressure[9].

## 1.6 Light absorbers

Optical absorbers refer to functional materials or structures that can effectively absorb electromagnetic waves and then convert the electromagnetic energy into thermal energy. For this reason, optical absorbers have been extensively studied with increasing demand for innovative applications in optical sensors as well as photoacoustic transducers[17]–[21]. As it can be seen in equation (1-4), in order to have high pressure amplitude it is crucial to have excellent light absorption followed by fast heat transfer to the surrounding thermal expansion medium. Several optical absorbers made of Germanium [22] , Gold NPs [23] and carbon have been integrated. Among metal-based absorbers, nanostructured Germanium (Ge) possess high amplitude acoustic wave which is 7.5 times stronger than that of the Cr transmitter[22].

In order to generate high frequency ultrasound, rapid heating is an important prerequisite. Carbon nanomaterials such as CB, CNFs, CNTs and CSNPs exhibit high thermal conductivity and consequently high thermal diffusivity which leads to fast heat transfer. If the duration of exposure to laser radiation is long, significant quantities of heat will diffuse out of the target volume during irradiation, reducing the efficiency of heating. As a result, it is desirable to deliver heat in a time shorter than a characteristic time known as the thermal relaxation time. In this way, heat may be confined to the target during delivery, maximizing the peak temperature.

Thermal diffusion time is predicted by the following relationship:

$$\tau_{th} = \frac{d_p^2}{\alpha k} \quad (1-8)$$

Where  $d_p$ ,  $a$  and  $\alpha$  are diameter of a particle, thermal diffusivity and ‘k’ constant varying with particle shape[14]. Accordingly, thermal relaxation time is dependent on the particle size, material type, and particle shape.

### 1.6.1 CNT/PDMS

It has been demonstrated that a small weight fraction of added CNT in PDMS, results in a significant increase in acoustic attenuation in high frequencies as shown in figure 1.5. However, the presence of CNT does not have a measurable effect on the speed of sound[24].

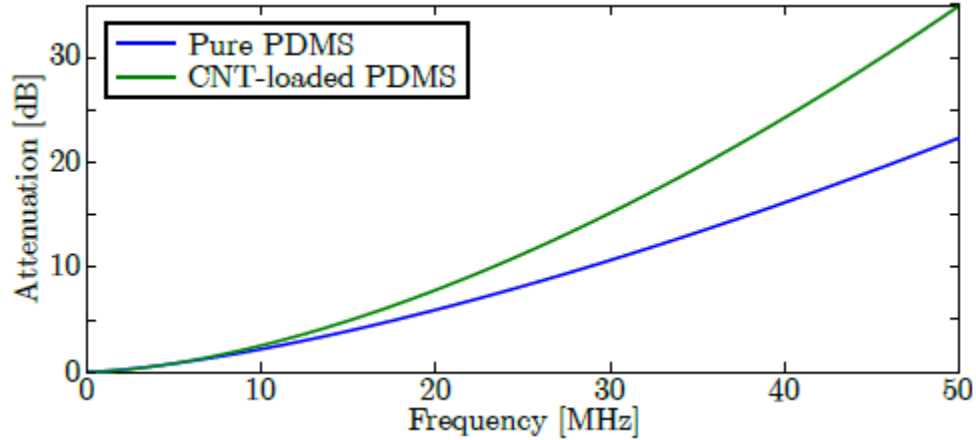


Figure 1.5 Effect of CNT as a light absorber on frequency attenuation [24]

### 1.6.2 Carbon black

Carbon black is available in form of dye and it is usually added to the uncured PDMS to be coated on a substrate. Carbon black as an absorber for photoacoustic generation has been coated in both planar and curved substrate in accordance to the application. Jinwook Kim et.al demonstrated the efficacy of sonothrombolysis using a laser generated focused ultrasound transducer with CB/PDMS coating[25]. In another study, the pulsed waves of ultrasound, generated by a CB/PDMS photoacoustic lens were introduced to trigger the drug release from a microgels encapsulated with drug-loaded as it is depicted in figure 1.6[26].

Experimental study of CB/PDMS reveals that there is an increase in absorbance by increasing the filler content. The nanocomposite conductivity is 35.2 % higher than the base material. As well, the thermal expansion coefficient decreases with an increase in carbon black content[27].

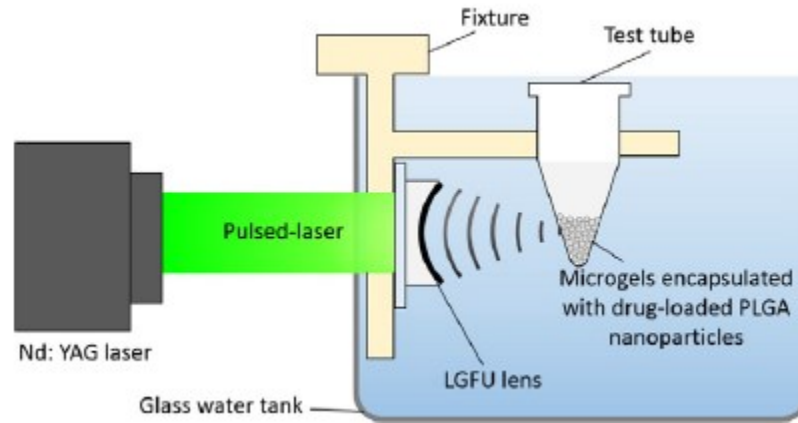


Figure 1.6 Schematic of the laser-generated-focused ultrasound using CB/PDMS transducer

### 1.6.3 Candle soot nanoparticle

CSNP (candle soot nanoparticle) composites exhibit a high energy conversion and fabrication simplicity compare to other carbon-based composites[28]. They are widely used in laser ultrasound transmitters (LUTs). As mentioned earlier, thermal relaxation time is affected by geometric shape of nanoparticles. The value of  $k$  for spherical shapes is 24 whereas it is 16 for cylindrical shapes nanoparticles[8], [14]. Hence, CSNPs would be more advantageous for efficient heat transfer compare with carbon nanofibers and carbon nanotubes. Figure 1.7 depicts schematic of CSNPs/elastomer composite coated on a glass substrate and generated pressure pulse.

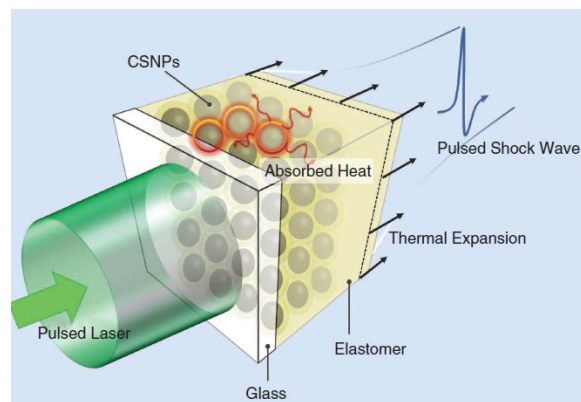
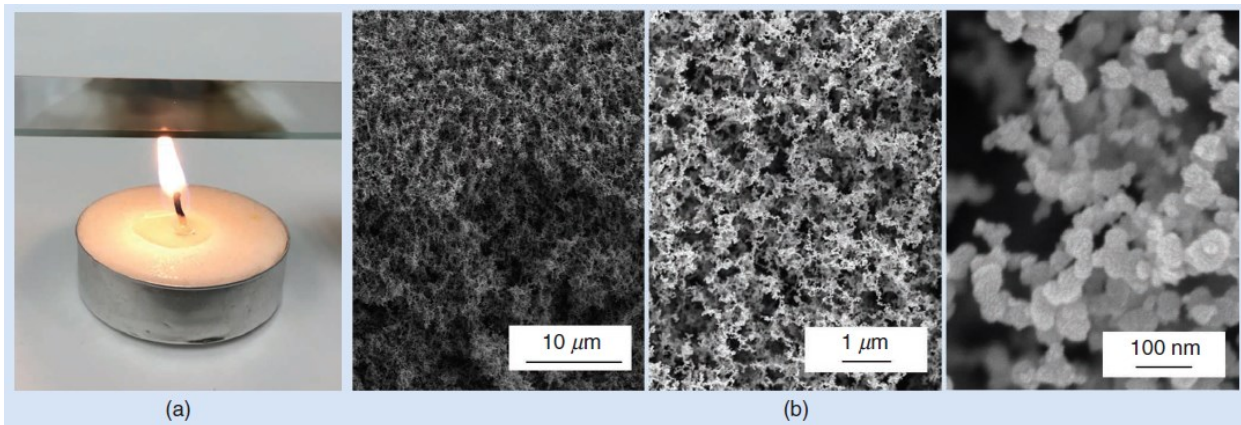


Figure 1.7 Schematic of CSNP/elastomer transducer [6]

One study showed that acoustic pressure from CSNP/PDMS can reach 4.8 MPa which is twice of CNFs-PDMS transducer[9]. Several efficient LGU designs have been developed using CSNP/PDMS composites.

### 1.7 Fabrication of CSNP/PDMS nanocomposite

A candle flame with incomplete combustion generates a cloud of black soot that consists of nano-size particles made of carbon (91.69%), hydrogen (1.75%), nitrogen (0.12%), and oxygen (calculated, 4.36%). Fast heat diffusion is possible due to nano-size carbon particles. Figure 1.8, shows the generation of carbon nanoparticles and their nano-size dimension. Carbon nanoparticles adhere to the glass substrate and then develop porous structure.



*Figure 1.8 a) Fabrication of CSNPs on a glass substrate using flame synthesis b) Scanning Electron Microscopy(SEM) of coated CSNPs [29]*

It has been shown that by changing the deposition time, different thicknesses of CS can be deposited[29]. Figure 1.9 shows the linear relationship between deposition time and CSNP thickness. A study showed that for carbon deposition time longer than 120 sec, the composite becomes very absorptive and the absorption saturates at around 96%[29]. Experimental result of 20, 60 and 120 s deposition time, is depicted in figure 1.10.

The PDMS is prepared with a base and curing agent (Sylgard 184). The recommended ratio of 10 parts base to 1 part curing agent is used to fabricate PDMS. To fabricate bubble free sample, the uncured mixture of PDMS is degassed in a vacuum desiccator for 30 minutes. The degassed PDMS mixture is then spin-coated directly on the CSNP-coated glass substrate[9], [28], [29][30]. In some cases where the composite is made on the tip of fiber optics, dip coating method is used [31]–[33].

Sylgard 184 can be cured at both room temperature ( $RT = 25\text{ }^{\circ}\text{C}$ ) and elevated temperatures ( $RT > T > 200\text{ }^{\circ}\text{C}$ )[34]. Table 1.1, shows the summary of recent published paper on this type of composites.

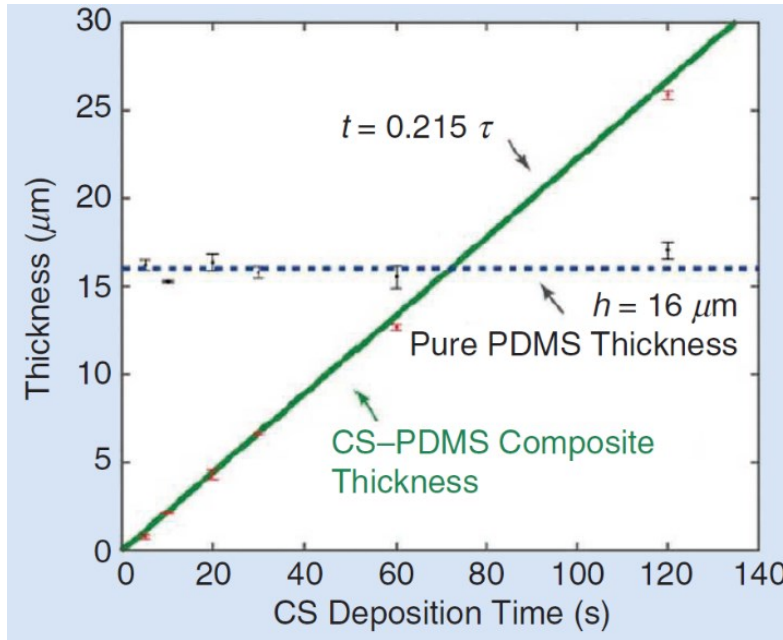


Figure 1.9 Relationship between CSNP thickness and its deposition time [29]

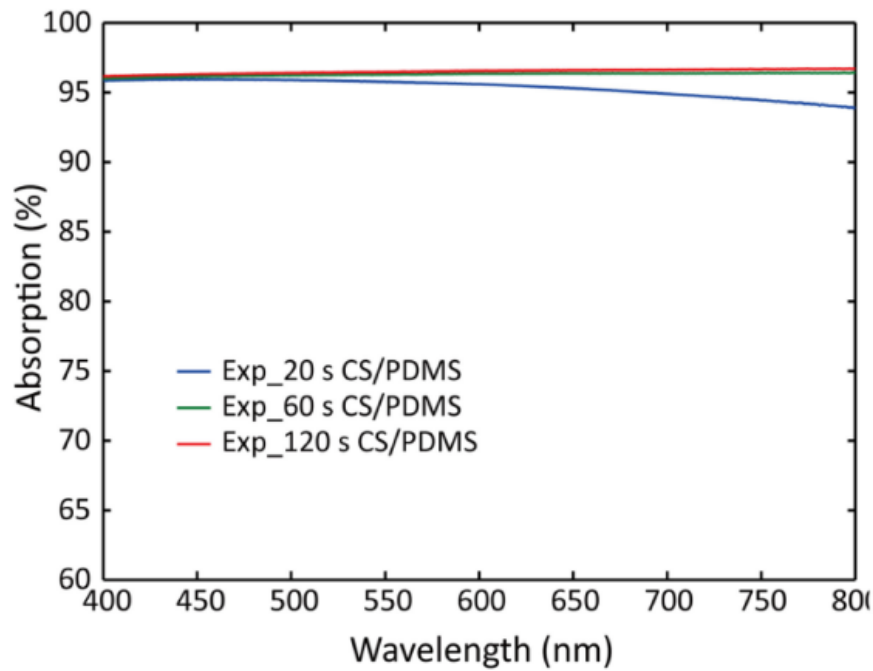


Figure 1.10 Light absorption of different thickness of CSNP for different wavelength [29]

Composite material	Total thickness [ $\mu m$ ]	Absorber thickness [ $\mu m$ ]	Pulse duration [ns]	Laser fluence [ $mJ/cm^2$ ]	Acoustic pressure [MPa]	Photoacoustic conversion efficiency [ $Pa/(\frac{W}{m^2})$ ]
CSNP/PDMS[28]	24.4	6.5	6	3.57	4.8	$4.41 \cdot 10^{-3}$
CSNP/PDMS[29]	18	2	6	1	3.78	$9.02 \cdot 10^{-3}$
CB/PDMS[9]	30	-	6	3.57	0.8	$0.3 \cdot 10^{-3}$
CNF/PDMS[9]	57.8	25	6	3.57	2	$1.6 \cdot 10^{-3}$
CNF/PDMS[12]	57.8	25	4	3.71	12.15	$15.6 \cdot 10^{-3}$
CB/PDMS[12]	30	30	4	3.71	2.13	N/A
RGO/PDMS[35]	0.2	0.1	5	56	9.5	N/A
CNT/PDMS[7]	58	18	6	51	8.8	$2.51 \cdot 10^{-3}$
CNT/PDMS[36]	-	23	4	-	5	-

*Table 1.1 Published papers on laser generated ultrasound using carbon/PDMS transducer*

### 1.7.1 Effect of absorber thickness on photoacoustic generation

Wei-Yi Chang et al improved the conversion efficiency of the transducer by optimizing the absorber thickness. That is, when the thickness of the absorption layer (CS/PDMS layer) is greater than the optical absorption thickness, the output acoustic pressure increases as the thickness of the absorption layer decreases. As a result they increased the conversion efficiency to  $9.02 \times 10^{-3}$  which is twice that of previous result[29]. Photoacoustic efficiency for CS/PDMS nanoparticles with different CS deposition can be found in figure 1.11.

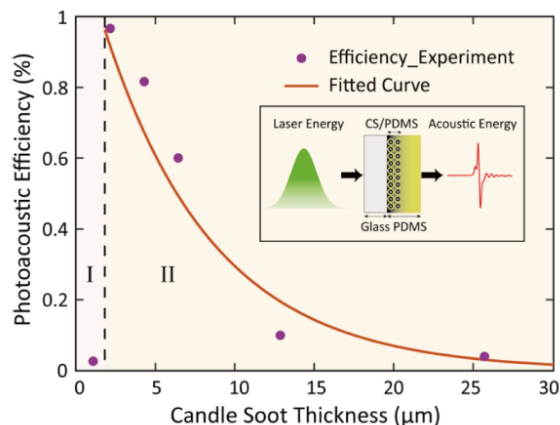


Figure 1.11 The relationship between the photoacoustic transduction efficiency and the thickness of CS/PDMS nanocomposites

By keeping the coefficient of absorption constant, the output pressure will depend on composite thickness. As it is depicted in figure 1.9, pressure amplitude increases first and then starts to saturate by enlarging the thickness. That is because optical energy cannot be fully absorbed by the composite if its thickness is less than light penetration depth. However, in reality output pressure will drop as the thickness of composite become larger. Wei-Yi Chang et al showed that candle soot deposition time of more than 60 second which leads to 13μm of candle soot will result in degradation of acoustic pressure[29]. From the experimental study done by Ye Tian the efficient thickness is three to six times of the penetration depth[37].

### 1.7.2 Elastomer Material

Strong thermoelastic property is necessary to provide efficient thermal to mechanical energy. Therefore, in addition to light absorber layer, a layer with high coefficient of thermal expansion needs to be added to the transducer. Among metallic materials and epoxy resins which have been utilized, PDMS has shown promising results due to its high coefficient of expansion ( $\beta_T = 0.92 \times 10^{-3} K^{-1}$ ) and its optical transparency below the infrared band [35], [38]. Aluminum is another material that has been used as an acoustic transmitter medium. Lee et al, demonstrated that reduced graphene oxide (RGO) coated thin aluminum film is an effective optoacoustic transmitter for generating high pressure ultrasound [35]. However, its relatively small coefficient of thermal expansion ( $23.1 \times 10^{-6} K^{-1}$ ), makes it less favorable compare to PDMS.

### 1.7.2.1 Mechanical properties of PDMS

It has been observed that the mechanical properties of PDMS vary with both curing and operational temperatures. Miao Liu et al studied the influence of curing temperature and time on Young's modulus of PDMS membrane[39]. The result is shown in figure 1.12. The curing temperature for Sylgard 184 is kept below 200°C since greater heating temperature causes thermal decomposition of PDMS [39]. The refractive index of PDMS is 1.4 [40].

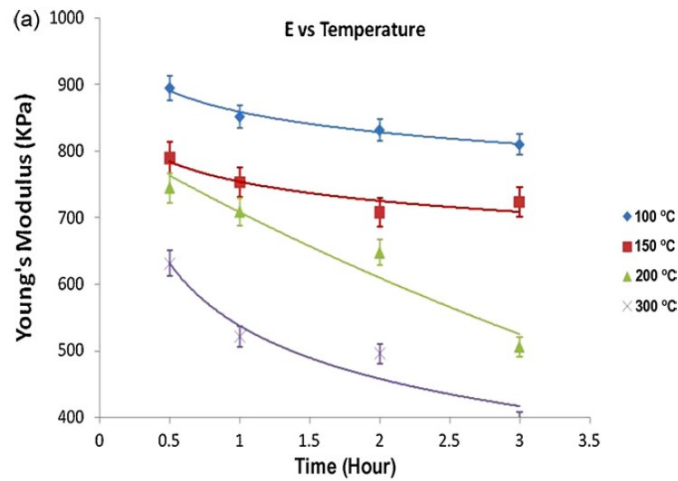


Figure 1.12 Impact of curing time on Young's modulus of PDMS [39]

### 1.7.3 Fabrication of PDMS composite transmitter for ultrasound generation

Previously, we highlighted the use of PDMS as a host material for optical absorbers. There are different fabrication processes to create PDMS composites with high optical absorption. However, this integration process is not always straightforward, as the hydrophobicity of the precured PDMS limits the type of absorbers that can be integrated and it can be challenging to achieve homogeneous composites. Moreover, maintaining small coating thicknesses to reduce acoustic attenuation and maintain wide bandwidths for high-resolution imaging can be difficult[41]. It is demonstrated experimentally and theoretically that the transducer's operational frequency is reverse proportion to the thickness of composite. Li et al. have depicted the relationship between the operational frequency of optoacoustic transducer and the CNTs array-PDMS composite's thickness as:

$$f = \frac{c}{4l} \quad (1.9)$$

Where  $c$  is the speed of sound in the composite and  $l$  is the composite thickness[7]. These fabrication processes involve different PDMS deposition techniques such as spin-coating, electrospinning, and dip-coating, to minimize coating thicknesses and maximize ultrasound bandwidths. Fabrication methods of PDMS composites can be categorized as follows:

- **All in one** method, in which the PDMS and optically absorbing component are mixed prior to coating the substrate to achieve homogeneous composites. It can be used to fabricate both metallic nanoparticle carbon based PDMS composite coatings. Examples are the gold nanoparticle-PDMS composite developed by Zou et al.[42] and carbon black-PDMS composite designed by Buma et al. [43].
- **Bottom-up** methods, in which the optically absorbing material is coated on the substrate and subsequently over coated with optically transparent PDMS to achieve a bilayer composite. Both spin-coating and dip-coating techniques for PDMS have been suggested in the literature [44][9][4][45][46]. Multiwalled CNTs are usually grown by a chemical vapor deposition process [47][7].
- **Top-down** methods, in which optically transparent PDMS is applied to the substrate and the optical absorber is subsequently incorporated to achieve a micrometer scale composite region. The incorporation of the optical absorber can be achieved by the diffusion of nanomaterial from the solution or by ion implantation[48][49].

## 1.8 Pulsed laser source

A laser emits a beam of coherent radiation, whose wavelength may be in the infrared, visible or ultraviolet part of the electromagnetic spectrum. When this is incident on a solid sample, in general some of the energy is absorbed by various mechanisms, depending upon the nature of the sample and the frequency of the radiation, while the remainder is reflected or scattered from the surface. Increasing the optical wavelength, further into the infrared increases the reflectivity[50]. For the case of laser ultrasound generation, it is imperative to have less reflection and more absorption. Thus, shorter wavelengths generate more efficient ultrasonic wave. In addition, pulse width need to be short enough to meet thermal and stress confinement[30]. Theoretical analysis shows that the employment of ultrashort pulses leads to substantial enhancement in photoacoustic conversion

efficiency and spatial resolution[51]. Thus, pulsed lasers with nanosecond pulse width are mostly used.

Pulsed lasers emit bursts of light spaced in time as shown in figure 1.13. Between pulses, the laser emits no light. The period is the time from the start of one pulse to the next. The pulse duration (pulse width) is the time measured across a pulse, often at its full width half maximum (FWHM). Pulse energy is a measure of emission over one period. Each period contains a single pulse, and all energy emitted during one full period is delivered by the pulse. Pulse energy, shown as the shaded regions in Figure 1.13 below. Longer pulse width produces larger pulse energy and the average power, as shown in figure 1.14, is controlled by pulse width and period.

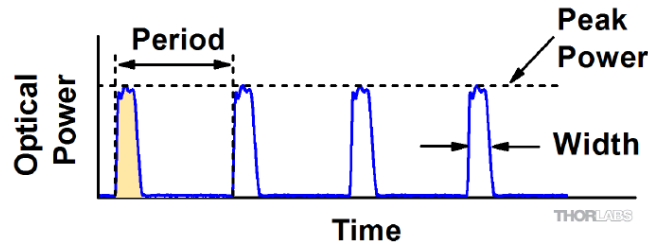


Figure 1.13 Energy per pulse presented as the area under average optical power profile[52]

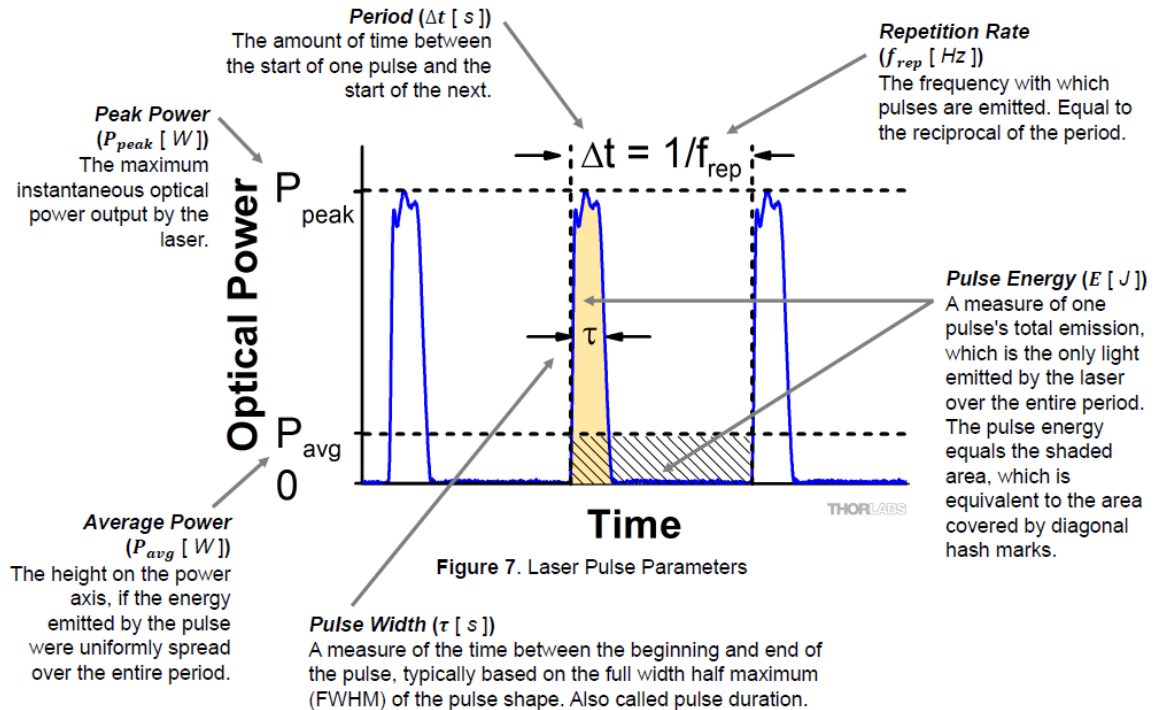


Figure 1.14 Characterization of pulsed laser[52]

## 1.9 Theory of photoacoustic generation

Although Equation (1-4) provides reasonable order-of-magnitude estimation, the photoacoustic amplitude can be more precisely calculated by simultaneously solving heat conduction equation and pressure wave equation. Temperature field caused by pulsed laser heating can be obtained by solving the conduction equation, which is represented below:

$$\kappa_i \nabla^2 T_i - \frac{\kappa_i}{\alpha_i} \frac{\partial T_i}{\partial t} = -S_i \quad (1-10)$$

Where  $\kappa$ ,  $\alpha$ ,  $t$ ,  $T$  and  $S$  are thermal conductivity, thermal diffusivity, time, temperature, and an arbitrary thermal source respectively. Subscript “i” denotes the layer numbers as shown in the figure 1.15.

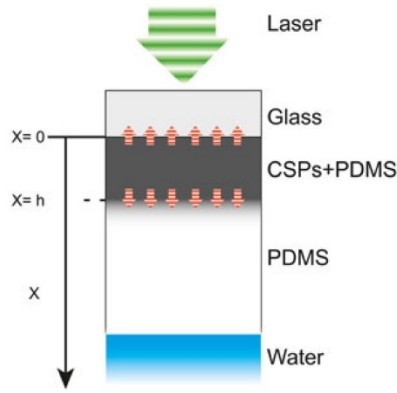


Figure 1.15 Schematic of CSNP/PDMS photoacoustic transducer [28]

The pure PDMS layer, CSNPs-PDMS composite layer, and backing glass layer are numbered as 1, 2, 3, consecutively. The thickness of the composite layer is  $h$ .

Since short laser pulse within tens of ns is used, the thermal diffusion during the acoustic generation can be neglected and equation (1.14) is simplified to:

$$\frac{\partial^2 T_i}{\partial t^2} = \frac{1}{\rho_i C_p} \frac{\partial S_i}{\partial t} \quad (1-11)$$

where  $\rho$  is the density and  $C_p$  is the thermal capacity which equals  $C_p = \kappa_i / \rho_i \alpha_i$ .

In the media, the thermal-mechanical coupled equations can be given below,

$$\nabla^2 P_i - \frac{1}{c_i^2} \frac{\partial^2 P_i}{\partial t^2} = -\rho_i \beta_{T_i} \frac{\partial^2 T_i}{\partial t^2} \quad (1-12)$$

where P is the pressure,  $\beta_T$  is the thermal volume expansion constant, and c is the sound speed in the medium.

Substituting the equation (1-15) into equation (1-16), yields:

$$\nabla^2 P_i - \frac{1}{c_i^2} \frac{\partial^2 P_i}{\partial t^2} = -\frac{\beta_{T_i}}{C_{P_i}} \frac{\partial S_i}{\partial t} \quad (1-13)$$

The absorbed light by CNPs-PDMS is converted into thermal. The heating function in the 2nd medium can be expressed by[28]:

$$S_2 = \beta I_0 e^{-\beta x} e^{j\omega t} \quad (1-14)$$

where  $\beta$  is the light absorption coefficient,  $I_0$  is the intensity of the incident light,  $\omega$  is the angular frequency, and x is the coordinate. Although the time-dependent harmonic pressure response can be obtained by solving equation (1-17) analytically, it is only valid in case of one-dimensional problems. Analytical studies help in understanding the theory behind photoacoustic generation. Pressure wave propagation in 3D problems necessitates developing a numerical model for better accuracy.

### 1.9.1 Evaluation of optical absorption coefficient

The absorption coefficient, can be determined from the corrected transmittance, T ( $\lambda$ ) and corrected reflectance, R ( $\lambda$ ) by using the following formula[53] :

$$\alpha(\lambda) = \left(\frac{1}{l}\right) \ln \left[ \frac{(1-R)^2}{2T} + \sqrt{\frac{(1-R)^4}{4T^2} + R^2} \right] \quad (1-15)$$

Where  $l$  is the composite thickness. In this equation reflection(R) and transmission(T) are measured using spectrometer. Absorption coefficient can also be computed if volume fraction of absorptive material is known. This method will be explained in the next section.

## 1.9.2 Maxwell-Garnett Theory

Reflection and transmission depend on volume fraction of absorptive material. In case of CSNP, carbon volume fraction with carbon deposition times longer than 10 s, is estimated to be 9% [29]. Figure 1.17, shows absorption coefficients calculated by Maxwell-Garnett theory as a function of carbon solid volume fraction and wavelength. It can be observed that for CSNP/PDMS composite, the absorption coefficient is between  $0.9 \mu\text{m}^{-1}$  and  $2.3 \mu\text{m}^{-1}$  for 9% carbon volume fraction within the visible wavelength range. It is noted that Maxwell-Garnett theory takes the following equation:

$$\frac{\varepsilon_{eff} - \varepsilon_{PDMS}}{\varepsilon_{eff} + 2\varepsilon_{PDMS}} = V \frac{\varepsilon_C - \varepsilon_{PDMS}}{\varepsilon_C + 2\varepsilon_{PDMS}} \quad (1-16)$$

Where  $\varepsilon_{eff}$  is the effective dielectric constant for CSNP/PDMS nanocomposites,  $\varepsilon_{PDMS}$  is PDMS dielectric constant,  $\varepsilon_C$  is the dielectric constant for carbon and V is carbon volume fraction[54].

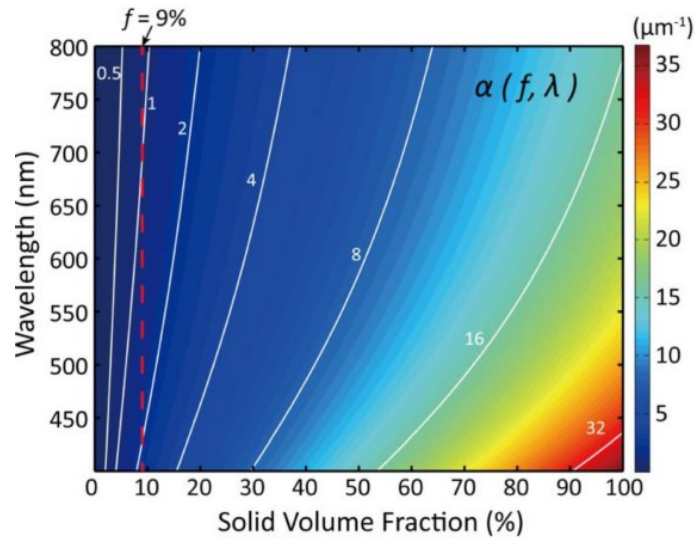


Figure 1.16 Absorption coefficients calculated by Maxwell-Garnett theory as a function of carbon solid volume fraction and wavelength [29]

## 1.9.3 Beer-Lambert's Law

The absorption coefficient ( $\alpha$ ) is defined by Beer-Lambert's law:

$$I = I_0 e^{-\alpha l} \quad (1-17)$$

Where  $I_0$  is the intensity of the incoming light and  $I$  is the remaining light intensity after passing through a medium with the thickness  $l$  [55]. The absorbance (A) of the medium is defined by:

$$A = -\log T \quad (1-18)$$

Where T is the transmittance. Absorption coefficient can be written as[56]:

$$\alpha = 2.303 \frac{A}{l} \quad (1-19)$$

Note that in the above equation, reflection is neglected. Thus, it is less accurate than equation (1-15).

#### 1.9.4 Temperature distribution for metal absorbers

Temperature distribution resulting from the absorption of a laser pulse at a surface of a metal is governed by differential equation for the heat flow in a semi-infinite slab with a boundary plane at  $z=0$ :

$$\nabla^2 T - \frac{1}{\alpha} \frac{\partial T}{\partial t} = -\frac{S}{k} \quad (1-20)$$

Where T (x, y, z, t) is the temperature distribution, q is the heat produced per unit volume per unit time, and k and  $\alpha$  are the thermal conductivity and diffusivity respectively. If the absorbed laser flux density is  $I_0$ , uniform across the irradiated area, and the laser is switched on instantaneously at zero time, from Carslaw and Jaeger, for 1D model, the solution of equation (1-25) is:

$$T(z, t) = \frac{2I_0(\alpha t)^{\frac{1}{2}}}{k} \text{ierfc} \left( \frac{z}{2(\alpha t)^{\frac{1}{2}}} \right) \quad (1-21)$$

Where

$$\text{ierfc}(\zeta) = \frac{1}{\sqrt{\pi}} e^{-\zeta^2} - \frac{2\zeta}{\sqrt{\pi}} \int_{\zeta}^{\infty} e^{-\zeta^2} d\zeta \quad (1-22)$$

Thus,

$$T(0, t) = \frac{2I_0(\alpha t)^{\frac{1}{2}}}{\sqrt{\pi}k} \quad (1-23)$$

The temperature distribution for more typical laser pulse shapes can be obtained by using Duhamel's theorem:

$$T(z, t) = \int_z^{\infty} \int_0^t \frac{I(t')}{I_0} \frac{\partial}{\partial t} \left( \frac{\partial}{\partial z} [T'(z', t - t')] \right) dz' dt' \quad (1-24)$$

Where  $T'(z, t)$  is the solution for the case of a step increase in absorbed flux density,  $I_0$ . Substituting equation (1-28) in equation (1-29) yields:

$$T(z, t) = \frac{1}{k\pi^{\frac{1}{2}}} \int_0^t \frac{I(t-t') \exp(-\frac{z^2}{4\alpha t'})}{t'^{\frac{1}{2}}} dt' \quad (1-25)$$

The temperature rise is higher for metals with lower thermal conductivity[50].

### 1.9.5 Temperature distribution for non-metal absorbers

The thermal diffusivity in non-metallic solids such as ceramics and plastics typically lies in the range  $10^{-7} - 10^{-6} \left[ \frac{m^2}{s} \right]$ , so that for the time scale of a Q-switched laser pulse of 6ns, the thermal length is of the order of nanometers. Thus, thermal conductivity effect can be neglected. In other words, optical penetration depths are considerably greater than thermal diffusion length in most common insulators.

### 1.10 Focusing ultrasound

To produce high-amplitude photoacoustic pulses, one can implement a focusing scheme, where photoacoustic pulses are concentrated to a (focal) spot. The photoacoustic amplitudes at the focal spot are significantly increased, which are characterized with a focal gain multiplied by photoacoustic amplitude right on the source. The higher focal gain is, the higher photoacoustic amplitude is. The focal gain is determined with the geometry of the photoacoustic transmitter (i.e.,  $f$ -number). Also, the focal gain is related to frequency bandwidth such that wide bandwidths (or short pulses) are desired for high focal gains[6].

The focusing function plays an important role in ultrasound therapeutic applications. Focusing provides a means of treatment that is deep-reaching and localized, with few secondary effects for the healthy tissues. One important application of focused ultrasound is to remove or disperse thrombolysis which is the formation of a blood clot in veins and arteries [57]. It has been shown that cavitation collapse is the primary cause of clot breakdown in focused ultrasound. In other words, each focused ultrasound pulse creates a cluster of microbubbles at the focus. The collapse of bubbles causes powerful micro-jets that can remove clots mechanically[58], [59].

### 1.10.1 Focusing in piezoelectric based transducers

This process of focusing leads to the creation of a focal region within the near zone, but not the far zone (figure 1.17). Focusing shortens the distance of the narrowest point of the beam from the transducer, that is to say, it reduces the near-zone length to a shorter value called the focal length. The beam beyond the focal region is divergent and so there is a reduction in lateral resolution of structures deeper than this point[60]. The width of a focused beam is determined by factors contained in the following equation:

$$\text{width of focused beam} \approx \frac{\text{focal length} \times \text{wavelength}}{\text{aperture}} \quad (1-26)$$

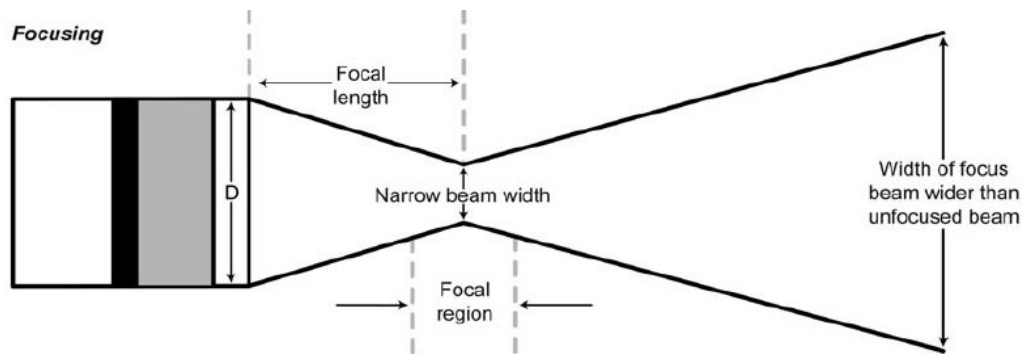


Figure 1.17 Focused piezoelectric transducer

Thus, a narrow, focused beam, and hence high lateral resolution, is obtained by:

- (i) Short focal length
- (ii) Short wavelength
- (iii) Wide aperture

### 1.10.2 Focusing technique in laser generated ultrasound

Piezoelectric transducers are not desirable for high intensity focused ultrasound (HIFU) due to their large focal spot size (>1mm) which makes it challenging for high-precision targeted therapy[32]. Several researches have been conducted to develop a high frequency focused ultrasound using carbon/polymer nanocomposite on a transparent concave substrate[31], [61]. Figure 1.18, shows a concave lens coated with CSNP/PDMS layer. Guangxin Ding et al, used

plano-concave lens with a diameter of 16 mm and radius of curvature of 10.33 mm as their substrate to generate positive and negative acoustic pressure of 14MPa and 8MPa respectively. The result is plotted in figure 1.19.[61].

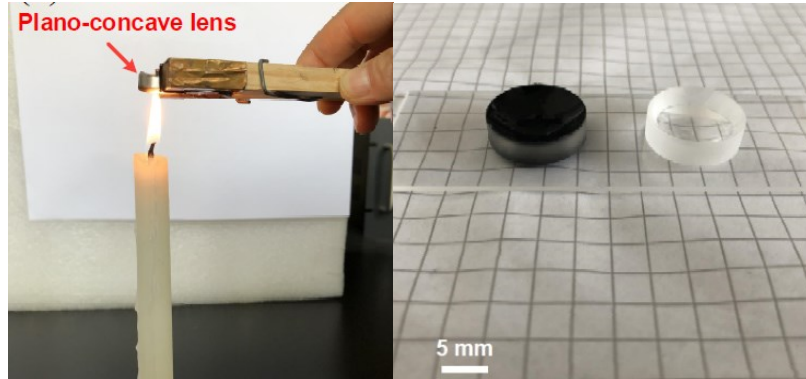


Figure 1.18 Deposition of CSNP on a plano-concave lens [60]

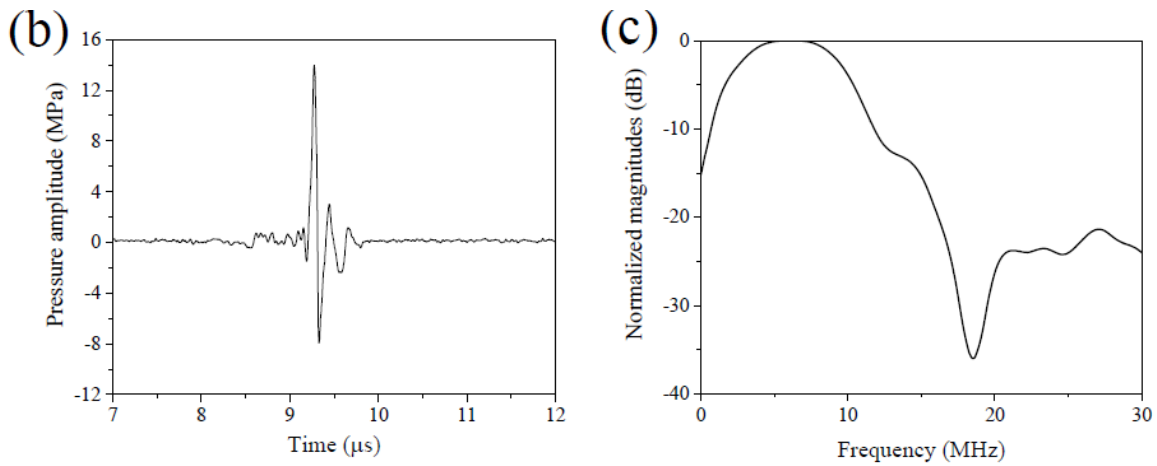


Figure 1.19 Time and frequency response of CSNP/PDMS transducer fabricated on Plano-concave lens [60]

For intravascular therapies such as thrombolysis, drug delivery, and plaque removal optical fiber-directed photoacoustic transmitters have been developed to generate high pressure shock waves[31]–[33], [62]. In these transducers, carbon/PDMS composite is coated on a concave lens.

Having discussed the state of the art in laser generated ultrasound (LGU), the relative merits and demerits of the use of composites for LGUs next we will discuss the scope of this thesis in the next part.

substrate	Composite material	Radius of curvature [mm]	Lens diameter[mm]	Acoustic pressure [MPa]	Laser energy[mJ]	Laser fluence[mJ/c m <sup>2</sup> ]
Plano-concave lens[25]	CB/PDMS	12.4	12.5	18/-12	20	-
Fiber optics[31]	CSNP/PDMS	1.3	2	10.9/-5.7	2	1.5
Plano-concave lens[61]	CSNP/PDMS	10.3	16	14/-8	4.9	-
Fiber optics[32]	CSNP/PDMS	4.71	6	33/-5.7	-	29.7
Plano-concave lens[63]	CNT/PDMS	5.5	6	22/-10	12	42.4

*Table 1.2 Published papers on laser generated ultrasound using carbon/PDMS transducer*

### 1.11 Thesis motivation

From the extensive review of LGU, there have been significant amount of experimental work but very few works on the theory behind LGU composites. On the other hand, almost all the works in the literature utilize high power lasers with repetition rates of few hertz for the experiments. We aspire to work on high repetition rate LGUs, as high repetition rate lasers are currently used in industry for manufacturing and they cost lower than the high-power lasers. Should the feasibility study for high repetition rate LGU needs to be performed, fundamental physics behind LGU should be understood.

### 1.12 Objective and scope of the thesis

The aim of this work is to utilize high repetition rate lasers for ultrasound generation. To this extent the objective and scope of the work have been formulated.

- To understand the fundamental physics behind LGU composites using optical absorbers.
  - Simulation of the laser generated ultrasound with CSNP/PDMS composite
  - Validating the simulation results with results available from the literature
- To test the robustness of the developed model
  - Validating of model result with other composite materials
- Extend the model parameters to include high repetition rate lasers

- To prepare various composite samples to experimentally determine the absorption coefficient
- Perform experiments using high repetition rate laser to identify the damaged threshold

### **1.13 Thesis organization**

The first chapter of the thesis provides an extensive critical review of the literature, from which the thesis motivation and the objectives were defined. In the second chapter preliminary model with data from literature was presented. Different simulation methodologies were tested and the simulation results were compared with experimental studies. The difference between the result from simulation and experiment were analyzed. Subsequently, in the third chapter, a robust model was developed that included the geometry of hydrophone. To test the robustness of the model the model results were validated for different composites, different thicknesses and different laser fluences. Chapter four of the thesis discusses the feasibility of high repetition rate LGU. For this purpose, CSNP/PDMS composite transducers were fabricated. Experiments were then performed to identify the damage threshold of composite as well as the absorption coefficient. The data from the experiments were used for the feasibility study. The conclusion from each section of thesis have been summarized and presented in chapter 5. In addition, the potential extension of current work was presented.

## CHAPTER 2. Numerical study of LGU

### 2.1 Introduction

In this chapter, the theory and design of the numerical model for ultrasound wave in carbon/PDMS composite will be presented. COMSOL Multiphysics v5.6 will be used to establish a 2D-axisymmetric finite element analysis (FEA) to simulate the photoacoustic generation process. The result from the simulation carried out in this work will be validated by experimental studies performed using candle soot nanoparticles/PDMS transducer by Wenbin Huang et.al [28].

### 2.2 2D simulation of laser induced ultrasound

The mechanism behind the LGU could be better understood with a simulation of 2D model in COMSOL. 3D model was avoided due to excessively long computation time. In this work, we investigate how a commercially available Finite Element software can serve as a single platform for simulating a LGU transmitter that couples the electromagnetic, thermodynamic and acoustic pressure physics involved in photoacoustic phenomena. As shown in figure 2.1, pulsed laser beam is shined on a carbon/PDMS composite that is immersed in water. As the composite absorbs optical irradiation energy, it heats up and induces mechanical waves. Owing to thermal expansion, acoustic wave is excited and this propagates inside water.

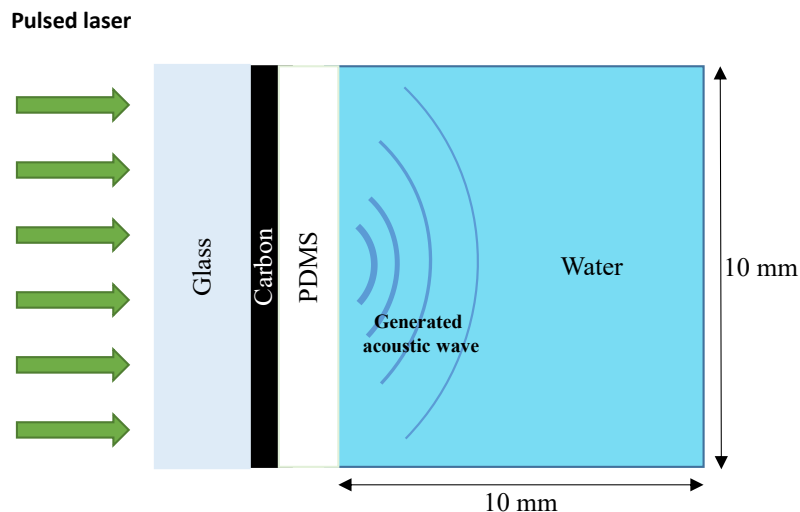


*Figure 2.1 Schematic of laser induced ultrasound using carbon/PDMS transducer and its propagation in water*

## 2.3 Simulation methodology

### 2.3.1 Geometry

The photoacoustic generator is a rectangle along laser beam pulse composed of carbon and PDMS placed on a 1mm glass substrate that radiates acoustic signal towards the front open space. The glass substrate does not play a role in the simulation and it only serves as a backup material to keep the composite fixed on the left side. The schematic of the model is depicted in figure 2.1. Domain dimensions in the 2D model can be seen in table 2.1.

Domain	Glass	Carbon	PDMS	Water
Width [mm]	10	10	10	10
Thickness [ $\mu\text{m}$ ]	1000	6.5	18	10000

*Table 2.1 Dimensions of domains in finite element model in 2D environment*

### 2.3.2 Material properties

All the materials used in the simulation are chosen from COMSOL library. In the preliminary investigation of photoacoustic ultrasound, absorber and thermal expansion part of transducer are considered separately. However, the mechanical properties of carbon are identical to that of PDMS[28]. This assumes that the acoustic property is dominated by the PDMS matrix. The assumption is reasonable because the CSNPs occupy less than a few percent in volume fraction in the CSNP-PDMS composite. In addition, candle soot nanoparticles are known to have a porous structure that allows the PDMS solution to penetrate the CS (candle soot) layer. Therefore, this composite layer possesses mechanical properties of PDMS and optical property of candle soot nanoparticles. In table 2.2, list of materials used are shown.

### 2.3.3 Physics

Photoacoustic phenomena consist of four phases. First, laser pulse is irradiated on the composite where most of the energy is absorbed and attenuated. The energy deposited by the laser beam propagation in the absorbing medium is calculated and will be used in the heat transfer mode where the temperature distribution in composite is obtained. Next, thermoelastic expansion is modeled in the structural mechanics module. Finally, the displacement of the composite is supplied as an

input to the pressure acoustics module in the form of normal acceleration. Figure 2.2 illustrate the approach of the simulation.

	Absorption coefficient [1/m]	Coefficient of thermal expansion [1/K]	Heat capacity at constant pressure [J/ (kg K)]	Density [kg/m <sup>3</sup> ]	Poisson's ratio	Sound velocity [m/s]	Thermal diffusivity [m <sup>2</sup> /s]
PDMS	-	9.00E-04	1460	970	0.49	1076	1.13E-07
Water	-	2.10E-04	-	998	-	1480	1.46E-07
CSNP	1.00E+06	9.00E-04	1460	970	0.49	1076	1.13E-07
CNF	1.80E+05	-	1460	970	0.49	1076	1.13E-07

Table 2.2 Material properties used in computer simulation with Young's Modulus of 750 KPa, and a Poisson's ratio of 0.49 for the composite.

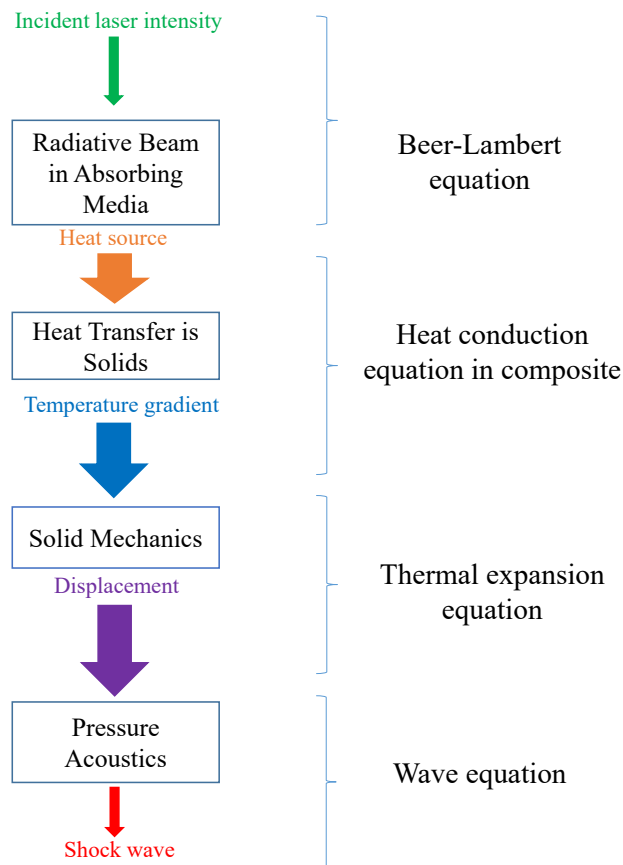


Figure 2.2 Acoustic pressure generation process

The beam intensity is determined using the Beer-Lambert law which can be found in Radiative Beam in Absorbing Media (RBAM) interface in COMSOL. This node calculates the radiative intensity of incident beams propagating in an absorbing medium using the equation below:

$$\nabla I_i = -\beta I_i \quad (2-1)$$

Where  $I_i$  is the intensity of  $i^{th}$  beam and  $\beta \left[\frac{1}{m}\right]$  is the absorption coefficient. The incident laser pulse is assumed to have Gaussian spatial and temporal profile and applied in the front boundary of absorbing medium. This boundary condition is expressed as:

$$I(y, t) = I_0 e^{-\left(\frac{t-t_0}{\sigma}\right)^2} e^{-\frac{2(y-D)^2}{r^2}} \quad (2-2)$$

Where  $I_0 \left[\frac{W}{m^2}\right]$  is the peak incident intensity at the center of the beam calculated from laser energy  $\left[\frac{mJ}{cm^2}\right]$ ,  $t_0$  [ns] is the time where pulse is centered at,  $y$  [mm] is the radial direction and  $D$  [mm] is the beam radius. Spatial and temporal profile of the incident laser intensity is depicted in figure 2.3.

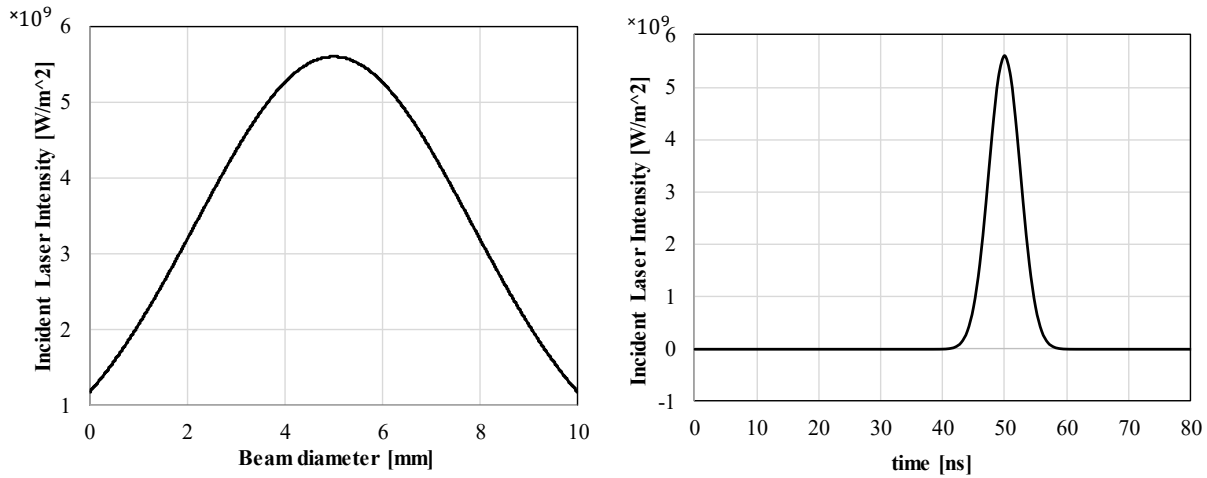


Figure 2.3 Spatial (left) and temporal (right) distribution of incident laser intensity

Laser intensity decays exponentially from a maximum at the surface,  $z=0$  to a negligible value at  $z=6 \mu\text{m}$  as a result of material light absorption. Intensity distribution calculated from Beer-Lambert equation at the center of the beam is shown in figure 2.4. The graph is plotted at 50 ns when intensity is at its maximum according to the time dependent profile in figure 2.3(right).

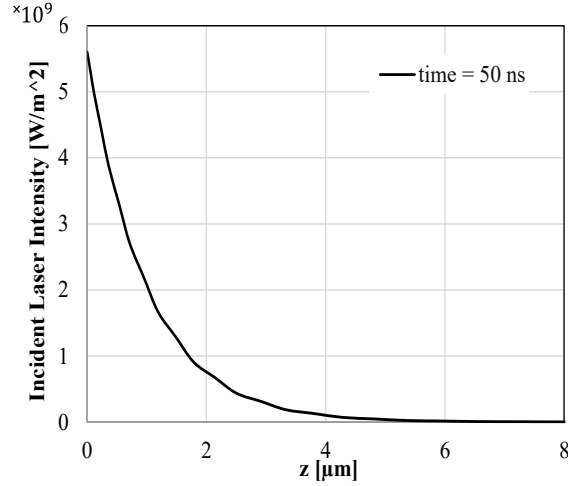


Figure 2.4 Exponential distribution of laser intensity as it is absorbed by composite

The temperature of composite changes as a result of energy absorption. The temperature distribution can be obtained using heat conduction equation under “heat transfer in solids” interface in COMSOL:

$$\rho C_p \frac{\partial T}{\partial t} - \nabla(k\Delta T) = Q \quad \text{where } Q = \sum_i \beta I_i \quad (2-3)$$

Where  $Q$  [ $\frac{W}{m^3}$ ],  $\rho$  [ $\frac{kg}{m^3}$ ],  $C_p$  [ $\frac{J}{kg.K}$ ],  $k$  [ $\frac{W}{m.K}$ ] and  $T$  [K] are the heat source, density, the specific heat capacity, thermal conductivity and temperature respectively.

As a result of temperature changes within the absorber, composite undergoes a thermoelastic expansion which is modelled using ‘solid mechanics’ module. In order to couple heat transfer and solid mechanics modules, thermal expansion Multiphysics is added in the model from which the thermal stress is calculated as below:

$$\varepsilon_{th} = \beta_T (T_{ref} - T) \quad (2-4)$$

Where  $\beta_T$  [ $\frac{1}{K}$ ] is coefficient of thermal expansion and  $T_{ref}$  is the reference temperature. Finally, ultrasound induced in the surrounding medium can be solved by the COMSOL “pressure acoustic” mode. This module solves below acoustic wave equation in the time domain.

$$\frac{1}{\rho c^2} \frac{\partial^2 P}{\partial t^2} - \nabla \left( \frac{1}{\rho} \nabla P \right) = 0 \quad (2-5)$$

The displacement of the composite evaluated by thermal expansion equation will be used (in the form of acceleration) as the input in the acoustic wave equation. This can be done by adding the ‘acoustic-structure boundary’ Multiphysics which is described as follows:

$$-\vec{n} \cdot \left( \frac{1}{\rho} \nabla P \right) = -\vec{n} \cdot \frac{\partial^2 u}{\partial t^2} \quad (2-6)$$

Where ‘u’ is the structural acceleration and ‘n’ is surface normal. Figure 2.5 summarizes all the physics interfaces applied to the model. Having given an idea into the modality and general physics behind the simulation process, the next section will give insight into the boundary conditions used for simulation.

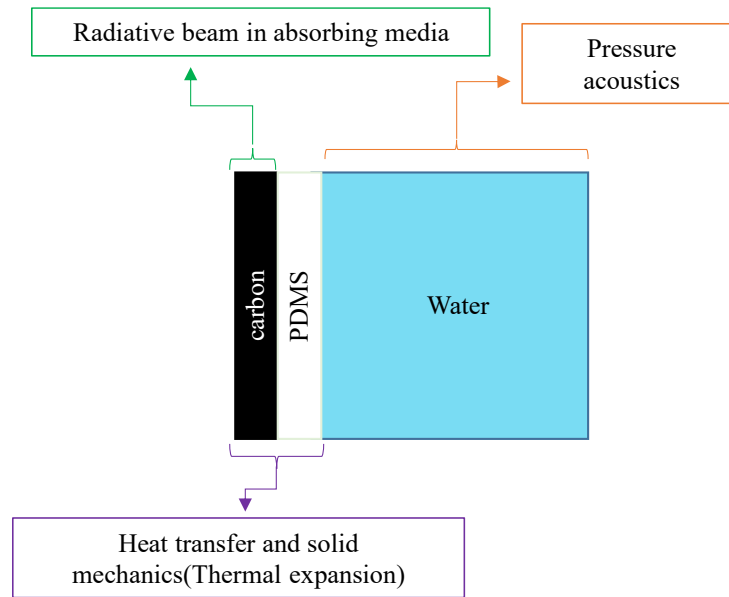


*Figure 2.5 Physics applied to the domains*

### 2.3.4 Boundary conditions

Boundary conditions are selected as per model requirement. Figure 2.6, illustrates the boundary conditions and their corresponding surfaces. The laser intensity is defined on the incident surface (surface 1) of composite as the incoming heat flux using equation (2-2). All the other boundary of carbon domain is set to be “transparent surface” which indicates that all the outgoing beams traveling from the medium to the exterior (PDMS) leave the domain without depositing any energy at this boundary.

Since “heat transfer” module is implemented for both carbon and PDMS layer, they will be treated as a single domain. Care should be taken when defining the heat source as it is only applicable for carbon domain. All the boundaries can be left at default thermal insulation with the exception of illuminated face. At the illuminated boundary, the temperature will rise significantly, and radiative heat loss can occur. This can be modeled with the “Surface-to-ambient radiation” boundary condition, which takes the ambient temperature of the surroundings and the surface emissivity as inputs. These two boundary conditions are defined as follows:

$$-n \cdot q = 0 \quad \text{Thermal insulation} \quad -n \cdot q = \varepsilon \sigma_s (T_{amb}^4 - T^4) \quad \text{surface to ambient temperature}$$

Where  $n$ ,  $q$ ,  $\varepsilon$ ,  $\sigma_s$  and  $T_{amb}$  are surface normal, heat flux, surface emissivity, Stefan-Boltzmann constant and ambient temperature respectively.

All boundaries of absorber domain are fixed except the interface between water and the composite which is the input load for acoustic physics and has been described in section (2.3.3). Other three faces of water tank are set as “sound hard boundary”. “Sound hard boundary” is the default boundary condition used if no boundary condition is specified at a given boundary. Conceptually a sound-hard boundary is equivalent to a closed end of a tube. Since no forward motion is possible, the pressure accumulates and reaches its maximum at the double of the incident pressure. Note that mathematically this condition is identical to the “Symmetry” condition. This boundary condition will be modified in section 2.4 where PML layer will be introduced to account for infinite extend of water domain, as it is the case in the real experiment.

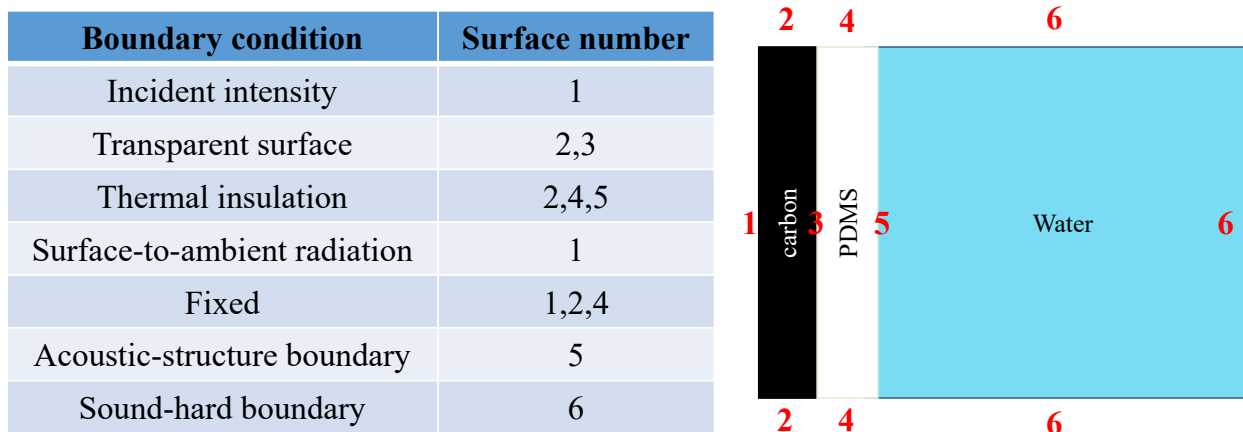


Figure 2.6 Boundary conditions in 2D model

### 2.3.5 Parameters of the numerical model and assumptions

The material parameters and validation of the numerical models are established from the references [28][9]. The emissivity of the composite is assumed to be 0.7 which is taken from the literature [64]. The initial condition is set as zero for all the partial differential equation (PDE) equations involved in the model. The incident laser intensity has Gaussian temporal profile [64]. For accurate simulation, we assume that the incident laser light intensity follows a Gaussian distribution with respect to distance from the origin in addition to temporal distribution. Both temporal and spatial profile of intensity has been discussed in section (2.3.3). “ $\sigma$ ” in the time domain profile is dependent on pulse width ( $\tau$ ) and is evaluated with equation 2-7, while the peak intensity calculated using 2-8: Table 2.2 shows the parameters used in the simulation.

$$\sigma = \frac{\tau}{2\sqrt{-\ln\frac{1}{2}}} \quad (2-7)$$

$$I_0 = \frac{E_0}{\sqrt{\pi} \sigma} \quad (2-8)$$

Laser fluence, $E_0$ [mJ/cm <sup>2</sup> ]	3.57
Pulse width, $\tau$ [ns]	6
Standard deviation, $\sigma$ [ns]	3.6
Time shift, $t_0$ [ns]	50
Laser power density, $I_0$ [W/m <sup>2</sup> ]	5.59e9
Emissivity, $\varepsilon$	0.7
Laser spot radius, $D$ [mm]	5
Maximum frequency, $f$ [MHz]	10

*Table 2.3 Simulation parameters for 2D model*

A monitoring point 4.2mm away from the acoustic source, representing a position where a pressure sensor (hydrophone) will be placed in the real experiments.

### 2.3.6 Mesh and study configuration

The next step for the simulation is to define the mesh. The 2D model is composed of about 50,000 elements and it is too fine to show here. The elements are refined progressively in two regions of interest. (1) Maximal mesh element size of 0.4 mm in the region of the absorption layer. (2) The

adjacent area between the absorption layer and the water with element growth rate of 1.2 and maximum element size of 0.2 mm. “Mapped” mesh has been used for carbon layer and the other two domains have been meshed using “free triangular” elements. Figure 2.7 depicts the mesh distribution for all three domains.

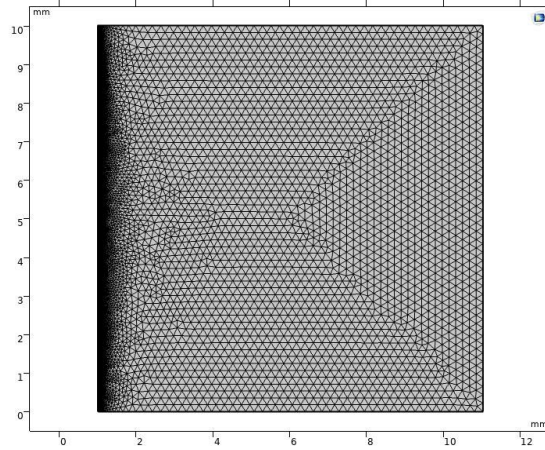


*Figure 2.7 Mesh distribution in 2D model*

The acoustic pressure has been evaluated using a time dependent solver. In solver parameters, time ranges from 0 to 6  $\mu\text{s}$ . It should be noted that the accuracy of a time-dependent model solving for any kind of wave-type model is limited by how well the finite element mesh resolves the waves in space and by how well the time steps resolve the temporal variations. It is hence reasonable to simulate a poorly configured model as a first part of the numerical study to understand the importance of mesh size.

The time step should resolve the wave well in time. Longer time steps will not make optimal use of the mesh, and any shorter time steps will lead to longer solution times with no considerable improvements to the results. The relationship between wave speed,  $c$ , maximum mesh size,  $h$ , and time step length,  $\Delta t$ , is known as the CFL number:

$$CFL = \frac{c\Delta t}{h} \quad (2-9)$$

This can be re-written in terms of the frequency  $f$ , and  $N$  the number of elements per local wavelength:

$$CFL = fN\Delta t \quad \Delta t = \frac{CFL}{Nf} \quad (2-10)$$

Where “N” denotes the number of elements per wavelength and it’s assumed to be equal to 6. The CFL number should be less than 0.2 and a value of 0.1 proves to be near optimal[65]. This will generate a manual time step  $1/(60 \times f)$ , which if you mesh with 6 elements per wavelength corresponds to a CFL number of 0.1. In the next part, the preliminary result for roughly meshed 2D model will be discussed.

### 2.3.7 Output acoustic pressure of 2D model

Figure 2.8 shows the propagation of pressure wave from the source at the different instances of time. The total computation time was about 35 minutes, which is quick due to course mesh configuration of the water domain. The source is represented by the acceleration of the interface between the composite and the water and it is located at the left side of the geometry. The composite dimensions are relatively small compared to the water domain hence it is not noticeable in the model. The propagation time of the acoustic wave can be calculated by the propagation distance (10mm) divided by speed of sound in water (1480 m/s), which is in accordance with the numerical simulation (about 6.7  $\mu$ s).

However, the pressure amplitude does not match the experimental result. To have a better comparison, a monitoring line 4.2mm away from the acoustic source was considered in the simulation to represent a position where a hydrophone will be placed in the real experiments. The average acoustic pressure was then computed on this line to be compared to the experimental result. The length of the monitoring line is set as 200 $\mu$ m and equal to the hydrophone aperture diameter. The result as shown in figure (2-9) was compared with the published experimental work and a big difference in the pressure profile was observed[28].

The presented acoustic pressure is 6 times less than the experimental result carried out by Wenbin Huang et.al. This is mainly attributable to course mesh size and the fact that spatial elements do not permit the features of the solution to evolve accurately. The required mesh size depends on the frequency of the ultrasound and is related to Nyquist sampling of signals [66]. Therefore, a better mesh configuration is required to meet Nyquist criteria. In the next section a 2D-axisymmetric model with sufficiently fine meshes will be constructed.

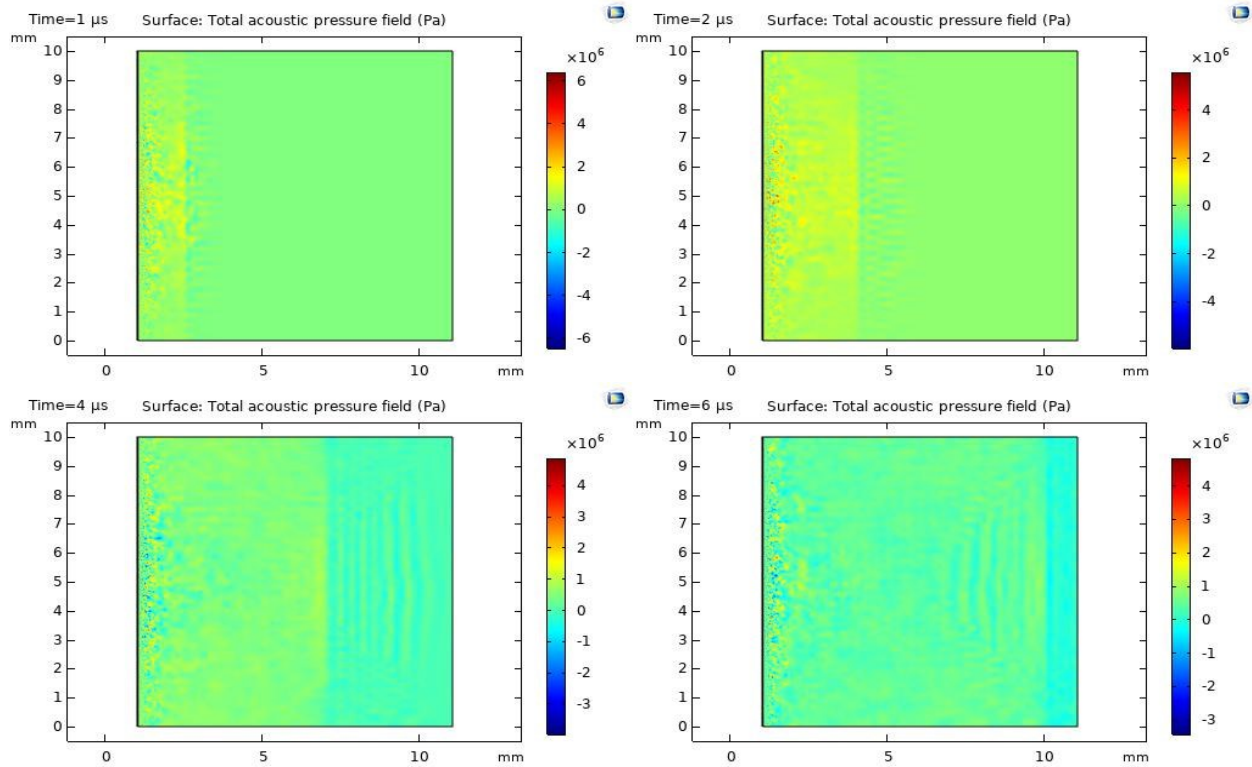


Figure 2.8 Acoustic pressure propagation in water domain at  $t=1$  to  $t=6$  microsecond

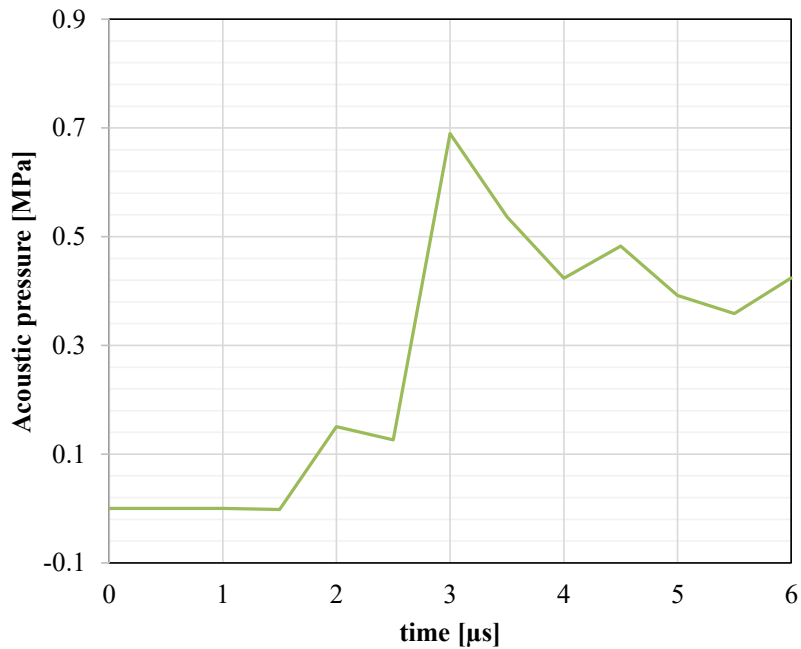
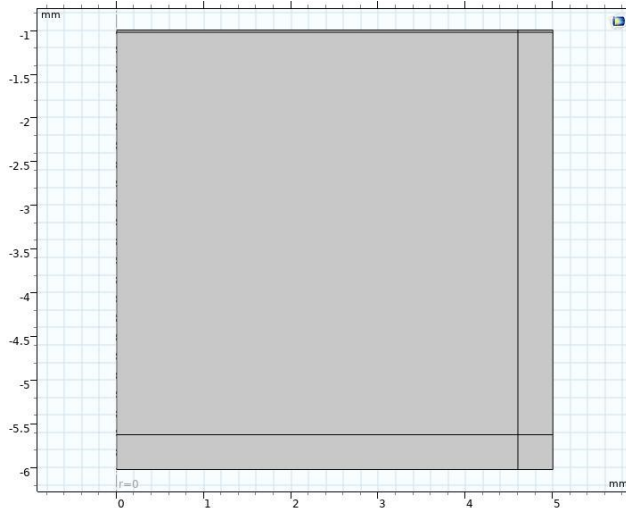


Figure 2.9 Average acoustic pressure at 4.2 mm away from the substrate

## 2.4 2D axisymmetric model simulation

As it was discussed in previous section both time steps and mesh sizes play a huge role in the accuracy of any wave problem. Therefore, both time-domain and spatial-domain need to be divided into small intervals and elements. As the number of dimensions of a FE model increases, the number of nodes generally increases and so does the time to compute a solution. As a result, there is always pressure to minimize the number of spatial elements and time-steps to allow calculations to be performed quickly or in a reasonable time. To reduce the computation time 2D-axisymmetric model was proposed where 5x5mm square is revolved about the laser axis. Figure 2.10 shows the geometry used in the 2-dimensional axisymmetric FE model.



*Figure 2.10 2D- axisymmetric FE model*

### 2.4.1 Geometry

Some modifications in the geometry have been made to generate more accurate and more time efficient computation in 2D-axisymmetric model. In the next part, these modifications will be explained elaborately.

#### 2.3.1.1 Single layer composite

For simplicity, the composite layer is represented by a single layer with the total thickness of 25  $\mu\text{m}$ . This assumption will not have a noticeable effect on the result since intensity is negligible in the pure PDMS layer as it is mostly absorbed within carbon layer. Exponential decay of the

intensity as it penetrates inside the composite can be observed in figure 2.4. Consequently, the heat generation takes place within approximately  $6\mu\text{m}$  of the composite thickness regardless of how it is modeled in the simulation

### 2.3.1.2 PML layers

The concept of a perfectly matched layer (PML) as an absorbing layer was introduced by Bérenger [67]. The PML provides absorption of propagating waves without introducing reflections from the interface between the PML and the physical domain. In the current study, only a small part ( $10 \times 10\text{mm}$ ) of water environment has been modeled since the implementation of the extended domain as in the real experiment is not feasible in the simulation. Using the default boundary condition of “sound-hard boundary”, treats the water domain as a closed tube and only allows for forward motion of the wave. To overcome this problem, PML is implemented to provide a non-reflecting region. A PML, however, is not a boundary condition. The PML is an artificial additional absorbing layer that enlarges the original simulation grid. As a wave enters the absorbing layer, it is attenuated by an absorption and decays exponentially[67]. This layer can be found in “Artificial Domains” under “Definitions” in COMSOL model tree. To generate mesh, it is recommended to use “Mapped” mesh with at least 8 mesh layers[68].

### 2.4.2 Mesh

In order to resolve the acoustic wave accurately, mesh size has been chosen in such a way that it can properly predict the physical behavior of the propagating wave. The mesh is however less dense outside the propagation area of interest, to reduce the computation time. The mesh size is set as  $h = \frac{1480}{6 \times 10[\text{MHz}]} = 25 \mu\text{m}$  on the left side of the water domain where maximum acoustic pressure is generated. Total number of elements is about 14000 consists of “mapped” and “free triangular” mesh. Figure 2.11 illustrates the mesh distribution for 2D-axisymmetric model.

### 2.4.3 2D-axisymmetric result

In the 2D-axisymmetric model factors such as material properties, boundary conditions and time-step were retained from the previous 2D model. However, as it was discussed in previous section, mesh distribution was adapted in such way that it can properly predict the behavior of the acoustic wave.

“Time dependent” solver was used to compute the solution over time. The computed acoustic pressure can be seen in figure 2.12. The result presented in figure 2.12 closely compares with the work of Wenbin Huang in which maximum acoustic pressure was measured to be 4.8MPa [28].

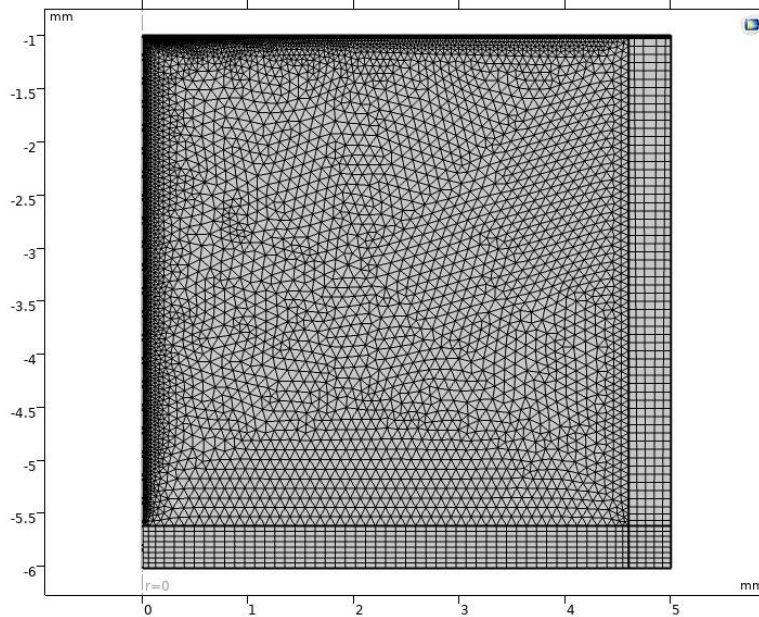


Figure 2.11 Mesh distribution in 2D-axisymmetric model

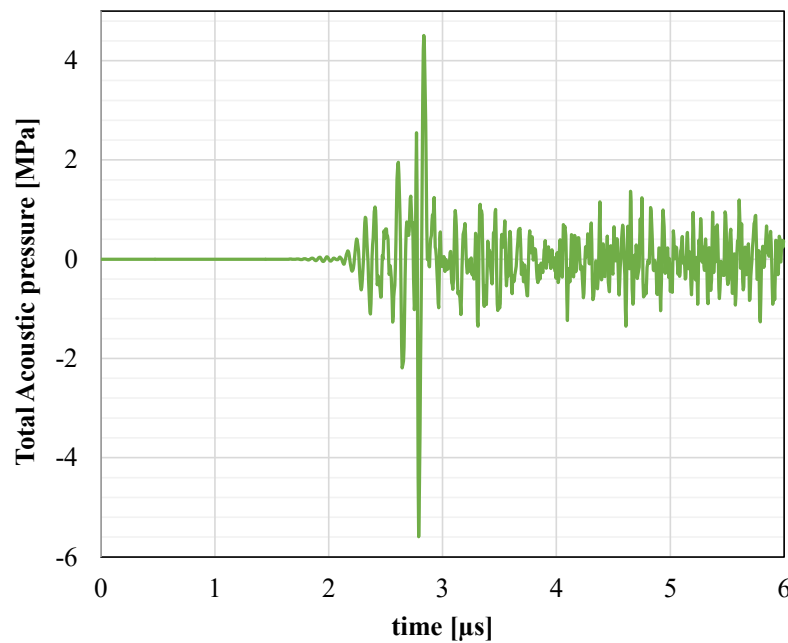


Figure 2.12 Average acoustic pressure of 2D-axisymmetric model at 4.2 mm away from the transducer

## **2.5 Summary**

2D simulation was performed on CSNP/PDMS composite LGU with COMSOL Multiphysics. The material properties of the composite were taken from the literature. The geometry, boundary conditions and meshing were defined. The physics for laser heat transfer, expansion of material and acoustic pressure generation was defined. The input parameters were selected from literature and the preliminary pressure output was extracted from the model similar to the experiments. However, significant shift in the result was found in comparison to the result from experiments. Mesh refinement was performed and 2D model was changed to 2D-axisymmetric to reduce the computation time. While there was improvement in the result further work on the model is required which will be discussed in the next chapter.

## CHAPTER 3. Model refinement and validation

### 3.1 Introduction

In previous chapter, the mechanism of laser generated ultrasound and its implementation in a finite element analysis (FEA) software (COMSOL Multiphysics) was explained. In this chapter, numerical model of candle soot nanoparticle (CSNP), carbon nanofiber (CNF) and carbon black (CB) will be demonstrated and compared with the experimental result. To have a better prediction of real case scenario, a modified geometry is suggested to obtain a more realistic evaluation of acoustic pressure. A mesh refinement will be performed to gain confidence in the model and results. In the last part of this chapter, utilizing the proposed numerical model, the relationship between generated acoustic pressure with variation in input parameters like composite thickness, laser energy density and pulse width will be investigated.

### 3.2 Model refinement

In this section, acoustic pressure of carbon black (CB)/PDMS and Carbon nanofiber (CNF)/PDMS will be investigated and the results will be compared with experimental study in the literature. First, a new approach will be posited in which transient behavior of the material is considered in “solid mechanics” interface. As it was shown in our primary result, “quasi-static” option was chosen in “solid mechanics” module, which returns faster computation at the cost of less accurate result. The solution of “solid mechanics” physics was 11% slower when inertia terms were included in the model.

#### 3.2.1 Structural transient behavior

The temperature increase in the absorber layer occurs in few nanoseconds and it causes a rapid expansion of the PDMS. The mechanical behavior of PDMS was described by the physics interface “solid mechanics” in COMSOL Multiphysics. This adds a domain condition governed by the following equation:

$$\rho \frac{\partial^2 \mathbf{u}}{\partial t^2} = \nabla \cdot \mathbf{S} + \mathbf{F}_V \quad (3-1)$$

Where  $u$ ,  $S_T$  and  $F$  are displacement, total stress and volume force respectively. As it can be observed, this equation contains the inertial terms  $\frac{\partial^2 \mathbf{u}}{\partial t^2}$ , which was neglected in section 2.3.3.

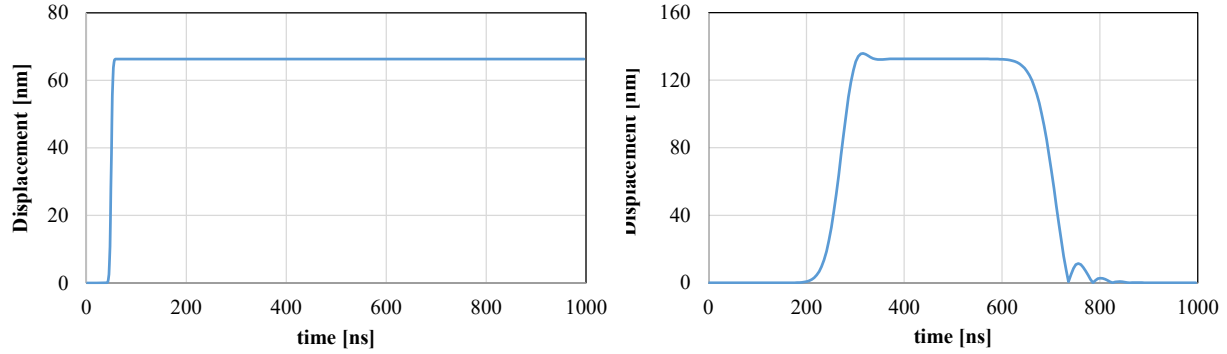


Figure 3.1 Time- dependent displacement of CSNP/PDMS composite when selecting "Quasi-static"(left) and "include inertial term" (right)

To obtain a more accurate result, we include this term by selecting “include inertial term” in the physics setting. Selecting this option enables the solver to account for the fast variation in time. As it is shown in figure 3.1, “include inertia terms” yield the transient response, which is desirable for a wave-type problem. In next part, material parameter’s variation will be explained for each substance.

### 3.2.2 Absorption coefficient of CB and CNF

The absorption coefficient of CB and CNF is usually not given directly. For absorbers such as CNF, CSNP and CNT, spectrometer is utilized to measure the optical density (OD) and reflection of the film[69][12]. Given the thickness of absorber layer, the absorption coefficient can be calculated. Table below shows the optical properties of CB and CNF.

	Thickness [μm]	Reflection [%]	Transmission [%]	Optical density [au]	Absorption coefficient [1/μm]
CNF[12]	25	4.13	0.001	5	0.45
CB[9][70]	30	-	-	2	0.15

Table 3.1 optical properties of CNF and CB

Absorption coefficient can be calculated using  $\alpha = 2.303 \frac{A}{t}$  where A and t are the optical density (absorbance) and thickness respectively[71].

### 3.2.3 Two-layer approach in numerical model of CNF/PDMS

Unlike CSNP, CNF possess lower absorption coefficient which means that light is able to penetrate more with less attenuation. Consequently, it is more realistic to consider two layers, one for the absorber and one for the pure PDMS. It is worth noting that CB is treated similar to CSNP since pure PDMS layer does not exist and fabrication process is done in a single step where the CB/PDMS solution is coated on a substrate[72].

### 3.2.4 Displacement profile of PDMS for different absorbers

Since the acoustic pressure is dominated by the expansion of PDMS, the displacement of a point at the interface of the PDMS and water domain has been investigated. The monitoring point is depicted in figure 3.2.

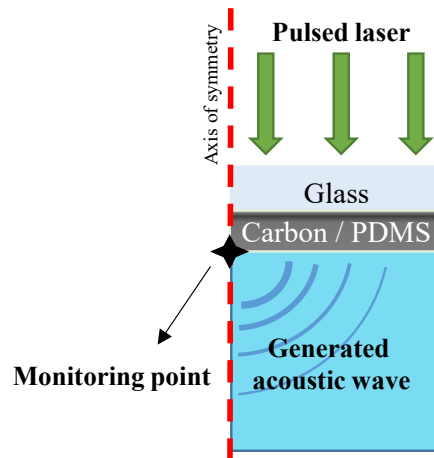


*Figure 3.2 : Schematic of the 2-D model and the point at which displacement is evaluated*

Figure 3.3, shows the displacement profile of the different composite. It should be noted that the laser parameters are identical for all three materials.

As it can be observed, CSNP/PDMS expands more compare to the other two, due to its higher absorption coefficient. It is noted that the time at which expansion starts, varies in different composites which is attributed to their different thicknesses. It should be noticed that the raise time in the displacement of CSNP/PDMS composite is small compared with CB and CNF. This indicates that, heat transfer and consequently thermal expansion is faster in CSNP which leads to a higher acoustic pressure. In the next section generated acoustic pressure will be presented.

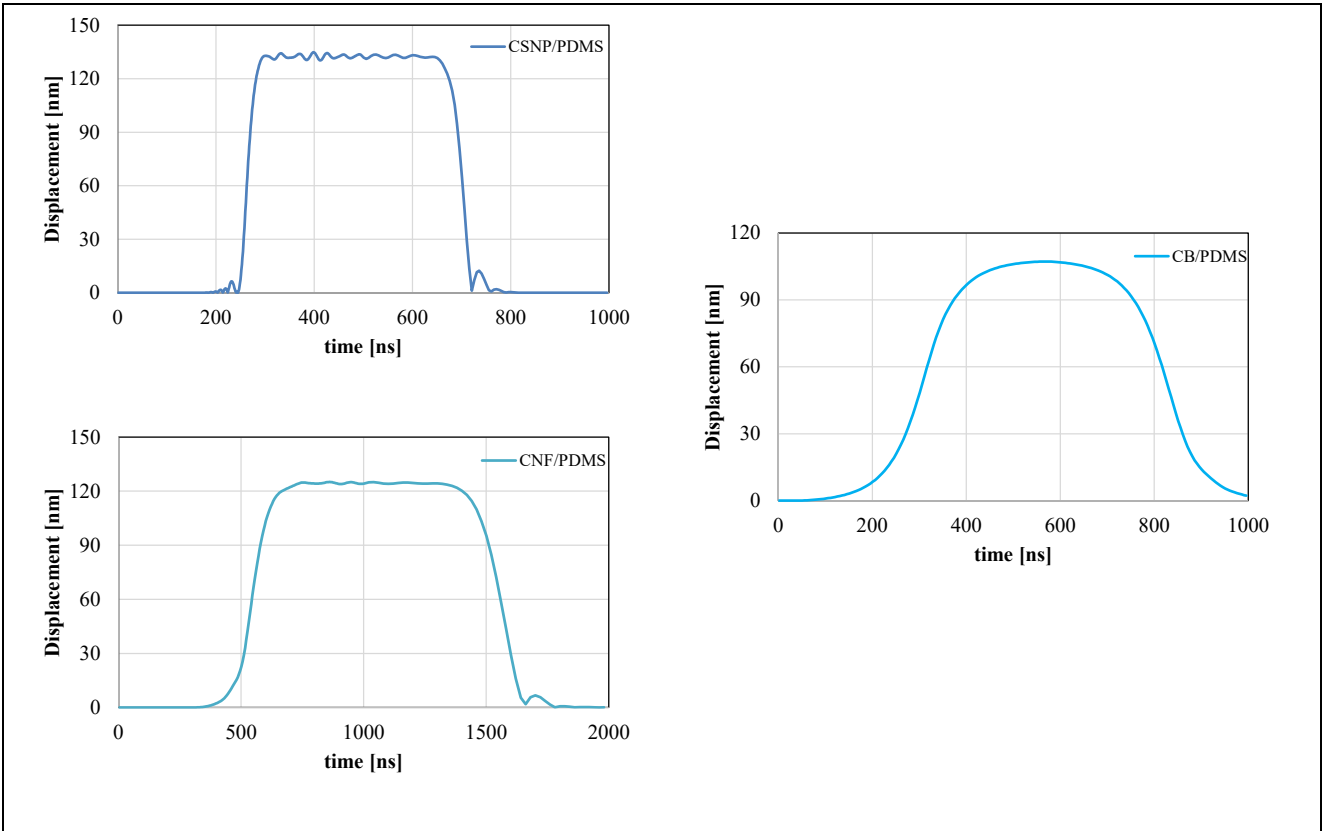
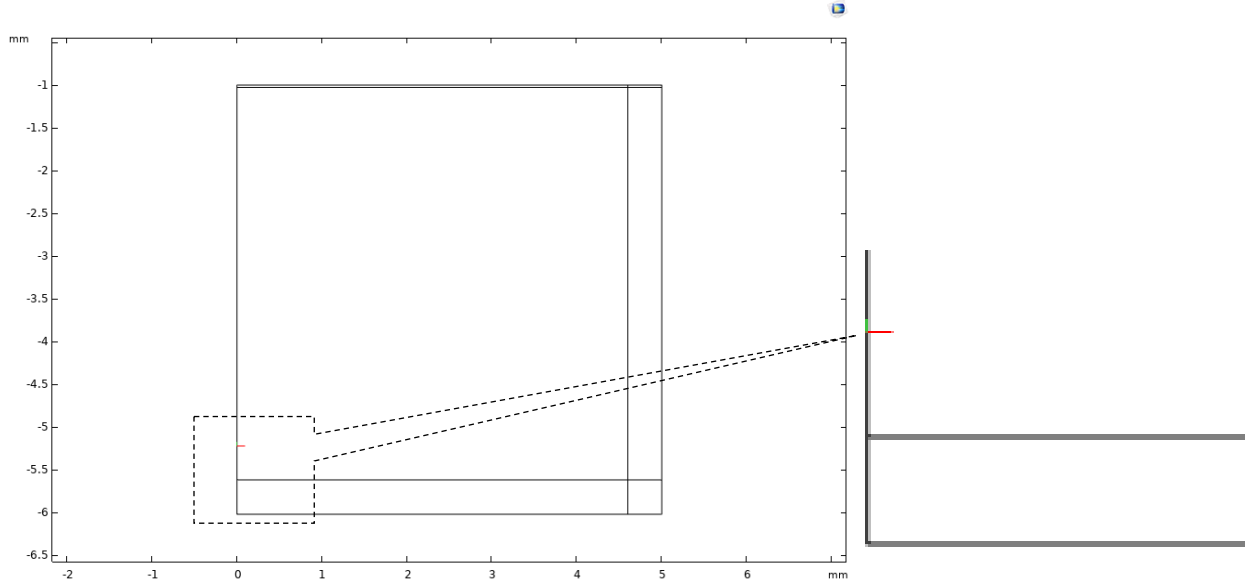


Figure 3.3: Figure 3.3 Displacement profile of the monitoring point in different composite material

### 3.2.5 Generated acoustic pressure in CSNP, CNF and CB embedded PDMS and its comparison with experimental result

As it was discussed in chapter two, a line is positioned at a distance of 4.2mm away from the composite to represent the approximate surface of the hydrophone in the experiment. Since the numerical model is symmetric along the center, the monitoring line is revolved about its center that generates a circle with a radius equal to the radius of the hydrophone. The acoustic pressure in the numerical model is obtained by taking an average along the monitoring line. The red line, shown in the enlarged insert as part of figure 3.4, represents the surface of the hydrophone where is the pressure is measured.



*Figure 3.4 2-D axisymmetric model in COMSOL.*

It should be noted that the mesh size and time step are identical for all the composites and have been explained in details in section 2.4.2. The time dependent acoustic pressure of CSNP has been depicted in figure 3.5. In this graph, negative pressure is observed with a time shift of 500 ns, which is associated with the compression of the composite. The time dependent response of the model is marginally different from that of previous chapter as the transient behavior of the composite was not included in the solver in chapter 2.

The output pressure peaks at  $3\mu\text{s}$ , which is the time, required the sound wave to reach the hydrophone at 4.2 mm away from the composite. Given the speed of sound in water  $C_s$  (1420m/s), and distance of the hydrophone from the substrate, peak time can be calculated using

$$t_p = \frac{\text{distance between the hydrophone and substrate}}{C_s}$$

Figure 3.6 shows the acoustic pressure of CNF and CSNP transducers. As it is depicted, CSNP can generate stronger acoustic wave thanks to its higher light absorption. In addition, due to its fast-thermal expansion it is able to generate high frequency waves which is beneficial in biomedical imaging[15].

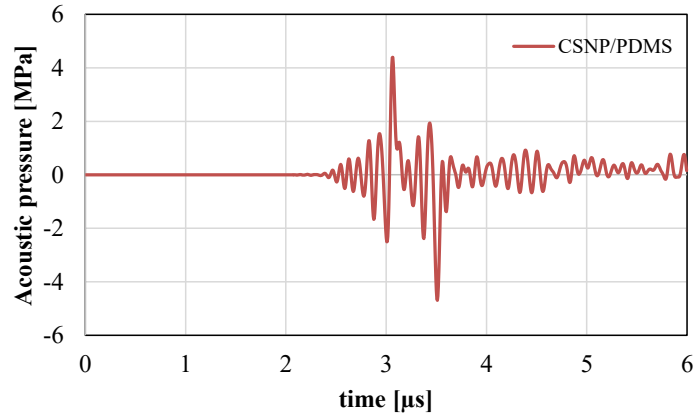


Figure 3.5 Output acoustic pressure generated by CSNP/PDMS composite at 4.2mm

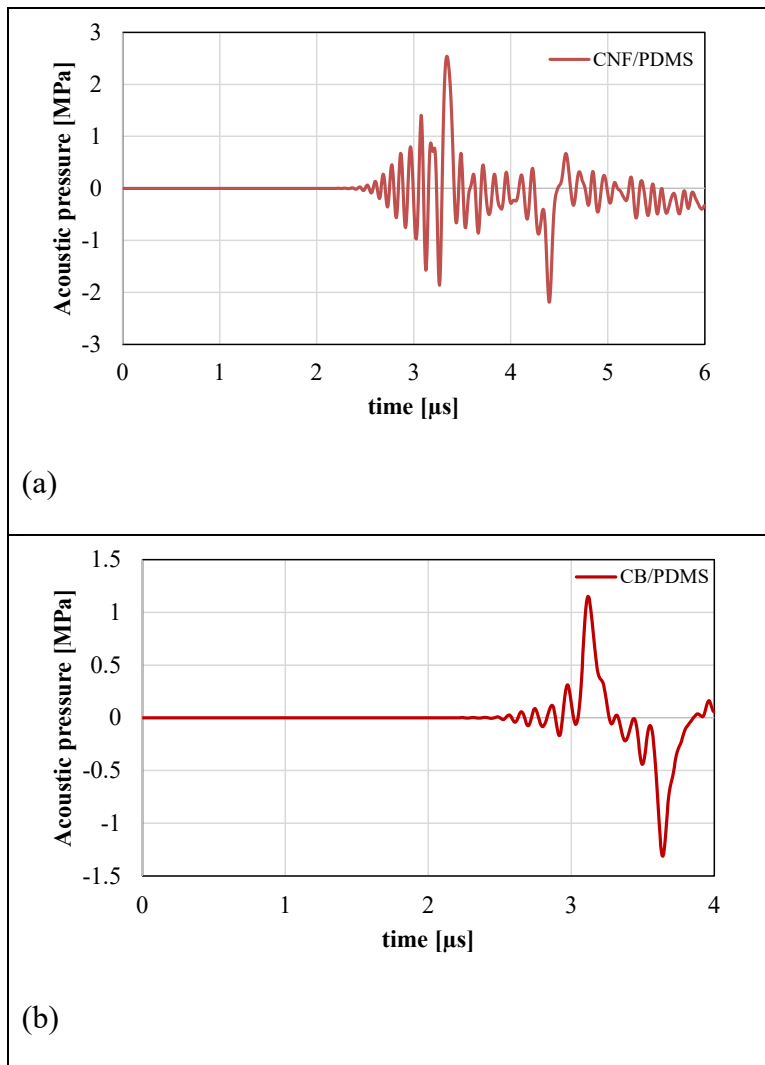


Figure 3.6 Output pressure of a) CNF/PDMS and b) CB/PDMS transducer at 4.2mm

### 3.2.6 Comparison of the numerical result with experimental study

With the description of three numerical models in the 2D-Axissymmetric environment in the previous sections, the result of those are compared with experimental study done by Huang W. and Chang W. in figure 3.7. [9][28].

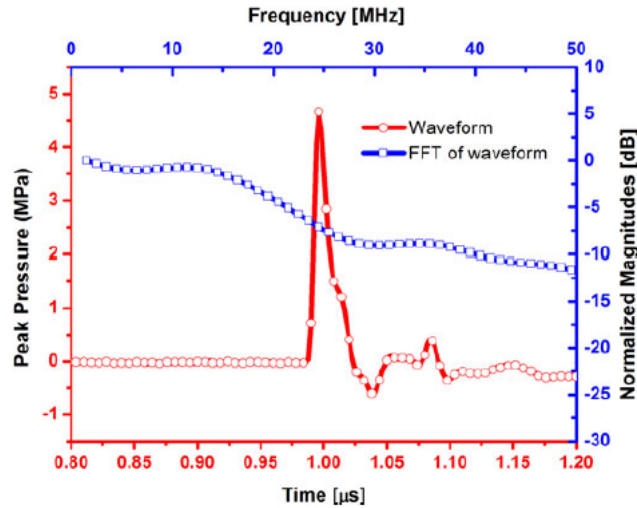


Figure 3.7 LGU of CSNP/PDMS transducer measured experimentally by Huang W. et.al[28]

As it can be observed in figure 3.8, a difference of 12%, 7% and 15% exists between maximum positive acoustic pressure of numerical and experimental study of CSNP/PDMS, CNF/PDMS and CB/PDMS respectively. Hence, our numerical model is validated.

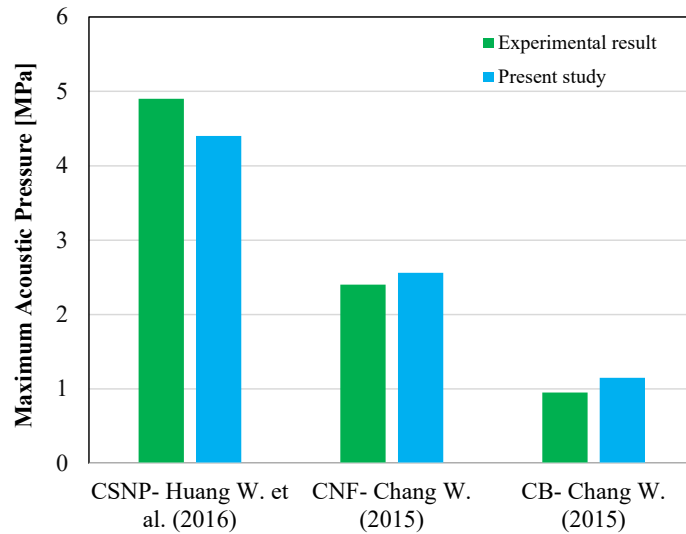


Figure 3.8 Pressure from the model compared with the experiments of Huang et. al.

The difference between experimental and numerical study is attributed to the following factors:

- The absorption coefficient of CB and CNF, which dominates the heat generation in the composite domain, was evaluated indirectly using equation (3-1) in which the effect of reflection is neglected.
- The spatial profile of the laser pulse was assumed to be a random Gaussian function which was not mentioned in the experimental studies.
- For simplicity, the effect of absorptive materials (CSNP, CNF and CB) in mechanical properties of PDMS was neglected.
- The possible off-axis position of hydrophone in experiment was not considered in the numerical model.
- The effect of backing material which contributes to the negative pressure, was not considered in the numerical model
- The line-average method, which was taken to evaluate the acoustic pressure, is the approximation of the pressure that is being measured by the hydrophone in experiment.
- The mesh size in water domain was properly configured only along the axis of the laser beam.

In order to reduce the error induced by the line average approximation and the error cause by the mesh size, a more accurate approach will be suggested in the next section.

### **3.3 Evaluation of output acoustic pressure of CSNP on a curved surface**

As it was discussed in previous section, one of the reasons that causes an error in the numerical model is the method by which the acoustic pressure is calculated. While in section 3.2.5 acoustic pressure was averaged along a line, the active surface of the hydrophone is not planar as it is shown in figure 3.9. In order to account for the geometry of the hydrophone, a semi sphere with a radius of a hydrophone is built in the model geometry. In addition to the change in the geometry of the monitoring surface, the mesh size has been reduced in the section where stronger acoustic pressure is predicted. For this purpose, a  $1\text{mm} \times 5\text{mm}$  rectangle is added to the geometry. This is particularly beneficial in reducing the computation time. The mesh size is chosen to be  $25\mu\text{m}$  in the newly added domain to resolve the acoustic wave. Figure 3.10 illustrates the modified geometry and mesh distribution, and the generated sound wave can be observed in figure 3.11.



Figure 3.9: Figure 3.9 HGL-0200, ONDA Crop.

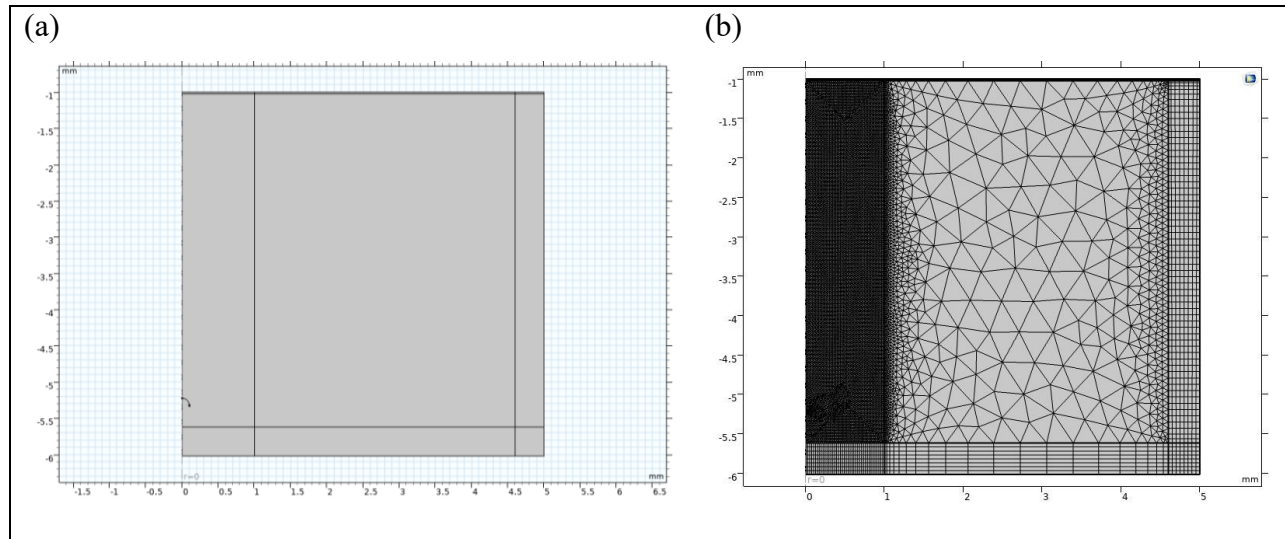


Figure 3.10: Figure 3.10 a) modified geometry including a semi-sphere monitoring surface b) a new mesh distribution adapted to resolve the acoustic wave in critical section

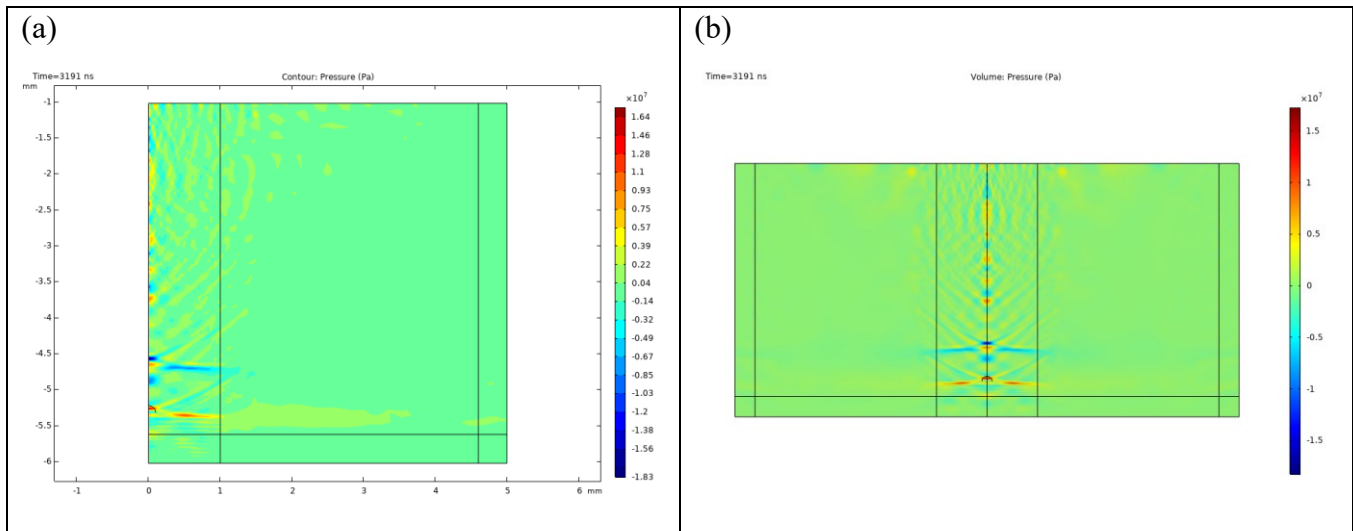


Figure 3.11: Figure 3.11 positive and negative pressure wave generated in a) 2-D axisymmetric environment b) 2D environment along the laser beam in the water domain at  $t=3191$  ns

Following the time dependent study, the output acoustic pressure versus time is plotted in figure 3.12. As it can be observed, using the properly configured mesh and geometry, yields a closer response to the experimental study. Maximum positive pressure in the case of CSNP/PDMS is about 5 MPa which compares well with the literature at which the pressure was measured to be 4.9MPa[28].

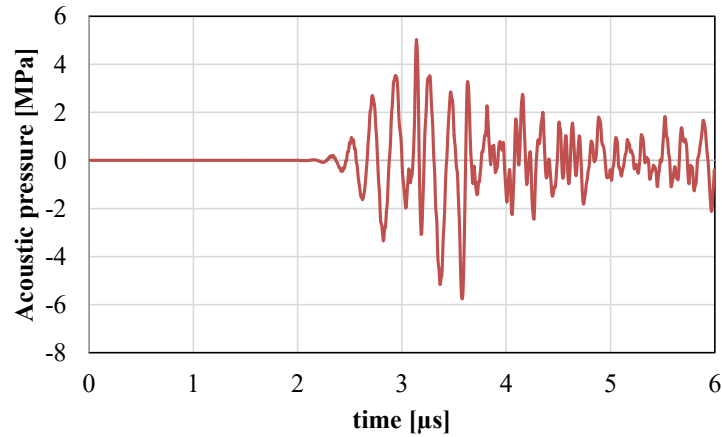


Figure 3.12: Figure 3.12 Output acoustic pressure of CSNP/PDMS composite evaluated on a semi sphere

### 3.4 Mesh refinement

To gain confidence in the accuracy of our model different mesh size was adapted and the result was compared. The maximum mesh size in the water domain is related to the minimum wavelength of the acoustic wave by following equation:

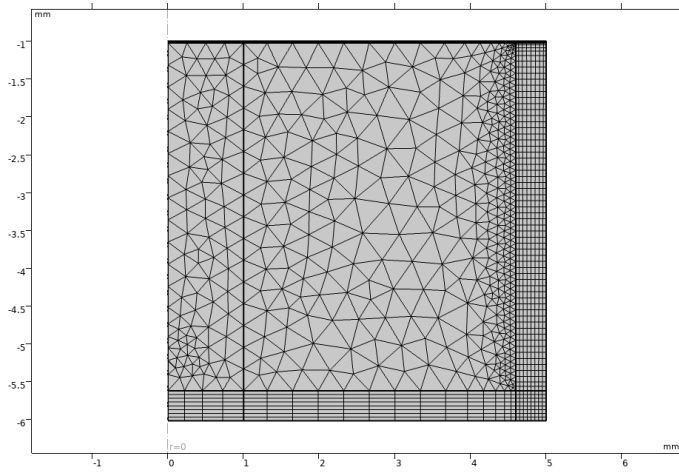
$$h_{max} = \frac{\lambda_{min}}{N} = \frac{c}{N \times 10 [MHz]} \quad (3-2)$$

As it was explained in chapter 2, N denotes the number of elements in a wavelength. As a result, by changing parameter “N” different mesh sizes can be generated. To reduce computation time, only the 1mm × 5mm rectangular domain is affected by mesh refinement. Mesh size variation with respect to N is shown in table 3.2, and the distribution shown in Figure 3.13.

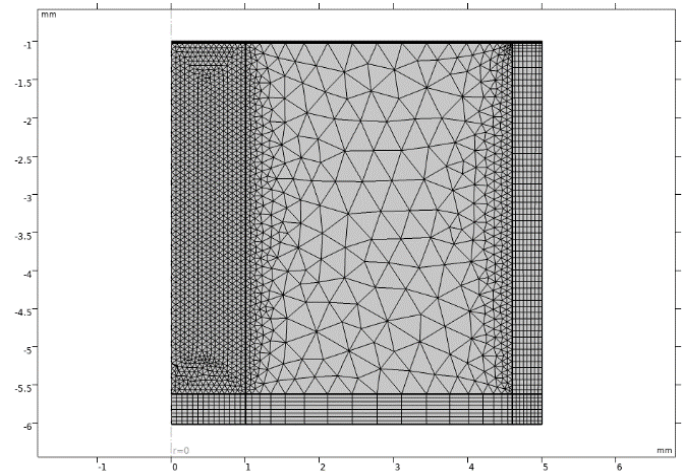
N	0.5	2	4	6
Max mesh size [μm]	296	74	37	25

Table 3.2 Different values of “N” and its corresponding mesh size

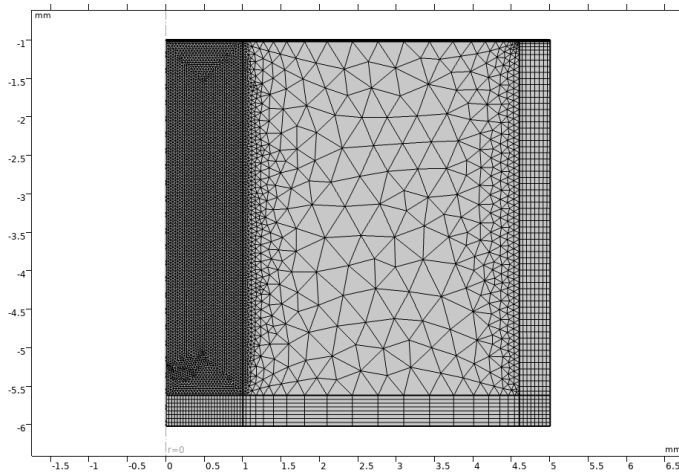
N=0.5



N=2



N=4



N=6

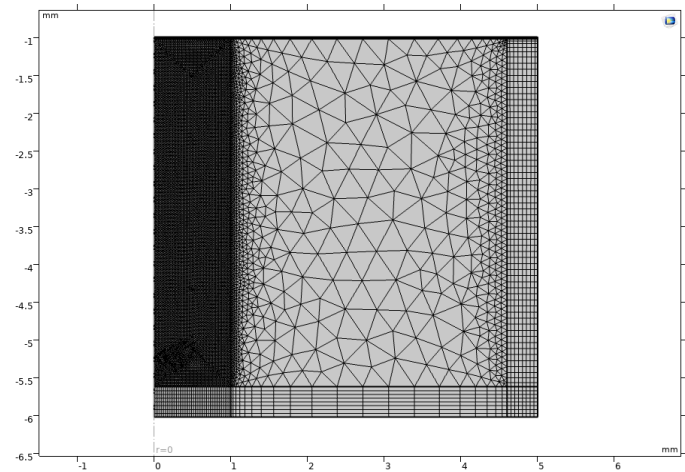


*Figure 3.13 Mesh distribution of 2-D axisymmetric model of CSNP with variation of “N”*

After re-evaluation of the result for each mesh size, maximum acoustic pressure averaged along the monitoring semi sphere was plotted versus parameter “N”. The result can be seen in figure 3.14.

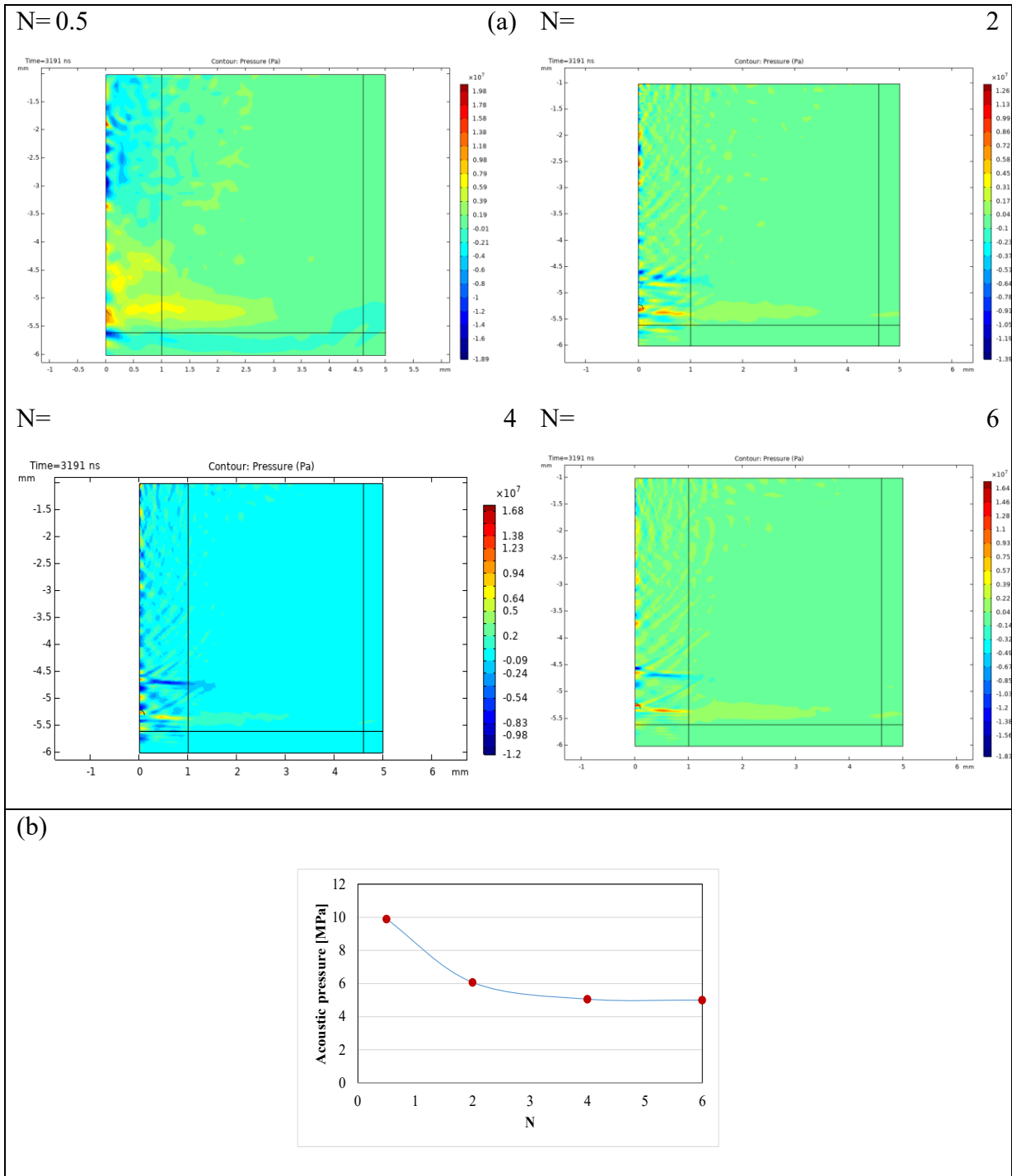


Figure 3.14: Figure 3.14 a) Generated acoustic pressure in 2-D axisymmetric model for variation of “N” at  $t=3191$ ns. b) Maximum acoustic pressure with respect to “N”

By comparing the result obtained in figure 3.14, it is concluded that the model is producing a mathematically accurate solution when “N” is set as 4 or any larger value. At “N” equal to 4 the maximum mesh size in  $1\text{mm} \times 5\text{mm}$  domain is equal to  $37\mu\text{m}$ .

With the new refinement in geometry of the hydrophone, and mesh refinement, the results from the simulation is shown in comparison with experiments of Huang et. al. in figure 3.15. The pressure generated from the model is 5 MPa with the refined model, which compares well with 4.8MPa from experiments with only a variation of 4%. This reduces from the variation of 12.5% in case of line average method, discussed in section 3.2, figure 3.8.

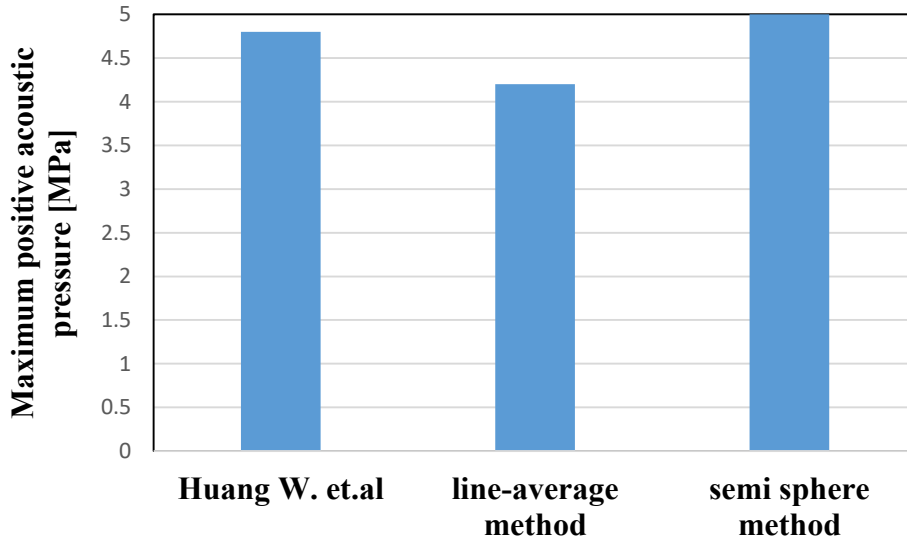


Figure 3.15 Pressure from the model compared with the experiments of Huang et. al.

### 3.5 Effect of composite thickness on acoustic pressure

In this section, effect of composite thickness on the output pressure has been investigated. For this purpose, 6 different thicknesses have been employed in the numerical model of CSNP/PDMS transducer in 2-D axisymmetric environment. In all cases, light absorption coefficient remains constant. As it can be seen in figure 3.16, maximum acoustic pressure increases with the increase in thickness until it reaches its peak pressure at  $2\mu\text{m}$ . Then the value of output pressure drops with further increase in thickness. This behavior can be explained by the optical properties of the absorber. As it was discussed in section 2.3.2, optical absorption of CSNP was measured to be  $1\text{ [}1/\mu\text{m]}$  which leads to the penetration depth of  $1\mu\text{m}$ . That means that the minimum thickness of the composite should be equal to  $1\mu\text{m}$  in order for the light to be fully absorbed. On the other hand, by keeping the absorption coefficient constant, thicker absorber causes more attenuation. As a result, acoustic pressure drops as the thickness exceed an optimum value. The experimental result carried out on gold nanoparticles (Au NPs)/PDMS transducer shows a similar trend[30].

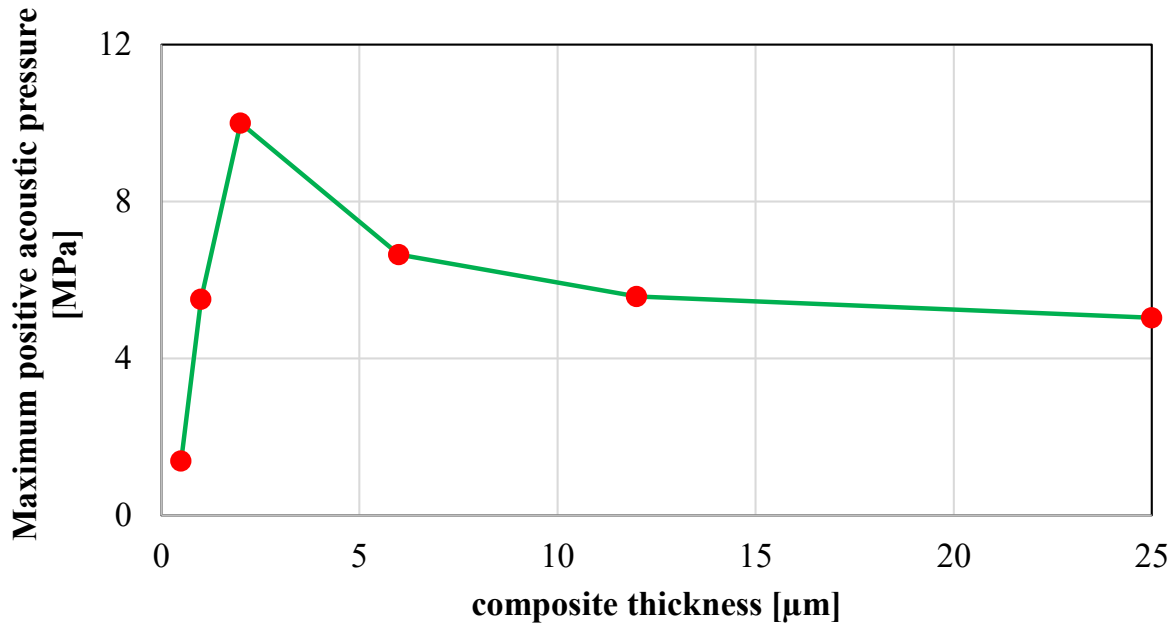


Figure 3.16 The amplitude of acoustic pressure with various composite thickness and identical absorption coefficient

### 3.6 Impact of laser fluence on the acoustic pressure

According to equation 1-4, acoustic pressure is proportional to the laser fluence. The numerical study has been carried out to investigate the relationship between laser fluence and output pressure and has been compared to the experimental study[9]. The laser energy density ramped from  $3.75[\text{mJ}/\text{cm}^2]$  to  $28.03 [\text{mJ}/\text{cm}^2]$  in the case of CSNP/PDMS composite. The result is illustrated in figure 3.17. As it was expected, maximum acoustic pressure increases linearly with the increase in the laser fluence.

It should be noted that, in the experimental study, the acoustic pressure has been measured at the position of 46mm from the substrate to avoid potential damage to the hydrophone. Whereas the numerical simulation has executed the result at 4.2mm distance from the composite since 46mm distance requires larger model geometry and will increase computation time. Consequently, the acoustic pressure magnitude does not match the experimental value. However, same trend can be observed in both studies. It can be noted that pressure increases with lower rate as laser fluence is

increased in the experimental study. This has been reported to be caused by partial detachment of the composite from glass slide which is not the case in simulation result.

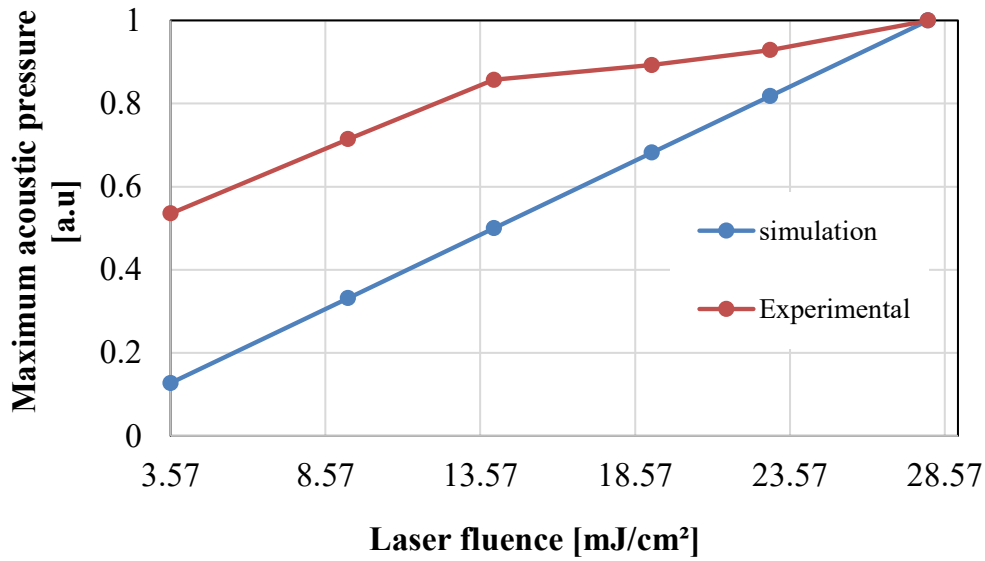


Figure 3.17 Maximum acoustic pressure versus different laser fluence

Increasing the energy of the incident laser beam seems to be an easy approach to increase photoacoustic amplitudes. However, this approach is limited by potential material damages induced by laser ablation. Thus, such approach is effective only when light-absorbing materials are sufficiently robust.

### 3.7 Relationship between laser pulse width and acoustic pressure

According to expression 1-4, acoustic pressure is related to laser pulse duration. To validate the previous analytical results, I numerically evaluated the acoustic pressure as a function of pulse duration and the simulation results is depicted in figure 3.17. The pulse duration used in the simulation was varied from 0.5 ns to 50 ns. The results show that the amplitude of acoustic signals increases with a decreasing pulse duration. The acoustic pressure declines more significantly in the beginning. This is due to the existence of stress confinement when laser pulse is short compared with the time required for the pressure wave to leave the heated region.

For efficient laser generation of ultrasound, the laser pulse duration should be short compared to the absorption coefficient of  $1 \left[ \frac{1}{\mu\text{m}} \right]$  for CSNP and laser pulse width of 6ns, the stress confinement

time ( $\tau_s = \frac{1}{c\beta}$ ) would be 1 ns. Hence, a pulse duration less than 1 ns, generates the most effective acoustic pressure.

Increasing the pulse width, would mean that the pressure wave will start to leave the optical absorption region while pressure is still being added by the laser pulse. In other words, the pressure spreads out rather than builds up and therefore the maximum amplitude decreases as the laser pulse duration increases. This trend agrees well with the experimental study of CB/PDMS and CNT/PDMS conducted by Fei G. et.al[30].

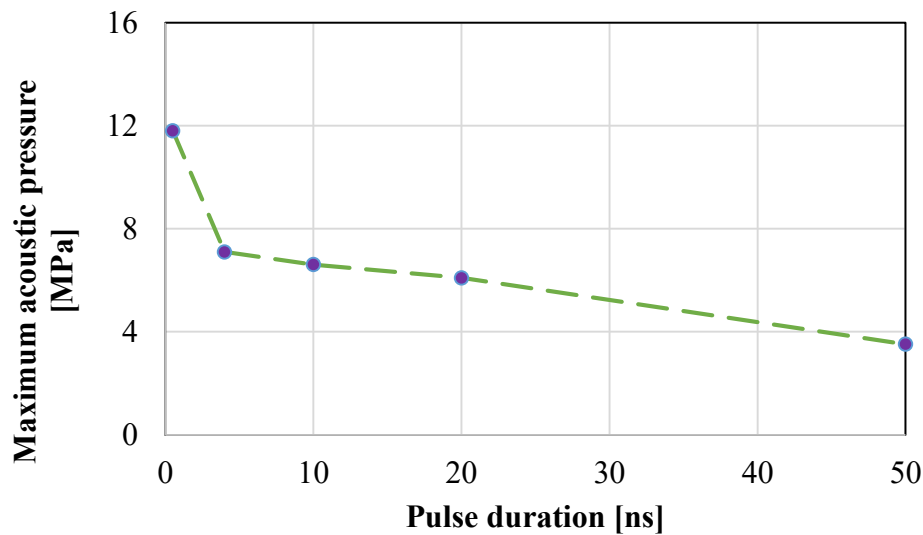


Figure 3.18 The peak pressure amplitude for CSNP/PDMS versus laser pulse width

### 3.8 Summary

In this chapter, a different approach was taken to simulate the laser generated photoacoustic ultrasound in which transient behavior of optical absorber was considered. The numerical model in 2\_D axisymmetric environment has been compared with the experimental studies for CSNP, CNF and CB embedded PDMS composite and very good agreement was reported.

To reduce the error induced by the line-average method of pressure evaluation, a new model was built to better approximate the surface of the active element of hydrophone. In this model a curved monitoring surface was created in the geometry on which the incident acoustic field was averaged. In addition, a well-configured mesh distribution was constructed in the critical region. The reported acoustic pressure provided the more accurate prediction of experiment. To ensure that the

presented model is providing true results, mesh refinement was carried out to find the optimum element size.

At last, the effect of composite thickness, laser energy and pulse duration on the output pressure was investigated. The numerical solution provides valuable data on how to improve the performance of laser generated ultrasound by tailoring the effective parameters. In general, this new analytical model provides new guidelines in the design of efficient ultrasound transducer, hence opening up promising applications to medical field. In the next chapter, the extension of my study on high repetition rate lasers will be elaborated.

## **CHAPTER 4. Feasibility study of LGU using high repetition rate lasers**

### **4.1 Introduction**

In this chapter, the feasibility of using high repetition rate laser as an excitation source for photoacoustic generation will be investigated. This is mainly because the low repetition rate lasers would bear a considerable high cost compared to high repetition ones. Since no study has been done on the damage threshold of carbon/PDMS transmitter under radiation of high repetition rate lasers (HRRL), I first examined the condition in which HRRL can be used without causing damage to the composite. For this purpose, a CSNP/PDMS planar transducer was fabricated and damage threshold at different repetition rates was evaluated. Lastly, possible repetition rates were chosen according to the desirable acoustic pressure.

### **4.2 Laser**

Available pulsed laser can be categorized into nanosecond, femtosecond and picosecond lasers. Most femtosecond and picosecond lasers, commonly known as ultrafast lasers, operates in infrared region. As it was mentioned in chapter one, the absorption coefficient drops with the increase in wavelength. Therefore, nanosecond lasers in visible range are more favorable for photoacoustic ultrasound generation.

Conventionally, a laser ultrasonic technique uses a single pulse laser excitation and generates only broadband ultrasonic signals without frequency control capacity. The narrowband ultrasonic waves can be generated using repetitive pulse lasers with a high repetition rate[73]. Figure 4.1 shows a representative ultrasonic signal generated by a single pulse and repetitive pulse laser excitation.

It should be noted that time interval between two adjacent laser pulses controls the central frequency of the generated narrowband ultrasonic waves[73]. In this study, Matrix 532-14-40, a solid-state Q-switched pulsed laser with a wavelength of 532nm and repetition rate of up to 200KHz was considered. As it will be explained in the next part, energy per pulse generated by this laser is much smaller than of that in low repetition rate lasers. As a result, beam diameter needs to be reduced to have an adequate laser fluence. To ensure that the PDMS/carbon will not damage

during the process, it is necessary to evaluate the damage threshold in case of high repetition rate laser. First fabrication method of CSNP/PDMS transducer will be explained.

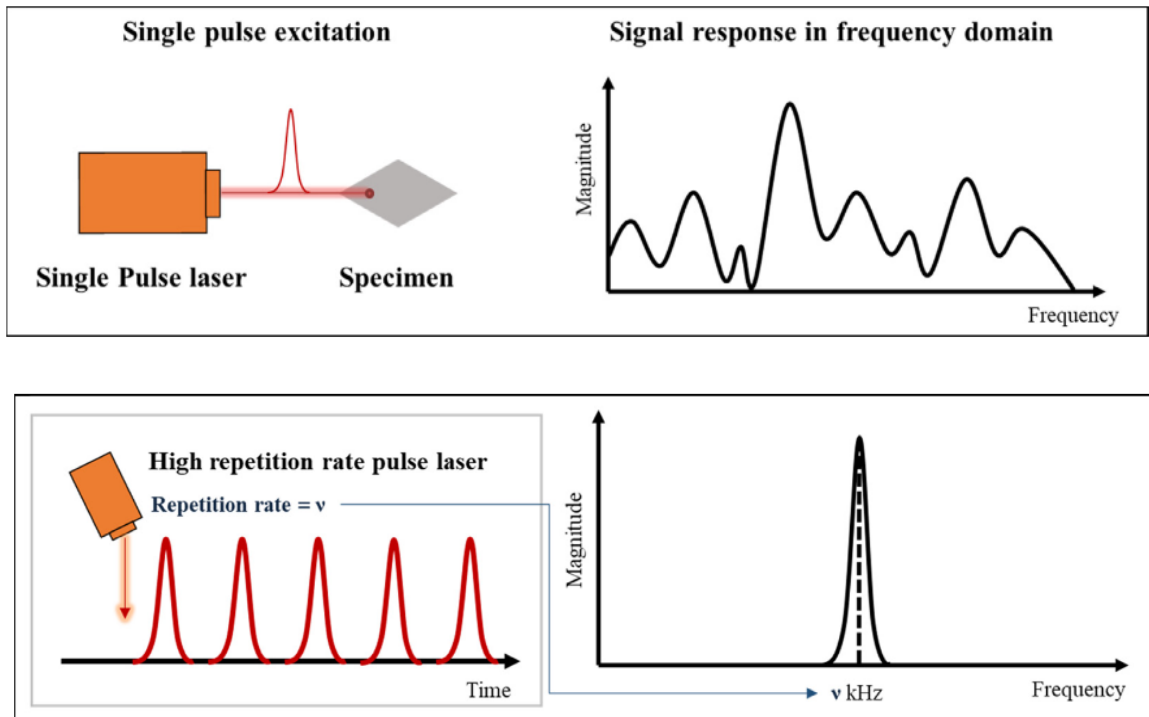
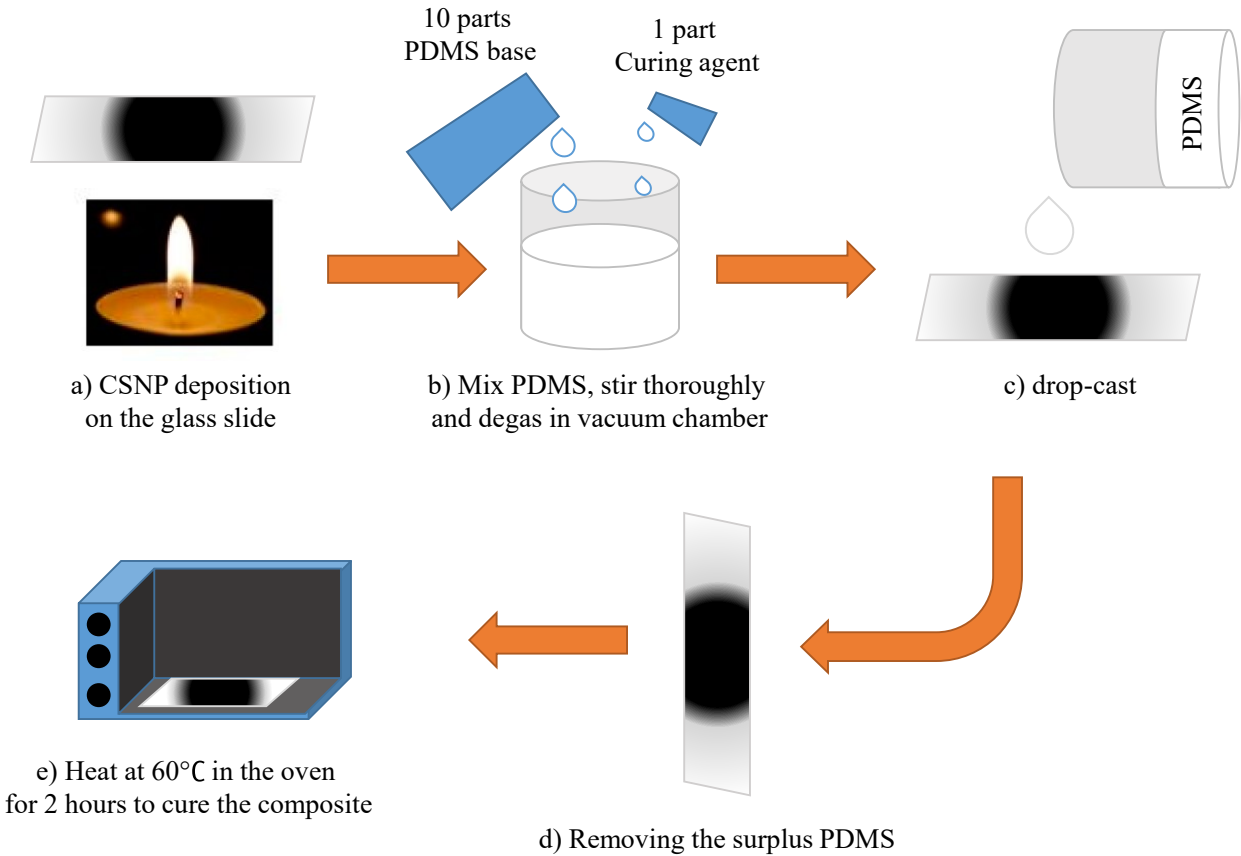


Figure 4.1 Relationship of Ultrasound bandwidth to laser repetition rate[73]

### 4.3 Fabrication of CSNP/PDMS transducer

As it was discussed in chapter 1, different fabrication techniques exist depending on the deposited material and applications in which transducers will be used. In our experience, bottom-up method was adapted to coat CSNP and PDMS on a glass substrate. The schematic diagram for fabrication is shown in Figure 4.2. In this method, A flame synthesis process was employed to obtain CSNP at room temperature using a paraffin wax candle. A glass slide was continuously moved for several seconds at about 2 cm above the wick, resulting in a coated area of approximately 25 mm by 30 mm. Meanwhile, a PDMS thermal expansion layer was fabricated. The PDMS was prepared with a base and curing agent (Sylgard184) with a ratio of 10:1, and then degassed for 30 min in a vacuum chamber (Nalgene Desiccator, 150mm, Thermo Scientific). Next, uncured PDMS was coated directly on the CSNP-coated glass slide by drop-casting method. To remove the surplus PDMS, the coated glass was rotated by 90° and placed for 30 minutes. Tissue paper was used to

wipe out the surplus PDMS from the downside of the composite. Finally, the composite was placed in the oven (Fisher Scientific Isotemp Oven) for 2 hours at 60°C to be cured. The fabricated sample is shown in figure 4.3.



*Figure 4.2 Fabrication process of CSNP/PDMS nanocomposite*



*Figure 4.3 Fabricated planar photoacoustic transmitter coated by CSNP/PDMS layer*

#### 4.4 Evaluation of the properties of fabricated CSNP/PDMS transducer

In this section, absorption coefficient of the fabricated transducer shall be evaluated using thickness and optical absorbance. Optical power meter was utilized to measure reflection and transmission of the light beam as it passes through the sample. The absorption properties were measured using the power meter (Coherent LabMax-TOP) at normal incidence at the sample on seven different points and the values were averaged. Total transmission,  $T$ , and reflection,  $R$ , of each point were measured, and absorption was obtained as  $1-T-R$ . Table 4.1 shows these optical properties for each point on the sample.

#	Reflection (R) [%]	Transmission (T) [%]	Absorption [%]	Absorbance = $-\log T$ [au]
1	5.18	2.96	91.85	1.53
2	3.84	1.73	94.42	1.76
3	3.98	0.77	95.24	2.11
4	3.39	1.07	95.53	1.97
5	3.37	1.26	95.36	1.89
6	3.10	1.63	95.26	1.79
7	3.68	1.66	94.65	1.78
Average = 3.78		Average = 1.58	Average = 94.62	Average = 1.83

*Table 4.1 optical properties of CSNP/PDMS transmitter measured by power meter*

To characterize the thickness of the CSNP-PDMS composite, scanning electron microscopy (Hitachi S-3400N) has been used. In order to measure the thickness of coated part of the glass, it was carefully cut from its center and fixed in the holder as it is shown in figure 4.4. Based on the observation of sample cross section, as depicted in figure 4.5, average thickness of CSNP/PDMS layer was measured to be  $17\mu\text{m}$ .

Based on the measured thickness and optical properties, wavelength-dependent absorption coefficient can be calculated by the following relationship:

$$\alpha(\lambda) = \left(\frac{1}{l}\right) \ln \left( \frac{(1-R)^2}{2T} + \sqrt{\frac{(1-R)^4}{4T^2} + R^2} \right) \quad (4-1)$$

where “ $\lambda$ ” is the wavelength and “ $l$ ” denotes absorber thickness. By substituting the values from the table 4.1 in equation 4-1, absorption coefficient of  $0.25 \left[ \frac{1}{\mu\text{m}} \right]$  is obtained.

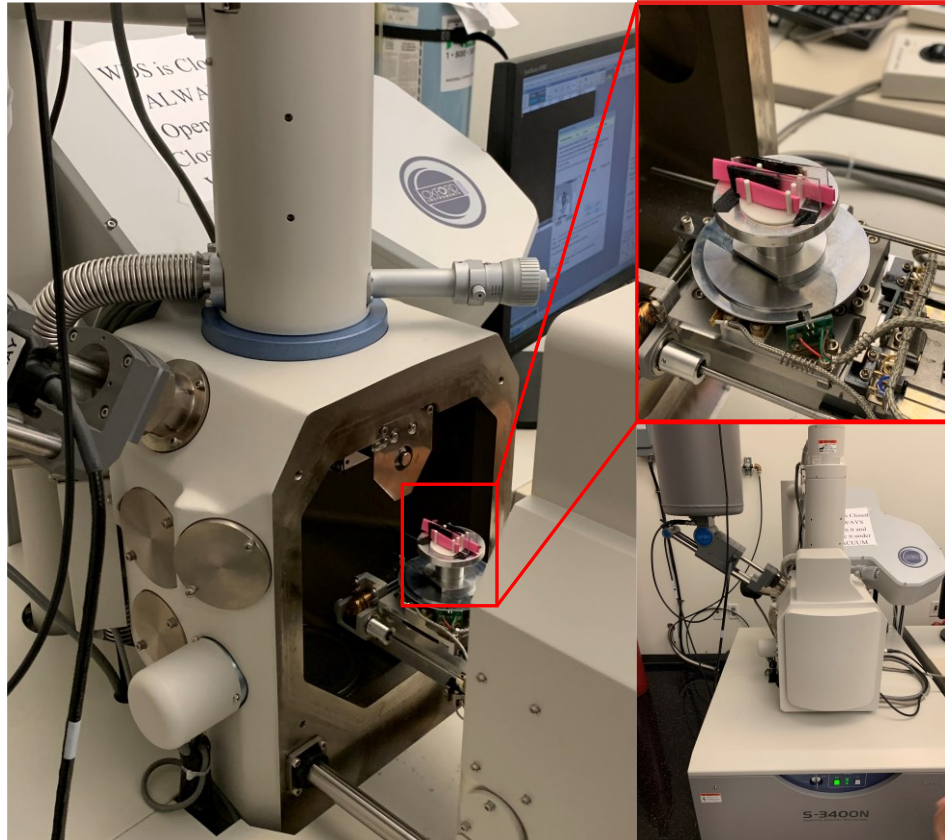


Figure 4.4 Scanning electron microscopy (SEM) of fabricated CSNP/PDMS composite

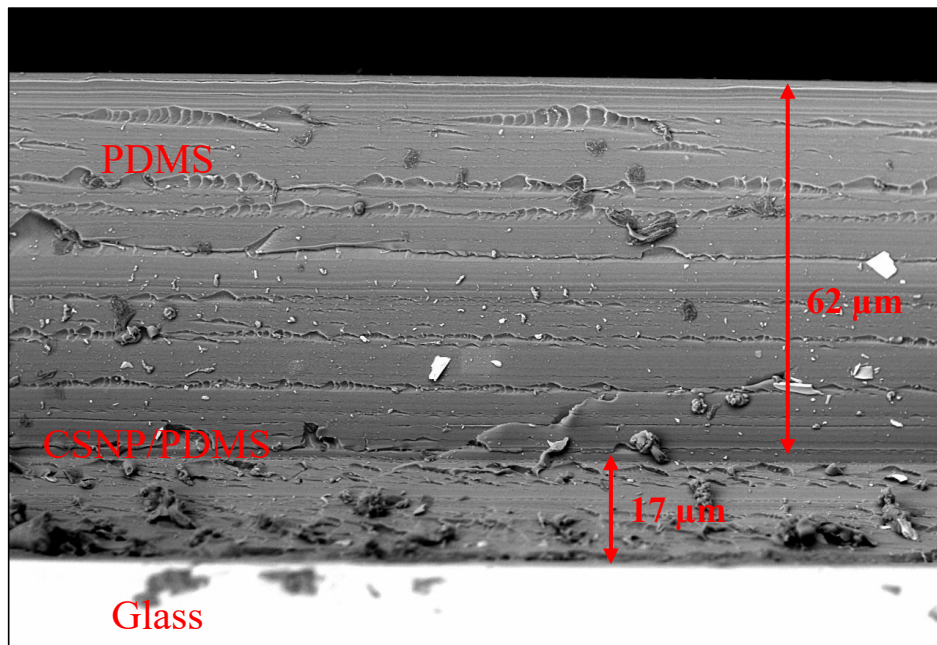
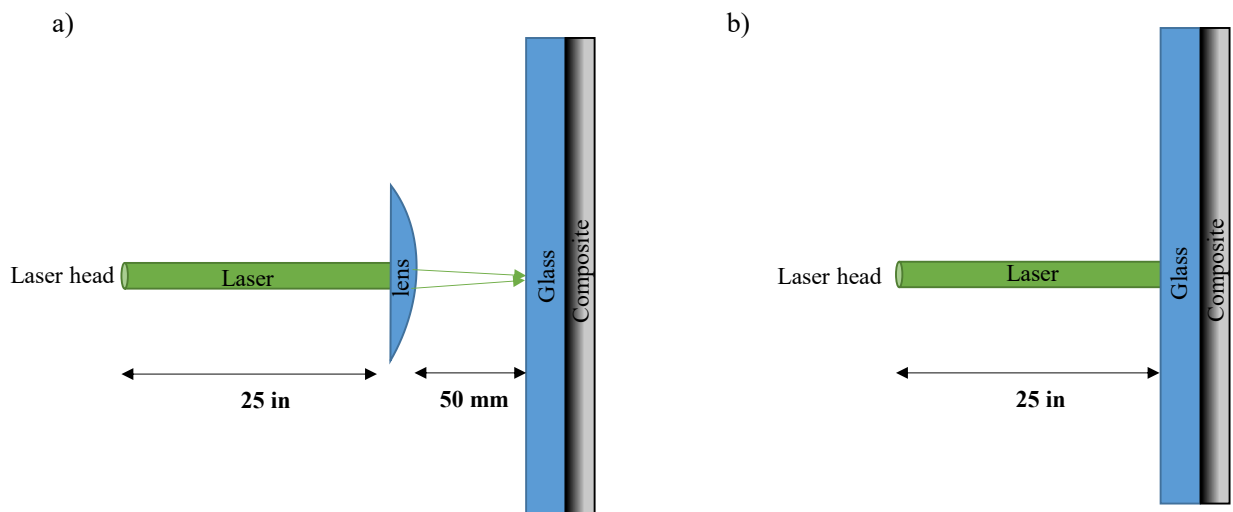


Figure 4.5 Scanning electron micrographs of the candle soot/PDMS nanocomposites

#### 4.5 Damaged threshold of CSNP/PDMS transducer at various repetition rates

The maximum laser fluence is limited by the damage threshold of photoacoustic composite, which depends on absorber material, thickness and laser wavelength. An experimental study carried by Srivalleesha Mallidi et.al recorded the maximum fluence of  $300 \text{ mJ/cm}^2$  for  $150\mu\text{m}$  thick PDMS/carbon black transducer[72]. However, the damage threshold of each fabricated sample needs to be measured and previous studied cannot be used as thickness changes per sample.

To determine the damage threshold of our transducer, fabricated CSNP/PDMS coated glass substrate was impacted by the pulsed laser. In order to increase the output power, repetition rate was varied from 2600Hz to 40000Hz. Two different setups were used to conduct the experiment: in the first one, a plano-convex lens was placed before the sample to focus the laser beam since ablation does not occur in low repetition rate region and in the second, laser beam was shined directly on the sample. The schematic of these two setups can be seen in figure 4.6. As it is illustrated Silica plano-convex lens (SPX061AR, Newport) with diameter of 25.4 mm and focal length of 50 mm is posited 25 in away from the laser head.



*Figure 4.6 Schematic of the experiment done to measure damage threshold of CSNP/PDMS composite. (a) with a plano-convex lens (b) without a lens*

The damage threshold can be computed as follows:

- 1- *For the case where a plano-convex lens was used:* In this case the laser was tuned in 2600Hz and 10000Hz. It should be noted that 2600Hz was the smallest repetition rate in which laser is

able to generate power. Also, the output power is limited by repetition rate. Therefore, in order to increase the power beyond a certain value, repetition rate must be increased.

At 2600Hz, output power was measured to be 15mW. No ablation was observed at this power. Then repetition rate was increased to 10000Hz. The laser power which is controlled by “set current” in continuous pulse mood, was increased until ablation occurred at 250mW. To calculate damaged threshold, spot size and energy per pulse need to be evaluated. Below, energy per pulse is obtained using average power and repetition rate:

$$\text{Energy per pulse} = \frac{P_{ave}}{RR} = \frac{250 \times 10^{-3}}{10 \times 10^3} = 25 \times 10^{-6} J = 0.025 mJ \quad (4-2)$$

According to the laser datasheet, the beam waist location is 230mm inside the laser head. Due to the natural divergence of a laser beam, the beam diameter changes as a function of the distance from the laser head. Figure 4.7, illustrates the dependence of beam diameter on axial distance.

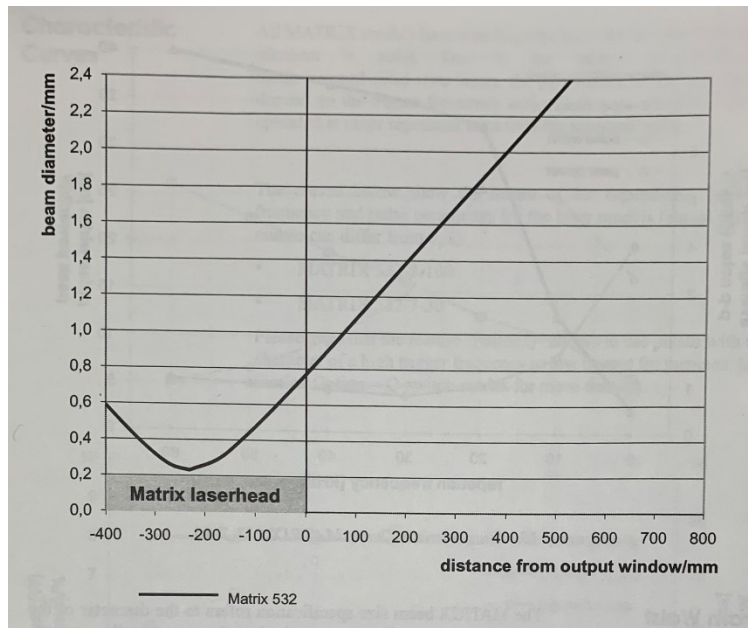


Figure 4.7 Typical beam propagation for MATRIX 532 Models[74]

As it is shown in figure 4.7, beam diameter at laser head is approximately 0.76 mm. Given a 4.2mrad divergence of laser beam, beam diameter of 6.1 mm is obtained at the distance of 25in from the laser head[75]. Laser spot size and fluence on the substrate can be calculated as follows:

$$\text{Spot size} = \frac{\text{focal length} \times \text{wavelength}}{\text{aperture}} = \frac{50 \times 10^{-3} \times 532 \times 10^{-9}}{6.1 \times 10^{-3}} = 4.36 \mu m \quad (4-3)$$

$$\text{Laser fluence} = \frac{\text{Energy per pulse}}{\text{area}} = \frac{0.025}{1.49 \times 10^{-7}} = 167000 \frac{\text{mJ}}{\text{cm}^2} \quad (4-4)$$

2- *Direct laser incident on the composite:* In this case damaged threshold happened at 0.7W, 1W, 1W for repetition rate of 20000Hz, 30000Hz and 40000Hz respectively. Using equation 4-1, energy per pulse was calculated to be 0.035mJ, 0.034mJ and 0.025mJ. It should be noted that spot size is 6.1mm. The result is shown in table 4.2.

RR[HZ]	Focused incident beam		Direct incident beam		
	2600	10000	20000	30000	40000
Power [W]	0.015	0.25	0.7	1	1
Spot size [ $\mu\text{m}$ ]	4.36	4.36	6100	6100	6100
Energy per pulse [mJ]	0.006	0.025	0.035	0.034	0.025
Damage threshold [ $\text{mJ}/\text{cm}^2$ ]		167000	0.12	0.11	0.08

*Table 4.2 Damage threshold of CSNP/PDMS composite in deferent repetition rates*

As it can be observed, damage threshold rises as repetition rate ramps up. This is due to the accumulative laser energy being deposited in higher frequencies. In the next section the feasibility of using MATRIX 532 as an excitation source for photoacoustic generation will be discussed.

#### 4.6 Using MATRIX 532 for photoacoustic generation

According to equation 1-4, laser fluence of around  $11 \text{ mJ}/\text{cm}^2$  is required to generate an output acoustic pressure of 3.6 MPa. As it was discussed earlier, laser energy is constrained by repetition rate. As a result, beam diameter can be used as a control parameter in order to generate the required laser fluence. Table 4.3 shows what beam diameter can be chosen to produce laser fluence of  $11 \text{ mJ}/\text{cm}^2$ .

Repetition rate [Hz]	2600	10000	20000	30000	40000
Laser power [W]	0.015	0.25	0.7	1	1
Beam diameter [mm]	0.26	0.53	0.63	0.62	0.54
Fluence [ $\text{mJ}/\text{cm}^2$ ]	11	11	11	11	11
Laser energy [mJ]	0.0057	0.025	0.035	0.034	0.025

*Table 4.3 Beam diameter required to produce laser fluence of  $11 \text{ mJ}/\text{cm}^2$*

As it can be observed, in cases where repetition rates of 20, 30 and 40 kHz were employed, beam diameter needs to be 0.63, 0.62 and 0.54mm respectively, which are smaller than 6.1mm by an order of magnitude. Consequently, laser fluence far exceed the damage threshold of CSNP/PDMS

composite. However, in cases where repetition rate is tuned to be 2600Hz and 10000Hz, the required diameter for laser fluence of  $11 \text{ mJ/cm}^2$  is 0.26 mm and 0.53mm respectively which are larger than  $4.36\mu\text{m}$  (.0046mm) which indicates the feasibility of photoacoustic ultrasound generation with high repetition rate lasers. Figure 4.8, summarizes the result obtained under different laser repetition rates. Green marker is used to show the repetition rates in which photoacoustic ultrasound can be generated without damaging the CSNP/PDMS transducer.

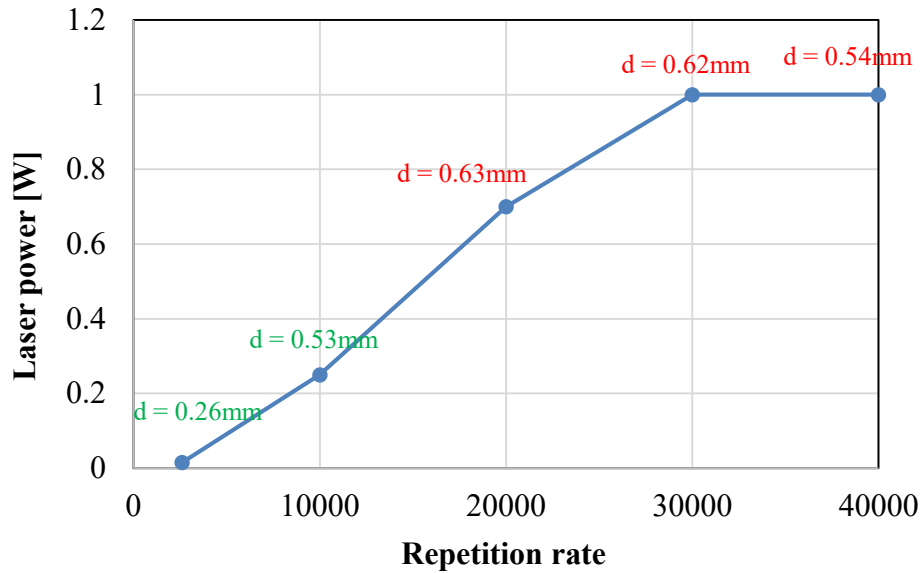


Figure 4.8 Required beam diameter to produce  $11 \text{ mJ/cm}^2$  fluence for different repetition rate

It can be concluded that repetition rates of 2600Hz and 10000Hz are able to generate enough laser fluence to create acoustic pressure and yet not creating large deposition of heat into the composite that triggers damage within the composite. It is worth noting that laser fluence can be controlled by varying beam diameter as long as it does not exceed the damage threshold.

Although acoustic pressure generation is feasible under the above-mentioned repetition rates, no pressure was measured using Muller-plate needle hydrophone in the case of 10000Hz repetition rate with beam diameter of 0.53 mm during our experiments. The experimental setup is illustrated in figure 4.9.

This indicates that there might be other factors influencing the pressure generation, which necessitates performing a numerical simulation.

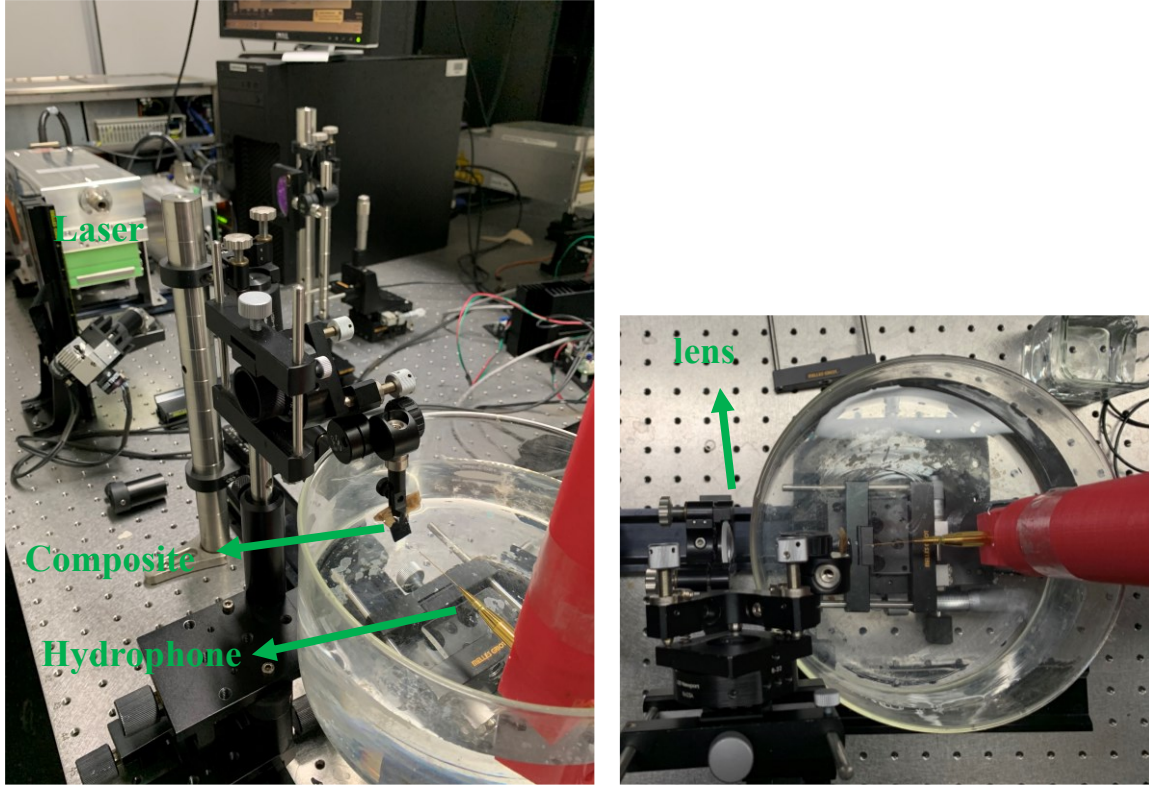


Figure 4.9 Experimental setup

#### 4.7 Numerical simulation with excitation source as Matrix 532-14-40

To verify our conclusion obtained in section 4.6, a 2D numerical model of CSNP/PDMS composite was created using laser parameters of Matrix 532-14-40. The simulation process is same as explained in chapter 2. However, simulation parameters have been adjusted to the Matrix laser and the fabricated CSNP/PDMS transducer as shown in table 4.4.

Laser fluence, $E_0$ [ $\text{mJ}/\text{cm}^2$ ]	11.3
Pulse width, $\tau$ [ns]	20
Standard deviation, $\sigma$ [ns]	12
Laser spot radius, $r$ [mm]	0.53
Absorption coefficient [ $1/\mu\text{m}$ ]	0.25
CSNP/PDMS thickness [ $\mu\text{m}$ ]	17/62
Water dimension [mm]	10×5

Table 4.4 Simulation parameters for excitation source as Matrix 532-14-40

The total number of meshes, 10300 elements including mapped and free triangular, is different from previous model in section 2.4.2 due to the different dimension of the transducer. Time-

dependent study was performed for a period of  $6\mu\text{s}$ . Mesh distribution and pressure propagation at  $3.4\mu\text{s}$  is shown in figure 4.10.

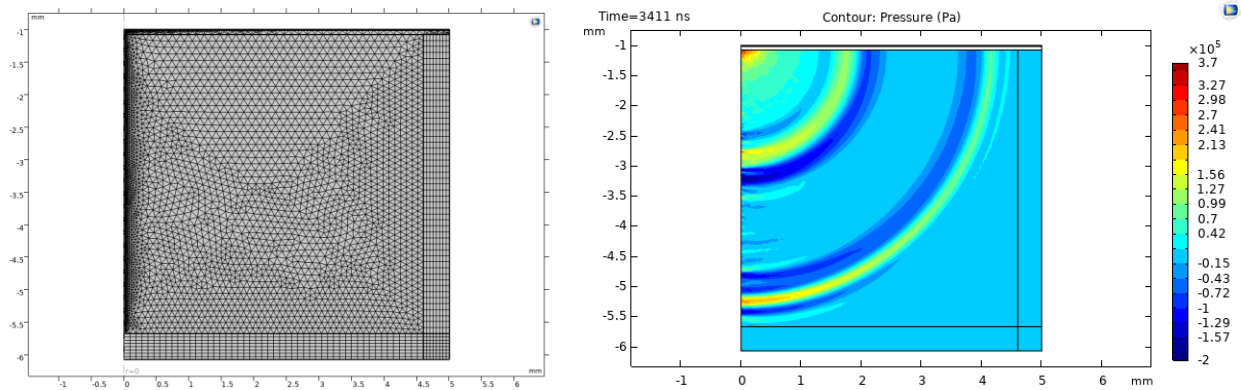


*Figure 4.10 Mesh distribution and pressure propagation of CSNP/PDMS transducer under excitation of Matrix 532-14-40*

Acoustic pressure was evaluated using the line average method (as in section 3-2-4) at 4.2mm away from the traducer. The result can be seen in figure 4.11. Maximum acoustic pressure is about one order of magnitude less than the expected number. Small beam diameter is surmised to contribute to this low acoustic pressure. In order to gain confidence that beam diameter is a dominant factor for this low pressure, the simulation has been repeated with the input parameters of table 4.5 as absorption coefficient and pulse width have been changed to  $1[1/\mu\text{m}]$  and  $6\text{ns}$  respectively.

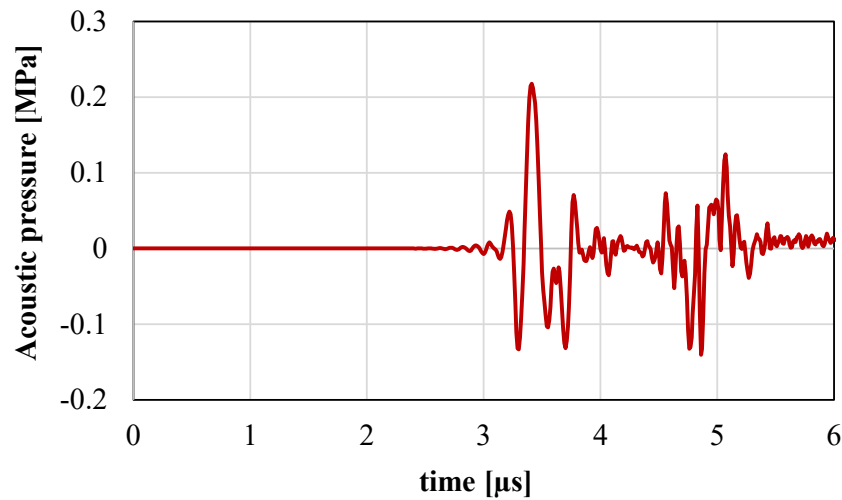


*Figure 4.11 Output acoustic pressure of CSNP/PDMS transducer under excitation of Matrix 532-14-40*

Laser fluence, $E_0$ [ $\text{mJ}/\text{cm}^2$ ]	11.3
Pulse width, $\tau$ [ns]	6
Standard deviation, $\sigma$ [ns]	3.6
Laser spot radius, $r$ [mm]	0.53
Absorption coefficient [ $1/\mu\text{m}$ ]	1
CSNP/PDMS thickness [ $\mu\text{m}$ ]	17/62

Table 4.5 Simulation parameter of CSNP/PDMS transducer fabricated by Wenbin Huang et.al [28] under excitation of Matrix 532-14-40

Acoustic pressure was computed at 4.2mm away from the substrate and the result is illustrated in figure 4.12. As it can be observed there is a slight difference between figure 4.11 and 4.12 which indicates that even larger absorption coefficient and smaller pulse widths do not contribute to the pressure amplitude in the case of small aperture size. In the next section, two 2D-numerical models will be simulated in COMSOL Multiphysics to investigate the effect of beam diameter.

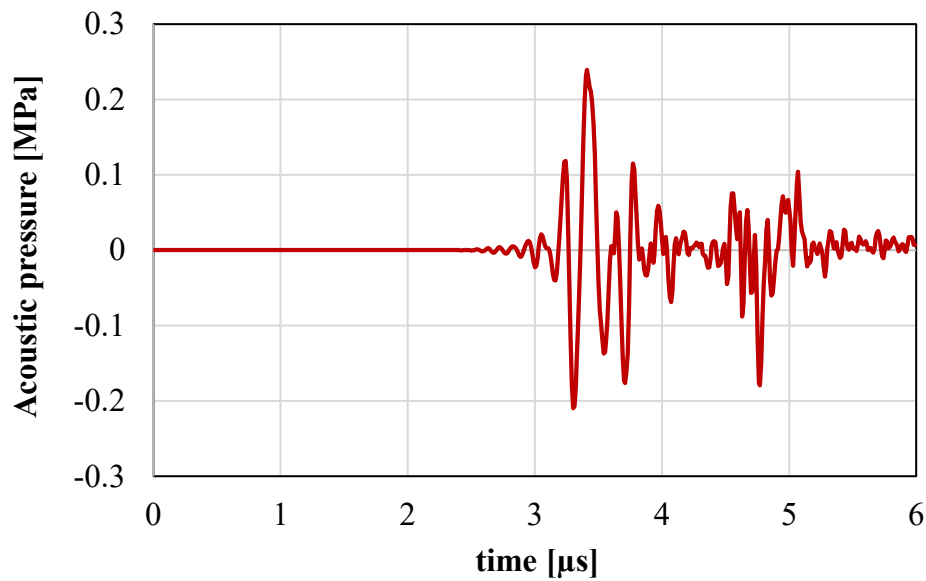


Figure 4.12 Output acoustic pressure of CSNP/PDMS transducer fabricated by Wenbin Huang et.al [28] under excitation of Matrix 532-14-40

#### 4.8 Comparison of two numerical models with different aperture sizes

In order to investigate the impact of beam diameter in pressure generation, two 2D-axisymmetric model were executed in COMSOL Multiphysics. Simulation parameters are the same for these two models except for the laser beam and are presented in table 4.6.

	Beam diameter [mm]	Laser fluence [ $\text{mJ}/\text{cm}^2$ ]	Pulse width [ns]	Absorption coefficient [ $1/\mu\text{m}$ ]	Water domain dimension [mm]
Model 1	0.53	11.3	6	1	10×5
Model 2	10	11.3	6	1	10×5

Table 4.6 Input parameters of CSNP/PDMS transducer in the numerical model

Mesh distribution is identical to the model explained in section 4.7 and time-dependent study was performed similar to our previous models. Pressure wave propagation inside water domain for model 1 and 2 is compared in figure 4.13.

Figure 4.14, shows the output pressure of model 1 and model 2 at 4.2mm away from the composite. As it can be observed, maximum pressure of the transducer with 0.53 mm beam size is about 20 times less than that of 10 mm one. This reduction in pressure is almost same as the change of aperture size,  $D$  (from 10mm to 0.53mm). This in turn implies that the pressure wave generated from smaller spot size carries less energy and is not able to produce a large pressure wave in far field. The effect of small spot size can also be seen in shock peening [76][77].

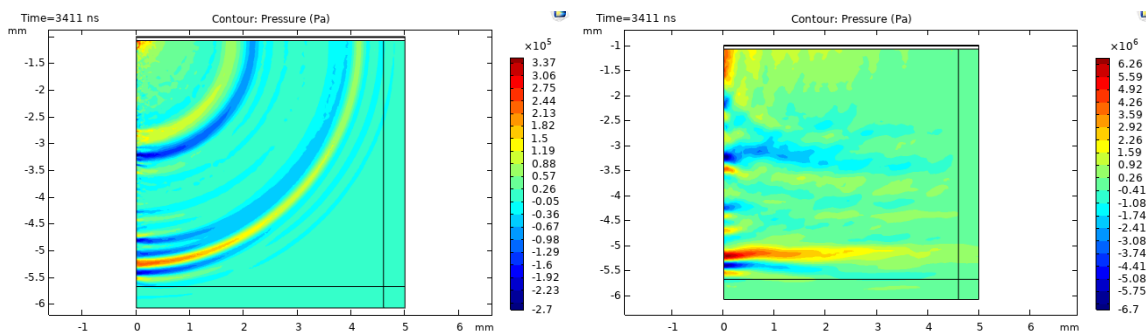


Figure 4.13 Pressure wave propagation in water for beam diameter of 0.53mm (left) and 10mm (right)

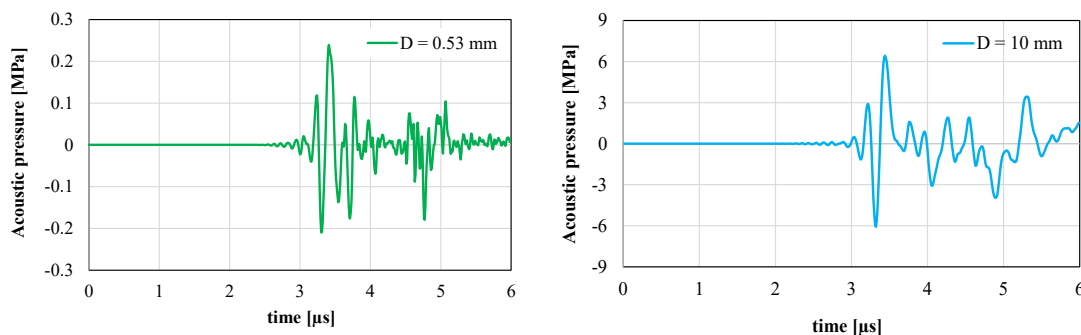


Figure 4.14 Pressure from CSNP/PDMS composite with beam diameter of 0.53 mm and 10 mm

To see how pressure wave dissipates in case of small and large spot size excitation source, maximum acoustic pressure was evaluated along wave propagation axis(z) and the result is displayed in figure 4.15. It can be noticed that pressure attenuates faster from 3.5 MPa to 0.2 MPa for the transducer excited by smaller beam diameter. Whereas pressure drop for the transducer with larger beam size(10mm) is only around 1 MPa.

Although acoustic pressure of 3.6 MPa can be generated in near field (200  $\mu\text{m}$ ) in case of spot size of 0.53mm, in the real experiment it is not recommended to bring the hydrophone that close to the source. To overcome this, smaller water tank needs to be designed. In the next section numerical simulation of reduced-size water domain will be presented.

In this section, numerical study of fabricate CSNP/PDMS transducer (in section 4-3) with Matrix 532-14-40 laser pulse excitation in reduced-size water domain will be evaluated. Table 4.7 shows the simulation parameters employed in COMSOL Multiphysics.

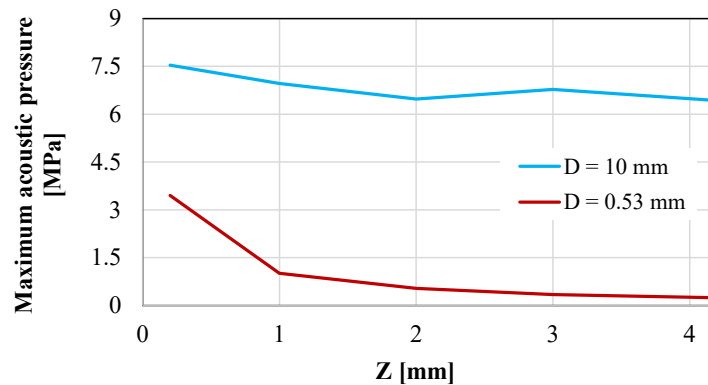


Figure 4.15 Attenuation of pressure along the propagation axis for 0.53 & 10mm beam diameter

#	Laser fluence [mJ/cm <sup>2</sup> ]	Beam diameter [mm]	Water domain dimensions [mm]	Pulse duration [ns]	Absorption coefficient [1/ $\mu\text{m}$ ]	CSNP/PDMS thickness [ $\mu\text{m}$ ]	Grüneisen coefficient
1	11.3	0.53	0.53 $\times$ 5	20	0.25	17/62	0.73
2	28.6	0.33	0.53 $\times$ 5	20	0.25	17/62	0.73
3	43.4	0.27	0.53 $\times$ 5	20	0.25	17/62	0.73

Table 4.7 Material properties and laser parameter in 2D axisymmetric model

It should be noted that Grüneisen coefficient is a dimensionless property of PDMS as it has been introduced in section 1.4. As it is shown in table 4.7, beam diameter was varied to obtain different

laser fluence since laser energy is kept constant. Numerical simulation was performed as explained in chapter 3. Time dependent acoustic pressure at 4.2mm away from the composite surface is plotted in figure 4.16.

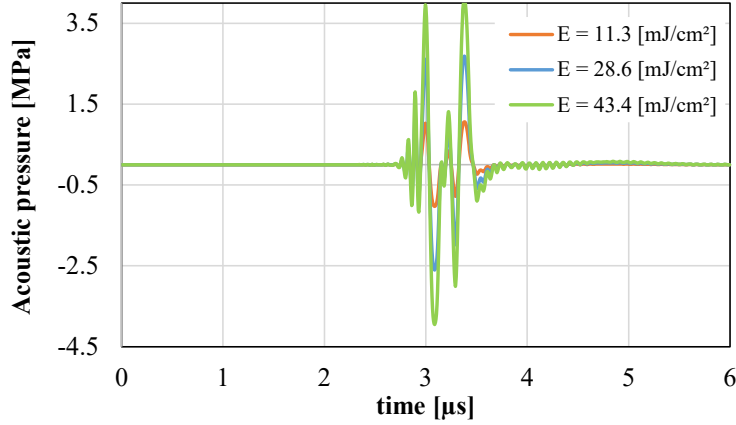


Figure 4.16 Pressure at various laser fluence measured 4.2 mm away from the composite

Relationship between laser fluence and maximum positive pressure is illustrated in figure 4.17. This result agrees with the study carried out in section 3.6 and demonstrates the linear relationship between acoustic pressure and laser fluence.

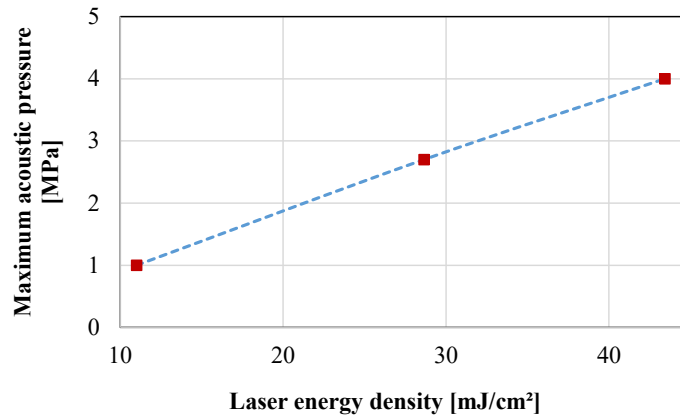


Figure 4.17 Maximum acoustic pressure of reduced-size CSNP/PDMS transducer with respect to various laser energy density

As explained in section 1-4, the initial pressure amplitude can be obtained from equation:

$$P_0 = \Gamma \cdot A \cdot \frac{E_0}{c\tau} \quad (4-5)$$

This equation approximates the pressure amplitude. It indicates that pressure amplitude is inversely proportional to the pulse width. Same result has also been obtained in figure 3.15. Since pulse width of Matrix 532-14-40 drops with repetition rate reduction as illustrated in figure 4.18, it is expected to observe an even larger acoustic pressure than what is predicted in figure 4.16.

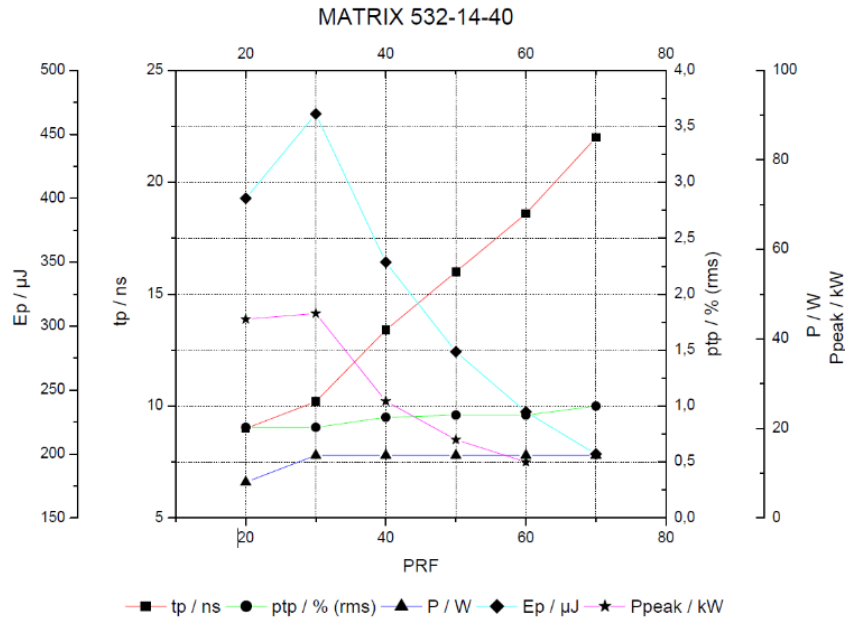


Figure 4.18 Characteristic curve of Matrix 532-14-40[74]

## 4.9 Summary

In this chapter, high repetition rate laser was examined to study the feasibility of photoacoustic pressure generation. Due to the accumulative laser energy in repetitive pulse lasers, damage threshold of the fabricated CSNP/PDMS has been measured. It can be concluded that repetition rates of 2600Hz and 10000Hz can be employed to generate acoustic pressure without posing any damage to the transmitter.

It should be noted that, the measured damage threshold is influenced by the optical properties of the transmitter as well as laser repetition rate. From the simulation result of different numerical models, it is clearly feasible to generate LGU using high repetition rate laser as an excitation source for CSNP/PDMS composite.

## **CHAPTER 5. General conclusion and future outlook**

Ultrasound has been widely used in the field of medical imaging and non-destructive testing. Recently, generation of ultrasound particularly for medical imaging has moved away from traditional piezo-transducers to lasers. From the extensive review of LGU, there have been significant amount of experimental work but very few works on the theory behind LGU composites. On the other hand, almost all the works in the literature utilize high power lasers with repetition rates of few hertz for the experiments. The aim of this work is to utilize high repetition rate lasers for ultrasound generation. To this extent, the objective and scope of the work have been formulated to understand the physics behind LGU, simulation of LGU process with CSNP/PDMS composite and compared with the result from the experiments in the literature.

2D simulation was performed on CSNP/PDMS composite LGU with COMSOL Multiphysics. The material properties of the composite were taken from the literature. The input parameters were selected from literature and the preliminary pressure output was extracted from the model similar to the experiments. However, significant shift in the result was found, as the maximum pressure obtained by numerical model was 6 times lower. Mesh refinement was performed and 2D model was changed to 2D-axisymmetric to reduce the computation time.

A different approach was taken to simulate the LGU model in 2-D axisymmetric environment and the model results were compared with the experimental studies for CSNP, CNF and CB embedded PDMS composite and maximum difference of 15% was observed between maximum pressure acoustic results between the experimental work in literature to the model developed under this study. To reduce the error induced by the line-average method of pressure evaluation, a new model was built to better approximate the surface of the active element of hydrophone. The acoustic pressure amplitude predicted by the refined model was within 4% of the pressure measured under similar conditions in the experiments found in literature. Mesh refinement was carried out to find out the optimum element size. It was concluded that the model is producing a mathematically accurate solution when “N” is set as 4 which corresponds to the mesh size of 37  $\mu\text{m}$ . The robustness of the model was further tested with different composites for different thicknesses under varying laser fluence. The linear relationship between acoustic pressure and laser fluence agrees with the results/trend from experiments available in the literature.

Further, high repetition rate laser was examined to study the feasibility of photoacoustic pressure generation. Due to the accumulative laser energy in repetitive pulse lasers, small laser fluence can damage the composite material. Damage threshold of the fabricated CSNP/PDMS has been measured to be  $167000 \text{ mJ/cm}^2$  under repetition rate of  $10000\text{Hz}$ . From the experiments, it can be concluded that repetition rates of  $2600\text{Hz}$  and  $10000\text{Hz}$  can be employed to generate acoustic pressure without posing any damage to the composite transducer.

Further, absorption coefficient of the fabricated samples was measured to be  $0.25 [1/\mu\text{m}]$ . The experimental results of the damage threshold and the absorption coefficient was used in the simulation for the feasibility study. From the results of the study, it can be concluded that it is clearly feasible to generate LGU using high repetition rate laser as an excitation source for CSNP/PDMS composite.

The developed numerical solution provides valuable data on how to improve the performance of laser generated ultrasound by tailoring the effective parameters. In this thesis, the feasibility study has been successfully carried out to understand the applicability of using a high repetition rate laser for ultrasound generation using CSNP/PDMS transducer. It can be said that; these low-cost lasers have the potential to be utilized as ultrasound source in biomedical applications. To achieve this, a numerical model that posits the results based on the laser-matter interaction has been developed, followed by validating the model with experimental and numerical studies from literature for three different light absorber materials (CSNP, CNF and CB). A numerical model has been validated for these transducers, by taking into account the prime factors from the literature. A feasibility study for a high repetition rate and low energy laser has been conducted, to understand its applicability for the laser ultrasound generation, such that the technology can be at the disposal of many industries and research enthusiasts.

## **5.1 Future research direction**

While the primary aim of the thesis for the development of laser assisted ultrasound was successfully met, there is lot of potential for future direction of research in this area. Some of which are summarized below.

- The experimental investigation of applicability of high repetition rate and low energy laser for the laser generated ultrasound can be conducted in different material composites.

- By utilising pulse width measurement tools such as autocorrelator, pulse duration can be determined in different repetition rates to establish more accurate simulation input.
- The simulation can also be carried out for studying focused ultrasound in non-planar substrates.
- Other fabrication techniques such as spin coating can be adapted to create a composite with smaller thickness and larger absorption coefficient to generate more efficient photoacoustic ultrasound.
- A new design of the water tank can be introduced in which the dimensions are optimized in such a way that desirable amount of acoustic pressure is propagated in water.
- High repetition rate lasers are expected to generate ultrasound waves of smaller bandwidths, as explained in chapter 4. This has not been considered in our simulation for feasibility which has to be considered in the future.

## References

- [1] H. Selim, M. Delgado-Prieto, J. Trull, R. Picó, L. Romeral, and C. Cojocar, “Defect reconstruction by non-destructive testing with laser induced ultrasonic detection,” *Ultrasonics*, vol. 101, no. June 2019, p. 106000, 2020, doi: 10.1016/j.ultras.2019.106000.
- [2] N. Wu, X. Zou, J. Zhou, and X. Wang, “Fiber optic ultrasound transmitters and their applications,” *Meas. J. Int. Meas. Confed.*, vol. 79, pp. 164–171, 2016, doi: 10.1016/j.measurement.2015.10.002.
- [3] J. Di, J. Kim, Q. Hu, X. Jiang, and Z. Gu, “Spatiotemporal drug delivery using laser-generated-focused ultrasound system,” *J. Control. Release*, vol. 220, pp. 592–599, Dec. 2015, doi: 10.1016/j.jconrel.2015.08.033.
- [4] J. Kim, W. Y. Chang, H. Wu, and X. Jiang, “Optical fiber laser-generated-focused-ultrasound transducers for intravascular therapies,” Oct. 2017, doi: 10.1109/ULTSYM.2017.8092704.
- [5] J. Y. Chapelon *et al.*, “New piezoelectric transducers for therapeutic ultrasound,” *Ultrasound Med. Biol.*, vol. 26, no. 1, pp. 153–159, 2000, doi: 10.1016/S0301-5629(99)00120-9.
- [6] T. Lee, H. W. Baac, Q. Li, and L. J. Guo, “Efficient Photoacoustic Conversion in Optical Nanomaterials and Composites,” *Adv. Opt. Mater.*, vol. 6, no. 24, pp. 1–30, 2018, doi: 10.1002/adom.201800491.
- [7] J. Li *et al.*, “A novel CNTs array-PDMS composite with anisotropic thermal conductivity for optoacoustic transducer applications,” *Compos. Part B Eng.*, vol. 196, no. May, p. 108073, 2020, doi: 10.1016/j.compositesb.2020.108073.
- [8] H. Won Baac *et al.*, “Carbon nanotube composite optoacoustic transmitters for strong and high frequency ultrasound generation,” *Appl. Phys. Lett.*, vol. 97, no. 23, pp. 1–4, 2010, doi: 10.1063/1.3522833.
- [9] W. Y. Chang, W. Huang, J. Kim, S. Li, and X. Jiang, “Candle soot nanoparticles-polydimethylsiloxane composites for laser ultrasound transducers,” *Appl. Phys. Lett.*, vol. 107, no. 16, 2015, doi: 10.1063/1.4934587.

- [10] “<Laser Generated Ultrasound Research Gate.Pdf>.” .
- [11] N. Yang, S. Li, C. Li, and X. Fan, “The Photoacoustic Effect of Multilayered Graphene Films,” *IOP Conf. Ser. Mater. Sci. Eng.*, vol. 531, no. 1, 2019, doi: 10.1088/1757-899X/531/1/012085.
- [12] B. Y. Hsieh, J. Kim, J. Zhu, S. Li, X. Zhang, and X. Jiang, “A laser ultrasound transducer using carbon nanofibers-polydimethylsiloxane composite thin film,” *Appl. Phys. Lett.*, vol. 106, no. 2, 2015, doi: 10.1063/1.4905659.
- [13] W. E. Gusev, A. A. A.A. Karabutov, and Anonymous, *Laser Optoacoustics*, vol. 1, no. 1. 1993.
- [14] “Physics of thermal processes in laser-tissue interaction - IOPscience.” <https://iopscience.iop.org/article/10.1088/0031-9155/35/9/001> (accessed Jul. 20, 2020).
- [15] J. R. Fincke, C. M. Wynn, R. Haupt, X. Zhang, D. Rivera, and B. Anthony, “Characterization of laser ultrasound source signals in biological tissues for imaging applications,” *J. Biomed. Opt.*, vol. 24, no. 02, p. 1, 2018, doi: 10.1117/1.jbo.24.2.021206.
- [16] G. Paltauf and P. E. Dyer, “Photomechanical processes and effects in ablation,” *Chem. Rev.*, vol. 103, no. 2, pp. 487–518, 2003, doi: 10.1021/cr010436c.
- [17] S.-G. Park *et al.*, “3D Hybrid Plasmonic Nanomaterials for Highly Efficient Optical Absorbers and Sensors,” *Adv. Mater.*, vol. 27, no. 29, pp. 4290–4295, Aug. 2015, doi: 10.1002/adma.201501587.
- [18] H. Bilgin, S. Zahertar, S. Sadeghzadeh, A. D. Yalcinkaya, and H. Torun, “A MEMS-based terahertz detector with metamaterial-based absorber and optical interferometric readout,” *Sensors Actuators, A Phys.*, vol. 244, pp. 292–298, Jun. 2016, doi: 10.1016/j.sna.2016.04.021.
- [19] S. Savo, D. Shrekenhamer, and W. J. Padilla, “Liquid crystal metamaterial absorber spatial light modulator for THz applications,” *Adv. Opt. Mater.*, vol. 2, no. 3, pp. 275–279, Mar. 2014, doi: 10.1002/adom.201300384.
- [20] X. Zhao *et al.*, “Optically tunable metamaterial perfect absorber on highly flexible substrate,” *Sensors Actuators, A Phys.*, vol. 231, pp. 74–80, Apr. 2015, doi:

- 10.1016/j.sna.2015.02.040.
- [21] R. Warren, F. Sammoura, K. S. Teh, A. Kozinda, X. Zang, and L. Lin, “Electrochemically synthesized and vertically aligned carbon nanotube-polypyrrole nanolayers for high energy storage devices,” *Sensors Actuators, A Phys.*, vol. 231, pp. 65–73, Aug. 2015, doi: 10.1016/j.sna.2014.07.010.
- [22] G. Yoo, Y. Park, P. Sang, H. W. Baac, and J. Heo, “High-frequency optoacoustic transmitter based on nanostructured germanium via metal-assisted chemical etching,” *Opt. Mater. Express*, vol. 6, no. 8, p. 2567, 2016, doi: 10.1364/ome.6.002567.
- [23] Y. Tian, N. Wu, X. Zou, H. Felemban, C. Cao, and X. Wang, “Fiber-optic ultrasound generator using periodic gold nanopores fabricated by a focused ion beam,” *Opt. Eng.*, vol. 52, no. 6, p. 065005, 2013, doi: 10.1117/1.oe.52.6.065005.
- [24] E. J. Alles *et al.*, “Acoustical characterisation of carbon nanotube-loaded polydimethylsiloxane used for optical ultrasound generation,” *IEEE Int. Ultrason. Symp. IUS*, 2017, doi: 10.1109/ULTSYM.2017.8092343.
- [25] J. Kim *et al.*, “Laser-generated-focused ultrasound transducers for microbubble-mediated, dual-excitation sonothrombolysis,” *IEEE Int. Ultrason. Symp. IUS*, vol. 2016-Novem, pp. 1–4, 2016, doi: 10.1109/ULTSYM.2016.7728473.
- [26] J. Di, J. Kim, Q. Hu, X. Jiang, and Z. Gu, “Spatiotemporal drug delivery using laser-generated-focused ultrasound system,” *J. Control. Release*, vol. 220, pp. 592–599, 2015, doi: 10.1016/j.jconrel.2015.08.033.
- [27] S. Hiremath, S. M. H, and S. M. Kulkarni, “Progression and characterization of polydimethylsiloxane-carbon black nanocomposites for photothermal actuator applications,” *Sensors Actuators, A Phys.*, vol. 319, p. 112522, 2021, doi: 10.1016/j.sna.2020.112522.
- [28] W. Huang, W. Y. Chang, J. Kim, S. Li, S. Huang, and X. Jiang, “A novel laser ultrasound transducer using candle soot carbon nanoparticles,” *IEEE Trans. Nanotechnol.*, vol. 15, no. 3, pp. 395–401, 2016, doi: 10.1109/TNANO.2016.2536739.
- [29] W. Y. Chang *et al.*, “Evaluation of Photoacoustic Transduction Efficiency of Candle Soot

- Nanocomposite Transmitters,” *IEEE Trans. Nanotechnol.*, vol. 17, no. 5, pp. 985–993, 2018, doi: 10.1109/TNANO.2018.2845703.
- [30] F. Gao *et al.*, “An analytical study of photoacoustic and thermoacoustic generation efficiency towards contrast agent and film design optimization,” *Photoacoustics*, vol. 7, pp. 1–11, 2017, doi: 10.1016/j.pacs.2017.05.001.
- [31] H. Wu, H. Kim, Y. Tang, J. Yao, and X. Jiang, “Fiber-optic laser-ultrasound transducer using carbon nanoparticles for intravascular sonothrombolysis,” in *Proceedings of the IEEE Conference on Nanotechnology*, Jul. 2019, vol. 2019-July, pp. 261–264, doi: 10.1109/NANO46743.2019.8993894.
- [32] Y. Li, Z. Guo, G. Li, and S.-L. Chen, “Miniature fiber-optic high-intensity focused ultrasound device using a candle soot nanoparticles-polydimethylsiloxane composites-coated photoacoustic lens,” *Opt. Express*, vol. 26, no. 17, p. 21700, 2018, doi: 10.1364/oe.26.021700.
- [33] J. Kim, W. Y. Chang, H. Wu, and X. Jiang, “Optical fiber laser-generated-focused-ultrasound transducers for intravascular therapies,” *IEEE Int. Ultrason. Symp. IUS*, pp. 15–18, 2017, doi: 10.1109/ULTSYM.2017.8092704.
- [34] “Mechanical characterization of bulk Sylgard 184 for microfluidics and microengineering Related content,” 2014, doi: 10.1088/0960-1317/24/3/035017.
- [35] S. Hwan Lee *et al.*, “Reduced graphene oxide coated thin aluminum film as an optoacoustic transmitter for high pressure and high frequency ultrasound generation,” *Appl. Phys. Lett.*, vol. 101, no. 24, p. 241909, Dec. 2012, doi: 10.1063/1.4772498.
- [36] S. Rajagopal, B. E. Treeby, and B. T. Cox, “Effect of Backing on Carbon-Polymer Nanocomposite Sources for Laser Generation of Broadband Ultrasound Pulses,” *IEEE Int. Ultrason. Symp. IUS*, vol. 2018-October, Dec. 2018, doi: 10.1109/ULTSYM.2018.8579784.
- [37] Y. Tian, N. Wu, K. Sun, X. Zou, and X. Wang, “Numerical simulation of fiber-optic photoacoustic generator using nanocomposite material,” *J. Comput. Acoust.*, vol. 21, no. 02, p. 1350002, 2013.

- [38] E. Biagi, F. Margheri, and D. Menichelli, “Efficient laser-ultrasound generation by using heavily absorbing films as targets,” *IEEE Trans. Ultrason. Ferroelectr. Freq. Control*, vol. 48, no. 6, pp. 1669–1680, 2001, doi: 10.1109/58.971720.
- [39] M. Liu, J. Sun, and Q. Chen, “Influences of heating temperature on mechanical properties of polydimethylsiloxane,” *Sensors Actuators, A Phys.*, vol. 151, no. 1, pp. 42–45, Apr. 2009, doi: 10.1016/j.sna.2009.02.016.
- [40] Y. Xiao *et al.*, “Thermal Studies of Three-Dimensional Printing Using Pulsed Laser Heating,” *ES Mater. Manuf.*, pp. 21–26, 2018, doi: 10.30919/esmm5f103.
- [41] S. Noimark *et al.*, “Polydimethylsiloxane Composites for Optical Ultrasound Generation and Multimodality Imaging,” *Adv. Funct. Mater.*, vol. 28, no. 9, p. 1704919, Feb. 2018, doi: 10.1002/adfm.201704919.
- [42] X. Zou, N. Wu, Y. Tian, and X. Wang, “Broadband miniature fiber optic ultrasound generator,” *Opt. Express*, vol. 22, no. 15, p. 18119, Jul. 2014, doi: 10.1364/oe.22.018119.
- [43] T. Buma, M. Spisar, and M. O’Donnell, “A high frequency ultrasound array element using thermoelastic expansion in PDMS,” in *Proceedings of the IEEE Ultrasonics Symposium*, 2001, vol. 2, pp. 1143–1146, doi: 10.1109/ultsym.2001.991920.
- [44] A. Maxwell, S. W. Huang, T. Ling, J. S. Kim, S. Ashkenazi, and L. J. Guo, “Polymer microring resonators for high-frequency ultrasound detection and imaging,” *IEEE J. Sel. Top. Quantum Electron.*, vol. 14, no. 1, pp. 191–197, Jan. 2008, doi: 10.1109/JSTQE.2007.914047.
- [45] S. Noimark *et al.*, “Carbon-Nanotube–PDMS Composite Coatings on Optical Fibers for All-Optical Ultrasound Imaging,” *Adv. Funct. Mater.*, vol. 26, no. 46, pp. 8390–8396, Dec. 2016, doi: 10.1002/adfm.201601337.
- [46] R. J. Colchester *et al.*, “Laser-generated ultrasound with optical fibres using functionalised carbon nanotube composite coatings,” *Appl. Phys. Lett.*, vol. 104, no. 17, p. 173502, Apr. 2014, doi: 10.1063/1.4873678.
- [47] S. L. Chen *et al.*, “Efficient real-time detection of terahertz pulse radiation based on photoacoustic conversion by carbon nanotube nanocomposite,” *Nat. Photonics*, vol. 8, no.

- 7, pp. 537–542, 2014, doi: 10.1038/nphoton.2014.96.
- [48] S. Rosset, M. Niklaus, P. Dubois, and H. R. Shea, “Metal ion implantation for the fabrication of stretchable electrodes on elastomers,” *Adv. Funct. Mater.*, vol. 19, no. 3, pp. 470–478, Feb. 2009, doi: 10.1002/adfm.200801218.
- [49] S. Noimark *et al.*, “Dual-mechanism antimicrobial polymer-ZnO nanoparticle and crystal violet-encapsulated silicone,” *Adv. Funct. Mater.*, vol. 25, no. 9, pp. 1367–1373, Mar. 2015, doi: 10.1002/adfm.201402980.
- [50] “Laser Ultrasonics Techniques and Applications - C.B Scruby, L.E Drain - Google Books.” [https://books.google.ca/books/about/Laser\\_Ultrasonics\\_Techniques\\_and\\_Applica.html?id=KgXPqx9ST-wC&redir\\_esc=y](https://books.google.ca/books/about/Laser_Ultrasonics_Techniques_and_Applica.html?id=KgXPqx9ST-wC&redir_esc=y) (accessed Nov. 01, 2020).
- [51] C. Lou, S. Yang, Z. Ji, Q. Chen, and D. Xing, “Ultrashort microwave-induced thermoacoustic imaging: A breakthrough in excitation efficiency and spatial resolution,” *Phys. Rev. Lett.*, vol. 109, no. 21, pp. 1–5, 2012, doi: 10.1103/PhysRevLett.109.218101.
- [52] “Pulsed Lasers Introduction to Power and Energy Calculations.”
- [53] A. S. Hassanien and A. A. Akl, “Effect of Se addition on optical and electrical properties of chalcogenide CdSSe thin films,” *Superlattices Microstruct.*, vol. 89, no. January 2019, pp. 153–169, 2016, doi: 10.1016/j.spmi.2015.10.044.
- [54] Abhijeet Bagal *et al.*, “Multifunctional nano-accordion structures for stretchable transparent conductors,” *Mater. Horizons*, vol. 2, no. 5, pp. 486–494, Aug. 2015, doi: 10.1039/C5MH00070J.
- [55] E. Weingartner, H. Saathoff, M. Schnaiter, N. Streit, B. Bitnar, and U. Baltensperger, “Absorption of light by soot particles: Determination of the absorption coefficient by means of aethalometers,” *J. Aerosol Sci.*, vol. 34, no. 10, pp. 1445–1463, Oct. 2003, doi: 10.1016/S0021-8502(03)00359-8.
- [56] K. Nama Manjunatha and S. Paul, “Investigation of optical properties of nickel oxide thin films deposited on different substrates,” *Appl. Surf. Sci.*, vol. 352, pp. 10–15, 2015, doi: 10.1016/j.apsusc.2015.03.092.
- [57] S. Atar and U. Rosenschein, “Perspectives on the role of ultrasonic devices in

- thrombolysis,” *Journal of Thrombosis and Thrombolysis*, vol. 17, no. 2. Kluwer Academic Publishers, pp. 107–114, Apr. 2004, doi: 10.1023/B:THRO.0000037665.21691.61.
- [58] A. D. Maxwell, G. Owens, H. S. Gurm, K. Ives, D. D. Myers, and Z. Xu, “Noninvasive treatment of deep venous thrombosis using pulsed ultrasound cavitation therapy (histotripsy) in a porcine model,” *J. Vasc. Interv. Radiol.*, vol. 22, no. 3, pp. 369–377, Mar. 2011, doi: 10.1016/j.jvir.2010.10.007.
- [59] A. Burgess, Y. Huang, A. C. Waspe, M. Ganguly, D. E. Goertz, and K. Hynynen, “High-Intensity Focused Ultrasound (HIFU) for Dissolution of Clots in a Rabbit Model of Embolic Stroke,” *PLoS One*, vol. 7, no. 8, p. e42311, Aug. 2012, doi: 10.1371/journal.pone.0042311.
- [60] A. Ng and J. Swanevelder, “Resolution in ultrasound imaging,” *Contin. Educ. Anaesthesia, Crit. Care Pain*, vol. 11, no. 5, pp. 186–192, 2011, doi: 10.1093/bjaceaccp/mkr030.
- [61] G. Ding and hui xia, “Laser-induced focused ultrasound for noninvasive sonothrombolysis using candle soot polymer nanocomposite-coated photoacoustic lens,” vol. 1117023, no. May, p. 120, 2019, doi: 10.1117/12.2533587.
- [62] R. J. Colchester, E. J. Alles, and A. E. Desjardins, “A directional fibre optic ultrasound transmitter based on a reduced graphene oxide and polydimethylsiloxane composite,” *Appl. Phys. Lett.*, vol. 114, no. 11, 2019, doi: 10.1063/1.5089750.
- [63] H. W. Baac *et al.*, “Carbon-nanotube optoacoustic lens for focused ultrasound generation and high-precision targeted therapy,” *Sci. Rep.*, vol. 2, pp. 1–8, 2012, doi: 10.1038/srep00989.
- [64] S. Wang, “Photo-thermal application of a polydimethylsiloxane foam embedded with carbon nanoparticles for interfacial solar water evaporation,” no. June, 2019.
- [65] N. D. Katopodes, “Methods for Two-Dimensional Shallow-Water Flow,” in *Free-Surface Flow*, Elsevier, 2019, pp. 500–567.
- [66] “Digital communications : fundamentals and applications. (Book, 1988) [WorldCat.org].” <https://www.worldcat.org/title/digital-communications-fundamentals-and-applications/oclc/300414546> (accessed Mar. 17, 2021).
- [67] J. P. Berenger, “A perfectly matched layer for the absorption of electromagnetic waves,” *J.*

- Comput. Phys.*, vol. 114, no. 2, pp. 185–200, Oct. 1994, doi: 10.1006/jcph.1994.1159.
- [68] “Numerical Simulation of Mechatronic Sensors and Actuators,” doi: 10.1007/978-3-642-40170-1.
- [69] S. Noimark *et al.*, “Carbon-Nanotube–PDMS Composite Coatings on Optical Fibers for All-Optical Ultrasound Imaging,” *Adv. Funct. Mater.*, vol. 26, no. 46, pp. 8390–8396, 2016, doi: 10.1002/adfm.201601337.
- [70] S. Hiremath, S. M. H, and S. M. Kulkarni, “Progression and characterization of polydimethylsiloxane-carbon black nanocomposites for photothermal actuator applications,” *Sensors Actuators, A Phys.*, vol. 319, p. 112522, Mar. 2021, doi: 10.1016/j.sna.2020.112522.
- [71] A. S. Hassanien, K. A. Aly, and A. A. Akl, “Study of optical properties of thermally evaporated ZnSe thin films annealed at different pulsed laser powers,” *J. Alloys Compd.*, vol. 685, no. November, pp. 733–742, 2016, doi: 10.1016/j.jallcom.2016.06.180.
- [72] S. Mallidi and S. Emelianov, “Photoacoustic technique to measure beam profile of pulsed laser systems,” *Rev. Sci. Instrum.*, vol. 80, no. 5, 2009, doi: 10.1063/1.3125625.
- [73] J. Jang, P. Liu, B. Kim, S. woo Kim, and H. Sohn, “Silicon wafer crack detection using nonlinear ultrasonic modulation induced by high repetition rate pulse laser,” *Opt. Lasers Eng.*, vol. 129, p. 106074, Jun. 2020, doi: 10.1016/J.OPTLASENG.2020.106074.
- [74] “MATRIX 1064 and 532 A P P L I C A T I O N S • ID Card Marking • Diamond Processing • PCB No Good Marking • SIP Processing • Wafer Marking • LGP Mask Drilling.”
- [75] “Solid-State, Q-Switched Laser Front View Rear View Side View Top View,” 2011, Accessed: Aug. 01, 2021. [Online]. Available: [www.Coherent.com](http://www.Coherent.com).
- [76] K. Ding and L. Ye, “Physical and mechanical mechanisms of laser shock peening,” *Laser Shock Peen.*, pp. 7–46, Jan. 2006, doi: 10.1533/9781845691097.7.
- [77] “doi:10.1016/j.ijfatigue.2007.01.033 | Elsevier Enhanced Reader.” <https://reader.elsevier.com/reader/sd/pii/S0142112307000588?token=4CE4267D03E05095765AD3D922AB6FE6109576FFD3402589148CE7ABF827B1FEA4FE322DA98ABFE9927CA355D8F7C2DF&originRegion=us-east-1&originCreation=20210903035709>

(accessed Sep. 03, 2021).